UNIVERSITY OF OKLAHOMA

GRADUATE COLLEGE

LIMITATIONS AND POTENTIAL OF COMPLEX CLOUD ANALYSIS AND ITS IMPROVEMENT FOR RADAR REFLECTIVITY DATA ASSIMILATION USING OSSES

A DISSERTATION

SUBMITTED TO THE GRADUATE FACULTY

in partial fulfillment of the requirements for the

Degree of

DOCTOR OF PHILOSOPHY

By

CHONG-CHI TONG
Norman, Oklahoma
2015

LIMITATIONS AND POTENTIAL OF COMPLEX CLOUD ANALYSIS
AND ITS IMPROVEMENT FOR RADAR REFLECTIVITY DATA ASSIMILATION
USING OSSES

A DISSERTATION APPROVED FOR THE
SCHOOL OF METEOROLOGY

BY

_____
Dr. Ming Xue, Chair

_____
Dr. David Parsons

_____
Dr. Fanyou Kong

_____
Dr. Guifu Zhang

_____
Dr. Lance Leslie

_____
Dr. Sivaramakrishnan Lakshmivarahan

Acknowledgements

It has been such a long journey finishing up a doctoral degree! Achievement like this can't be done without continuous passion, which could be supported and refilled by a number of wonderful people: Dr. Ming Xue, my advisor, who kept five years of regular meetings in which I obtained inspiring and valuable instructions on my research, my other committee members, Drs. David Parsons, Lance Leslie, Fanyou Kong, Guifu Zhang, and S. Lakshmivarahan, who helped me refine my dissertation research with helpful suggestions and greatest patience, and those professors who taught the classes from which I acquired useful knowledge and skills highly beneficial to my Ph.D. works.

In addition, I want to appreciate the hard-working research crew who kept developing and maintaining the ARPS system. Thanks to Drs. Keith Brewster and Youngsun Jung for their helps on resolving some technical problems. My classmates and colleagues, Bryan Putnam, Rong Kong, Gang Zhao, Mike VandenBerg, and Jonty Hall are thanked for the inspiring discussions on course or research works. I also appreciate the warm cares and administrative assistance provided by the kind secretaries in both the CAPS and SoM, including Ms. Eileen Hasselwander, Debra Farmer, Christie Upchurch, and Celia Jones. Mutual cheering-ups provided by the forever-enthusiastic-Thunder-fan, Marcia Pallutto with relaxation from my intense study are truly valued.

Last, I would like to save some space for my loving and beloved family, especially my parents, grandparents, and my sister. Thanks for them to bear this long-term separation with their endless support and encouragement for me to pursue my study-abroad dream. Deepest love will be for them like always!

The simulation works presented in this study were performed using the supercomputing resources provided by the Extreme Science and Engineering Discovery Environment (XSEDE) and OU Supercomputing Center for Research and Education (OSCER).

Table of Contents

Acknowledgements iv

List of Tables ix

List of Figures x

Abstract xvi

Chapter 1: Introduction 1

1.1 Background and Motivations 1

1.2 An Overview of the Study 7

Chapter 2: Cloud Analysis and a Real Case Application 8

2.1 Existing Cloud Analysis Systems and Algorithms 8

2.2 The ARPS Complex Cloud Analysis 12

2.2.1 An Overview of Current Complex Cloud Analysis in the ARPS 12

2.2.2 A Modified Mixing Ratio Analysis Procedure 19

2.3 The Use of Polarimetric Radar Measurements in the Cloud Analysis 21

2.3.1 Mixing Ratio Analysis Using Polarimetric Radar Variables 21

2.3.2 A Mei-Yu Front Mesoscale Convective Vortex and Model Configuration 26

2.3.3 Results and Discussion 29

Chapter 3: Observing System Simulation Experiments based on Direct Initial Variable Insertion 38

3.1 Introduction 38

3.2 The Truth Simulation and the Degraded Control Experiment 41

3.2.1 The Model Configuration and Truth Simulation 42

3.2.2 Degraded Control Experiment from Smoothed Initial Condition 47
3.3 Experiments with Model Error in Microphysics 58
3.3.1 Design of Experiments 59
3.3.2 Results and Discussion 61
3.3.3 Summary 72
3.4 Experiments with Direct Insertion of State Variables 74
3.4.1 Design of Experiments 75
3.4.2 Results and Discussion 76
3.4.3 Summary 86
Chapter 4: Cloud Analysis Experiments 88
4.1 Introduction 88
4.2 Experiments with Different Configurations of Cloud Analysis 91
4.2.1 Design of Experiments 91
4.2.2 Results and Discussion 92
4.2.3 Summary 108
4.3 Conceptual Model of Forecast Error 109
Chapter 5: Improving Moisture Adjustment in Cloud Analysis 117
5.1 Impact of Moisture Accuracy 117
5.1.1 Validity of Current Moisture Adjustment 117
5.1.2 Design and Test of a Potential Modified Moisture Adjustment 122
5.2 A Modified Moisture Adjustment and its Impact 132
5.2.1 Development of a Vertical Motion Based Moisture Adjustment 134
5.2.2 Impact of the Modified Moisture Adjustment 143

Chapter 6: Summary and Future Work 149

6.1 Summary and Conclusions 149

6.2 Future Work 154

References 156

Appendix A: Formulation of the Modified Mixing Ratio Analysis Procedure 166

A.1 Retrieving the Portions of Mixtures 166

A.2 Extracting the Coefficient in Radar Operator for Rain 167

A.3 Extracting the Coefficients in Radar Operator for Species Other than Rain 168

A.4 Calculating for Final Analysis of Mixing Ratios 170

Appendix B: Verification Indices 173

B.1 Scaled Root Mean Square Errors 173

B.2 Scaled Energy Differences 174

List of Tables

Table 1.1 Summary of the differences between Ge et al. (2013) and this study 6

Table 2.1 Summary ARPS complex cloud analysis procedure 18

Table 2.2 Empirical hard thresholds used to suppress apparently wrong designations (reproduced from Park et al. 2009) 24

Table 2.3 Naming of experiments with corresponding settings 29

Table 3.1 List of the truth simulation, four smoothing experiments, and their respective statistics 48

Table 3.2 Configurations of microphysics experiments 60

Table 3.3 Configurations of direct insertion experiments 76

Table 5.1 Contingency table used for statistics above the FL 135

List of Figures

FIG. 1.1 Equitable threat score (ETS) of hourly precipitation at 0.5 inch threshold averaged over the last 15 days of 2008 Spring Experiment. Experiments with grid spacing of 4 km and 2 km are denoted by blue and red color, respectively. Dash line indicates experiment with no radar analysis. Adapted from Xue et al. (2008). 4

FIG. 2.1 Trapezoidal membership function, where X is an arbitrary radar variable. Adapted from Park et al. (2009). 23

FIG. 2.2 Weekly averaged sea surface temperature during 2-8 June 2008 and MCV track. Gray dots and black dots are tracked by IR satellite images and radar radial velocity, respectively. Red square denotes the domain of our simulation. Reproduced from Lai et al. (2011). 27

FIG. 2.3 Distribution of four CWB operational radars and NCAR S-Pol radar. Observing ranges are denoted by circles in corresponding colors (200 km for CWB radars and 150 km for NCAR S-Pol). 28

FIG. 2.4 (a) Composite reflectivity observed by NCAR S-Pol at 00 UTC 5 June 2008 and a (b) selected cross section **AB**. 29

FIG. 2.5 Mixing ratio (g/kg) analyses for hydrometeor: (a)(b) rain, (c)(d) snow, and (e)(f) hail, using KRY (left panel) and JZX (right panel) procedure. 31

FIG. 2.6 Hourly rainfall accumulation (mm) of (a) CWB QPESUMS, (b) KRY_S, (c) JZX_S, (d) KRY_D, and (e) JZX_D valid at 01 UTC 5 June 2008. Hour rainfall maximum is written at the lower right corner of each plot. 35

FIG. 2.7 One hour forecast of mixing ratio (g/kg) analyses for hydrometeor: (a)(b) rain, (c)(d) snow, and (e)(f) hail of experiment KRY_S (left panel) and JZX_S (right panel). 36

FIG. 3.1 Synoptic analysis at 925 mb valid at 00 UTC 19 May 2013. Geopotential height, temperature, and dew point temperature are provided with black solid contours, red dash contours, and green solid contours, respectively. Winds are provided in flags. Courtesy to the Storm Prediction Center of NOAA's National Weather Service..... 42

FIG. 3.2 Computational domains used for the experimental EnKF ensemble in 2013 Spring Experiment (600 × 400 grids with 4-km spacing denoted by black rectangle) and our study (803 × 803 grids with 1-km spacing denoted by red square). 44

FIG. 3.3 Time line of the truth simulation and the experiments. Main studied period is marked by gray shading area. 45

FIG. 3.4 Hourly simulated composite reflectivity (Z) and surface winds (V_h) of the truth simulation at (a) 02 UTC, (b) 03 UTC, (c) 04 UTC, (d) 05 UTC, and (e) 06 UTC. Wind flags are plotted in 40 km interval. 46

FIG. 3.5 Perturbation potential temperature (θ') and horizontal wind (V_h) field at 6 km AGL at 02 UTC for (a) the truth simulation, experiment (b) SMT_d15, (c) SMT_d35, (d) SMT_d55, and (e) SMT_d75. Wind flags are plotted in 40 km interval. 49

FIG. 3.6 SRMS error time series of (a) V_h, (b) w, (c) T, (d) q_v, (e) q_w, and (f) all variables for four smoothing experiments. The extra gray solid line in (b) is for a uniform 0 m s^{-1} w field. 52

FIG. 3.7 (a) RMS_Z, (b) bias score, and (c) ETS calculated with threshold of 30 dBZ for four smoothing experiments. 54

FIG. 3.8 Same as FIG.3.4, but for the experiment SMT_d15. 55

FIG. 3.9 Same as FIG. 3.4, but for the experiment SMT_d75. 56

FIG. 3.10 ASED of four smoothing experiments. 58

FIG. 3.11 Same as FIG. 3.6, but for the CNTL and three microphysics experiments. .. 62

FIG. 3.12 Same as 3.10, but for the CNTL and three microphysics experiments..... 64

FIG. 3.13 Composite reflectivity and surface winds at 02 UTC for (a) truth simulation, (b) CNTL, (c) MYSM, (d) MYDM, and (e) Lin. The convergent line is indicated by a red dash line in (a). Wind arrows are plotted in 30 km interval. 68

FIG. 3.14 Same as FIG. 3.13, but for 04 UTC. 69

FIG. 3.15 Same as FIG. 3.7, but for the CNTL and three microphysics experiments. .. 72

FIG. 3.16 Same as FIG. 3.6, but for the CNTL and five direct insertion experiments. . 81

FIG. 3.17 Same as FIG. 3.7, but for the CNTL and five direct insertion experiments. . 84

FIG. 3.18 Composite reflectivity and surface winds at 03 UTC for (a) Pt, (b) Qv, (c) Qcld, (d) Qpcp, and (e) Qall. Wind arrows are plotted in 30 km interval..... 85

FIG. 4.1 Cross section of truth mixing ratio in g kg^{-1} for (a) rain water, (b) snow, (c) graupel, and (d) hail. 93

FIG. 4.2 Same as FIG. 4.1, but for the cloud analysis experiments. 94

FIG. 4.3 Cross section of 10log(N_0) from the truth simulation for (a) rain, (b) snow, and (c) graupel. The default N_0 values are marked by black dash line on the color bar. 97

FIG. 4.4 Composite reflectivity and surface winds at 2:00 UTC for (a) truth simulation and (b) experiments with cloud analysis. 98

FIG. 4.5 Same as FIG. 3.6, but for the CNTL and four cloud analysis experiments. 98

FIG. 4.6 Same as 3.10, but for the CNTL and four cloud analysis experiments..... 103

FIG. 4.7 Same as FIG. 3.7, but for the CNTL and four cloud analysis experiments. .. 105

FIG. 4.8 Same as FIG. 3.18, but for four cloud analysis experiments (a) NoAdj, (b) PtAdj, (c) QvAdj, and (d) BothAdj. 107

FIG. 4.9 Conceptual model of the forecast error evolution corresponding to IC accuracy (including the resolution fineness of moisture field and hydrometeor availability) and model perfectness. Details about the arrow marks are provided in the context. 111

FIG. 5.1 Cross section of RH field (%) for (a) truth simulation, (b) background (CNTL), and (d) QvAdj. The RH difference between the truth and CNTL (CNTL-truth) is given as (c). The height of 0 °C is denoted by white solid lines in (a) and (b). 15 dBZ echo boundary is drawn by gray contour in (c) and (d) for a rough illustration of cloudy regions. The LCL is denoted by a blue dash line in (d). 120

FIG. 5.2 RMS error of q_v as a function of height (in terms of model level) at forecast initial (2:00 UTC). Experiments with and without hydrometeor analysis are represented by solid and dash lines, respectively. The ninth level is marked with a horizontal blue dash line. See context for detailed description. 122

FIG. 5.3 Cross section of RH field (%) for (a) truth simulation and (c) RHInsrt. Cross section of q_v field (g/kg) for (b) truth simulation and (d) RHInsrt. Corresponding 0 °C levels are denoted by white solid lines. 15 dBZ echo boundary is drawn by gray contour. The LCL is denoted by blue dash line for experiment RHInsrt indicating the bottom boundary of adjustment. 125

FIG. 5.4 Same as FIG. 3.6, but for the CNTL, TrueQv, NoAdj, SatAdj, RHInsrt, and UpdftAdj. 126

FIG. 5.5 RMS error of (a) u, (b) θ, (c) q_v, and (d) q_w as a function of height (in terms of model level) at 30-min forecast (2:30 UTC). Experiments with and without hydrometeor analysis are represented by solid and dash lines, respectively.... 130

FIG. 5.6 Same as FIG. 3.7, but for the CNTL, TrueQv, NoAdj, SatAdj, RHInsrt, and UpdftAdj. 132

FIG. 5.7 Same as FIG. 5.1a, but with black contours of true w = -0.2 m/s overlaid.... 133

FIG. 5.8 Diagram of w and RH fields used for statistics above the FL. Area within the blue and black ellipses denotes w < threshold and RH < 100%, respectively. Hits and misses corresponding to the contingency table test (Table 5.1) are shaded in gray and yellow color, respectively. 135

FIG. 5.9 HMR as a function of varying w threshold. 136

FIG. 5.10 SRMSE of q_v as a function of varying constant RH value specified for negative w areas. For reference purpose, SRMSEs of some other associated experiments are listed at upper right corner of the plot. 138

FIG. 5.11 Scatter plot of the true w and RH within the cloudy regions below the FL. Scatters between two black dash lines are used to fit for polynomial relations. Blue curve is the final relation used as the modified q_v adjustment. 141

FIG. 5.12 Retrieval of w-RH relationship using (a) first order, (b) second order, and (c) third order polynomial regression. Regression results are plotted with blue solid line or curves in the middle of the figures, along with the equations written. Constant RH values used for w exceeding terminal thresholds are marked with horizontal dashed blue lines at both sides. SRMS error of q_v analysis using corresponding equation is listed at the bottom left corner of each plot..... 142

FIG. 5.13 Same as FIG. 5.3, but for the SatAdj (upper panel) and UpdftAdj (lower panel). 144

Abstract

The radar data assimilation is very important for improving short-range precipitation forecasts. Within the three dimensional variational (3DVAR) framework which is still the prevailing method used for operational regional and convective-scale numerical weather prediction (NWP) systems, complex cloud analysis schemes have been shown to be quite effective for assimilating radar reflectivity data. However, due to semi-empirical nature of such schemes, there exist deficiencies. This study attempts to gain a better understanding of the limitations of the complex cloud analysis system within the Advanced Regional Prediction System (ARPS), and based on the results propose improvements to the system. The sensitivity of the short-range precipitation forecast to the accuracy of the initial state variables is also investigated to guide improvements to the cloud analysis.

A general overview of various existing cloud analysis systems/algorithms is first provided, followed by a detailed introduction to the current version of the ARPS complex cloud analysis system. A new version of the hydrometeor analysis is implemented based on the recently developed reflectivity operators that include a simple melting model. A hydrometeor classification algorithm based on polarimetric radar variables is utilized to help determine the hydrometeor species. The impact of the revised cloud analysis on very short range rainfall forecast is examined for a maritime mesoscale convective vortex case. Only a small sensitivity of the results to this revised cloud analysis algorithm is found. Significant model error is likely to be a contributing factor.

To unambiguously determine the sensitivity of model forecasts to the cloud analysis procedure and to various treatments within, we focus the rest of our study on experiments conducted in an observing system simulation experiment (OSSE) framework, for a case of mesoscale convective system (MCS) that occurred over central United States. A degraded initial condition is created through smoothing a truth forecast and by removing cloud fields. The simulation based on this degraded initial condition serves as a control, while sensitivity and data assimilation experiments try to improve the degraded initial conditions, or examine the impact of improved initial conditions.

The sensitivity of precipitation forecasts of up to four hours to 1) model error due to the use of different microphysics scheme and 2) accuracy of model initial state variables is first investigated. The sensitivity to state variables is examined by inserting the perfect values of individual or a group of variables back into the smoothed initial conditions. The forecast winds, temperature (T), moisture (q_v), total water-ice mixing ratio (q_w), and radar reflectivity (Z) of sensitivity experiments are evaluated in terms of the root mean square (RMS) error calculated against the truth. The results show that compared to the initial state of hydrometeors, the model microphysics has a relatively small impact on the prediction of state variables in a relatively short range. However, microphysics errors become significant for longer range forecasts, such after two hours, when evaluated in terms of forecast reflectivity. Among the model state variables updated by the cloud analysis, q_v is found to have the greatest impact on the prediction of state variables and forecast reflectivity. Precipitation hydrometeors have the second largest impact in terms of short-term prediction of q_w and associated T while the importance of the non-precipitating hydrometeors is relatively small.

The other set of experiments is designed to examine the impact and effectiveness of the cloud analysis scheme. In these experiments, hydrometeor and associated in-cloud state variables in the initial condition are obtained using the ARPS cloud analysis scheme with varying configurations, rather than through direct insertion as in the first set of experiments. When performing the hydrometeor analysis only without updating any other in-cloud state variable, noticeable and up-to-four-hours positive impact on forecast can be found in comparison with the hydrometeor-clear control. However, when q_v is adjusted to the value of saturation mixing ratio, i.e., the relative humidity (RH) is adjusted to 100% within precipitation region, as is done in the current ARPS cloud analysis procedure, rapid forecast error growth is found in most state variables and reflectivity is significantly over-forecasted. The in-cloud temperature adjustment towards the moist-adiabat of low-level lifted parcel in the cloud analysis is found to work quite well.

Based on the results of the earlier OSSEs, efforts are made to improve the q_v adjustment procedure in the cloud analysis to reduce precipitation overforecast. The effectiveness of a better specified in-cloud humidity field, by direct insertion of the true RH, is firstly demonstrated. A modified q_v adjustment procedure making use of the vertical velocity information is further proposed. This procedure avoids over-moistening in the downdraft regions, but the overall error in the adjusted q_v is not necessarily reduced quantitatively due to loose relationship between vertical velocity and relative humidity. Still, the forecasts resulting from the modified q_v adjustment is significantly improved over that from the original scheme.

Chapter 1: Introduction

1.1 Background and Motivations

Given the potential vital impact on human society, convective-scale precipitation systems and their forecasts using numerical weather prediction (NWP) models initialized with real observations, since the first attention called by Lilly (1990), have become an active field of research in the past two decades (e.g., Johns and Doswell 1992; Droegemeier et al. 1993; Lin et al. 1993; Hohenegger and Schär 2007; Stensrud et al. 2009; Xue et al. 2013). However, improving the forecast of convective-scale severe weather has still remained a great challenge. This difficulty is owing to not only the nonlinear dynamics and physics of the associated systems (Lorenz 1963), but also errors and deficiencies in the NWP models (Tribbia and Baumhefner 1988) and data assimilation (DA) systems.

Radar measurements have been widely used as a key source of data in convective-scale DA for their fine temporal and spatial resolutions. In the United States, the establishment of the Weather Surveillance Radar-1988 Doppler (WSR-88D; Crum and Alberty 1993) operational network in particular enable researchers and scientists to conduct storm-scale studies with its nationwide coverage. In these studies, radar reflectivity and radial velocity data are assimilated into NWP model using various DA techniques. Under the strong constraint of a prediction model, the four-dimensional variational (4DVAR; Lewis and Derber 1985) data assimilation is able to effectively assimilate observations within an assimilation window. A number of studies that assimilated either observational or simulated radar data using 4DVAR have been reported in the literature with reasonable results (e.g., Sun and Crook 1997, 1998).

However, these results were typically based on much simplified model physics, such as the warm rain microphysics. Due to the difficulties in developing the required adjoint model and convergence issues associated with highly nonlinear microphysics that are essential for accurate predictions, the practical application of 4DVAR to the convective-scale DA have been limited (Xu et al. 1996a, b). The ensemble Kalman filter (EnKF; Evensen 1994; Houtekamer and Mitchell 1998), a relatively new technique, has been demonstrated to provide promising analyses and forecasts with radar data (Snyder and Zhang 2003; Tong and Xue 2005). With a flow-dependent error covariance obtained from ensemble forecasts, the EnKF method has the ability to accumulate information through assimilation cycles to provide theoretically optimal initial conditions for initializing ensemble forecasts. The EnKF method also has its issues, however, such as covariance inflation and location, multiscale and model error issues, which still require much more research before the method becomes mature enough for operational applications at the convective scale. The high computational cost is also an important consideration.

Compared with the theoretically more advanced DA schemes 4DVAR and EnKF methods described above, the three-dimensional variational (3DVAR) DA method is widely used at operational NWP centers, especially for regional models, because of its lower computational cost and few technical difficulties associated with high nonlinearity. Its reasonably effective use for convective-scale radar data assimilation has been demonstrated in many studies (Kain et al. 2010; Rennie et al. 2011; Sun et al. 2012). Particularly, the efficiency of 3DVAR on analyzing radar radial velocity data has also been demonstrated by Gao et al. (2002, 2004) using the Advanced

Regional Prediction System (ARPS; Xue et al. 1995, 2000, 2001) 3DVAR package. Radar only observes few parameters, which are insufficient by themselves to determine a complete set of initial conditions (ICs) for NWP model use. Furthermore, for the lack of flow-dependent background error cross covariance in the 3DVAR formulation, many unobserved states cannot be directly analyzed using 3DVAR from the limited observed variables. The "complex cloud analysis," such as the one available within the ARPS 3DVAR system, employs certain physical constraints that create the linkage between radar observations and model state variables to overcome the observation deficiency problem. The cloud analysis is usually performed as a separate step from the 3DVAR analysis (Hu et al. 2006a, b).

In general, cloud analysis procedures construct three-dimensional cloud and hydrometeor fields making use of radar reflectivity data along with other satellite and surface cloud observations when available. Information in the analysis background, which in the ARPS case, is the result of the 3DVAR analysis, is also used. In the ARPS complex cloud analysis, in-cloud temperature and moisture are also adjusted based on semi-empirical rules. In many previous studies, the ARPS complex cloud analysis has been applied to various convective weather systems, including tornadic thunderstorms (e.g., Hu et al. 2006a), mesoscale convective systems (MCSs; e.g., Dawson and Xue 2006), and hurricanes (e.g., Zhao and Xue 2009). Given its effectiveness with relatively low computational requirement, the ARPS cloud analysis has been used, along with the 3DVAR radial velocity and other observations, for real-time storm-scale forecast over the continental U.S. domain since 2008 (Xue et al. 2008) for the NOAA Hazardous Weather Testbed (HWT) Spring Experiments (Kain et al. 2010; Xue et al. 2013). With

cloud analysis, the typical precipitation spin-up problem is mostly alleviated (illustrated in FIG. 1.1, by the initial ETS difference between c0, without cloud analysis, and cn, with cloud analysis; also addressed in Dawson and Xue 2006).

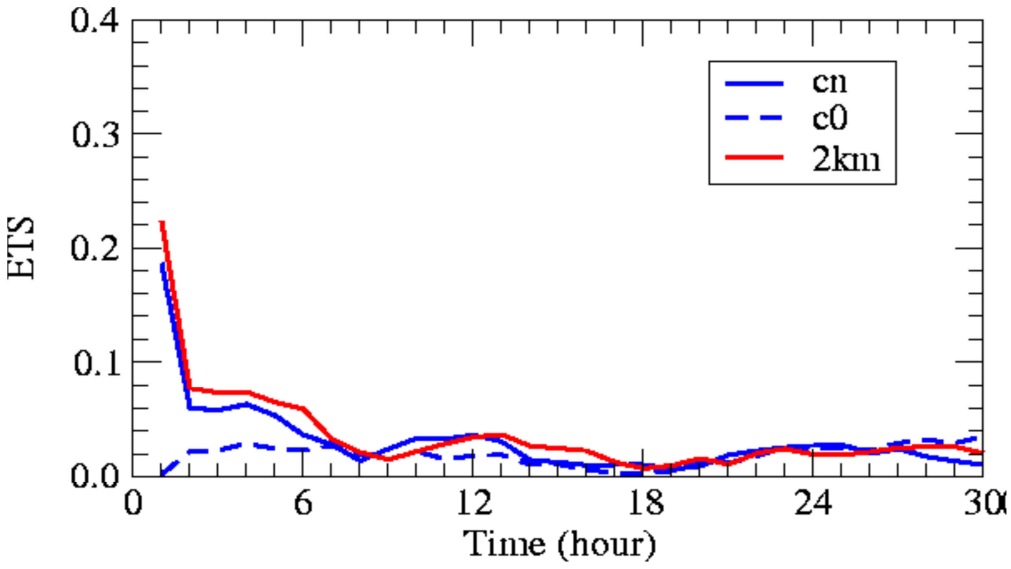

FIG. 1.1 Equitable threat score (ETS) of hourly precipitation at 0.5 inch threshold averaged over the last 15 days of 2008 Spring Experiment. Experiments with grid spacing of 4 km and 2 km are denoted by blue and red color, respectively. Dash line indicates experiment with no radar analysis. Adapted from Xue et al. (2008).

Despite some successes as demonstrated by previous studies, the cloud analysis approach still has its issues. As stated by Auligne et al. (2011), a summary paper of the International Cloud Analysis Workshop (2009), “Several cloud analysis and nowcasting systems are now operational, yet forecasts are still usually only useful for a few hours.” The difficulties, or limitations, can be mainly attributed to the inconsistency between the semi-empirical based analysis result and the complicated model physics: while the analyzed states from the cloud analysis are not consistent with the prediction model, they usually undergo rapid adjustments, and as a result, the impact of the cloud analysis

is eliminated quickly during the initial stage of forecast. This process is commonly reflected by the verification of the forecast, as shown in FIG. 1.1, with a rapid drop of the ETS in the very first hour after the forecast initialization.

Although the impact of the ARPS cloud analysis has been examined in many real case studies, because the truth of cloud and hydrometeor fields is little known, the accuracy of analyzed fields are difficult to determine. In many cases (Dawson and Xue 2006; Hu and Xue 2007; Zhao and Xue 2009b), the cloud analysis was applied with the 3DVAR analysis through intermittent assimilation cycles, in which the accuracy of the analyzed fields is further complicated by the model integration involved. The impact of individual analyzed cloud and hydrometeor fields, as well as the associated adjustments to temperature and moisture has not yet been carefully examined so far. It is our goal, in this dissertation, to investigate the impact of the accuracy of individual state variables in the initial conditions, particularly those variables that are adjusted by the cloud analysis, on the subsequent forecasts. Such study is best done using Observing System Simulation Experiments (OSSEs) where the truth of all state variables is known, so that the accuracy of the analyzed fields can be measured quantitatively. A study that examined a similar issue is that of Ge et al. (2013); however, in their study the individual state variables were examined as potential observations available over the entire model domain, and intermittent 3DVAR analyses were used. The main differences between Ge et al. (2013) and our OSSE study are summarized in Table 1.1.

Table 1.1 Summary of the differences between Ge et al. (2013) and this study

	This study	Ge et al. (2013)
Background fields	3D smoothed fields derived from the truth simulation of OSSE (real case based).	Homogeneous fields given by an idealized sounding.
ICs construction (DA) method and effective area	Direct insertion over entire domain or from ARPS complex cloud analysis for in-cloud regions.	3DVAR (with mimicked observation error) over entire domain.
Impacting variable examined	θ, q_v, q_x (mixing ratios of cloud and precipitation species).	V_h, w, θ, q_v, q_r (rain water mixing ratio).
DA frequency	One time.	Cycled analysis for 90 minutes.
Microphysics	Double-moment ice microphysics scheme.	Warn rain only.

Questions addressed in this dissertation include:

- How accurate is the analysis required to be for accurate predictions?
- What the role does the model error play? How large is the impact of model error relative to initial condition error?
- How long can the benefit of cloud analysis last? Is there an intrinsic limit?
- What is the relative importance of the different variables in the initial conditions on prediction?

By answering these questions through the investigation, a better understanding of the potential and limitations of the ARPS cloud analysis or other similar package can be gained. In addition, this study can serve as a guide for further cloud analysis improvement.

1.2 An Overview of the Study

The rest of the dissertation is organized as follows: At the beginning of Chapter 2, a brief overview of various existing cloud analysis systems implemented by different operational forecasting centers is provided. A more detailed introduction to the current ARPS complex cloud analysis package is then given, along with the modifications to the hydrometeor mixing ratio analysis procedure implemented in this study. The revised analysis procedure is applied to an observed maritime monsoonal mesoscale convective vortex (MCV), and the resulting very-short-range (one hour) rainfall forecast is examined. In Chapter 3, after an introduction to the MCS test case and the OSSE framework, two sets of experiments are presented that explore the forecast sensitivity to different control factors. The factors examined include model error due to the use of a different microphysics parameterization scheme and errors in the model initial state variables. The second set of experiment examining the practical impact of the ARPS cloud analysis and corresponding in-cloud state adjustments is presented in Chapter 4. Experiment results are discussed and summarized with a conceptual model of forecast error evolution at the end of the chapter. In Chapter 5, based on the findings from Chapter 4, the potential effectiveness of an accurately specified moisture initial condition on the model forecast is firstly tested and demonstrated. A modified in-cloud moisture adjustment procedure, making use of the vertical velocity information, is further proposed, followed by the preliminary evaluation of its efficacy. Finally, conclusions of the study are summarized in Chapter 6. Possible future work is also discussed.

Chapter 2: Cloud Analysis and a Real Case Application

2.1 Existing Cloud Analysis Systems and Algorithms

A number of analysis and forecast systems have been developed and implemented operationally for nowcasting or short-range forecasting use at various NWP centers or research organizations around the world over the past two decades. These systmes include the Local Analysis and Prediction System (LAPS; Albers et al. 1996) developed by the National Oceanic and Atmospheric Administration's (NOAA's) Forecast Systems Laboratory (FSL), the Nowcasting and Initialisation for Modelling Using Regional Observation Data Scheme (NIMROD; Golding 1998) by the United Kingdom Meteorological Office (UKMO), and the Rapid Refresh version of the Rapid Update Cycling model (RUC/RR; Benjamin et al. 2004) used for current operations at the National Center for Environmental Prediction (NCEP). A brief overview of these systems, in particular their cloud analysis component, will be provided as follows.

As one of the first systems that carry out the analysis of cloud-related fields, LAPS was designed to incorporate a variety of datasets, including surface observations, remote sensing observations (e.g., Doppler radars, satellites), multiple layer data (e.g., wind and temperature profilers), and aircraft reports, for NWP model use. The three-dimensional cloud distribution is retrieved based on the prerequisite 3D temperature analysis and the insertion of satellite and radar data. Other 3D cloud products of LAPS include cloud type, mean volumetric drop (MVD) size, in-cloud omega field (i.e., vertical velocity), and cloud liquid water/ice content derived using the Smith-Feddes model (Haines et al. 1989). Besides, the radar reflectivity data along with analyzed wet-bulb temperature serves as input for diagnosing 3D precipitation type. Most cloud

analysis procedures described above are inherited by the ARPS complex cloud analysis, whose details are provided in the coming subsection. At present, LAPS is still widely utilized in the weather agencies of several countries (e.g., China, Finland, Italy, Korea, Serbia, Spain, and Taiwan. Refer to http://laps.noaa.gov/).

For the UKMO's very short range forecasting needs, the NIMROD has been developed by integrating nowcasting and NWP techniques. Being one of the three major components, precipitation, cloud, and visibility, of the NIMROD system, the cloud analysis scheme utilizes the Meteosat satellite imagery as the main observation source, in conjunction with the surface reports. Firstly, the clear and cloudy regions are identified with the available satellite observations. Cloud top height is then calculated based on the atmospheric structure from the NWP model output, which processes the infrared (IR) radiance temperature information used to account for the relative location of the cloud top to the boundary layer height. Finally, the multi-level cloud analysis is obtained by applying a two-dimensional recursive filter algorithm (Purser and McQuiqq 1982) to each model level that brings best agreement among the satellite observation, surface cloud report, and the forecast first guess. Information of both cloud fraction and rain rate analysis (derived from radar and satellite observation) can be further used for humidity specification (Macpherson et al. 1996).

Since the first operational implementation in 1994, the RUC system has undergone a few updates, mainly in the aspects of application of finer model resolution and higher frequency on data analysis. The most current version of RUC, launched beginning in 2002, comes to a hourly assimilation cycle with 20-km horizontal spacing. Both the optimal interpolation (OI) and 3DVAR techniques are available in the RUC

system for assimilating a large variety of observation types (refer to Table 2 in Benjamin et al. 2004 for a complete list). The cloud/hydrometeor analysis component in RUC was first designed mainly using the Geostationary Observational Environmental Satellite (GOES) data, but was further modified to include the radar reflectivity data (Kim et al. 2002). Cloud clearing (i.e., removal) or building (i.e., insertion) is carried out based on the GOES observation in comparison with the background cloud field (1-h forecast from previous run). The water vapor mixing ratio is also adjusted throughout this process. Further hydrometeor mixing ratio adjustment has been proposed: the background (predicted) hydrometeors are used for partitioning the contribution on reflectivity from each hydrometeor species, and the observed reflectivity is complied with the reflectivity observation operators from Rogers and Yau (1989). A similar concept on using the hydrometeor predictions (when available) is also adopted in ARPS cloud analysis for the cycled analyses.

Efforts have been made by different groups of people to assimilate radar reflectivity data for hydrometeor analysis in a research scenario. In Sun and Crook (1997), assimilation of simulated reflectivity data either directly or indirectly (with q_r as the control variable through a Z-q_r relation) was tested using 4DVAR technique. With the same Z observation operators used in Sun and Crook (1997), Xiao et al. (2007) developed a 3DVAR scheme using the total water mixing ratio q_t as the control that realizes analyses of q_r, q_c, and associated moisture and temperature fields. Both of these studies above, however, took only the warm rain process into account. Zhao and Jin (2008) introduced a variational approach in which a gain factor, based on minimization

of the cost function with Z as the control variable, was used to update mixing ratios of multiple hydrometeor species (ice phase included).

Some algorithms, instead of realizing direct analysis of cloud/hydrometeor fields, are designed for updating other associated model states, such as temperature and moisture. One example is posed by the 1D+3DVAR method of Application of Research to Operations at Mesoscale (AROME; Seity et al. 2011) deployed in the Météo-France. With the application of a unidimensional (1D) Bayesian inversion, the treatment for the nonlinear moist processes is bypassed in favor of reflectivity assimilation. The observed reflectivity column is, at first, used to compute for the relative humidity profile, which is serving as a pseudo observation for the later 3DVAR assimilation. One of the advantages addressed for this two-step method is the possibility to control the quality of the 1D Bayesian retrievals before they are assimilated in 3DVAR with other observations.

Other non-variational based techniques, such as latent heat nudging (LHN) and diabatic digital filter initialization (DDFI), are also applied in operational forecasting for radar reflectivity assimilation. Based on the theoretically proportional relation existing between the resulting surface precipitation and the latent heating profile aloft, the model's temperature and moisture fields are "nudged" so that the diagnosed precipitation rate can better agree with the observation. Jones and Macpherson (1997) introduced the implementation of the LHN technique into the UKMO Mesoscale Model through the use of the radar-derived precipitation data is introduced. As the trend of increasing DA cycling frequency is used for convective-scale forecasts, the issue of imbalance among the analyzed fields, the spurious inertial-gravity wave specifically,

reveals and demands for appropriate treatments. The DDFI technique was first presented in Huang and Lynch (1993) as an ideal solution to this issue. In conjunction with the cloud analysis procedure in the RUC, a new radar reflectivity assimilation procedure using the DDFI is proposed in Weygandt et al. (2008). Basically, the observed-reflectivity-based latent heating rate is computed to modify the model-calculated temperature tendency during the diabatic forward integration part of the digital filter.

More simple and straightforward methods can be applied to adjust the in-cloud states. For example, a commonly used assumption that humidity is saturated in the cloudy regions is adopted widely in many studies (Albers et al. 1996; Zhang et al. 1998; Wang et al. 2013) for in-cloud moisture adjustment simply with the presence of echoes.

2.2 The ARPS Complex Cloud Analysis

2.2.1 An Overview of Current Complex Cloud Analysis in the ARPS

Serving as a major part in the ARPS Data Analysis System (ADAS; Brewster 1996), the complex cloud analysis module was designed to provide optimal analyses of hydrometeor and other associated fields for NWP model use. Since the analysis module was firstly developed by Zhang et al. (1998) based on the LAPS (Albers et al. 1996), several modifications and improvements have subsequently been made, including the important temperature and moisture adjustments (Brewster 2002). In the most current version of ARPS (5.3.5), ADAS is able to incorporate information from various sources of observation, such as single layer measurements (e.g., mesonet, airport report, buoy), multi-layer measurements (e.g., radiosonde), and remote sensing observations (e.g., satellite and radar). In this study, the focus is on radar data, whose impact on model

predictions has been demonstrated as primary in a present study for its relatively fine spatial resolution (Schenkman et al. 2011).

The complete procedure of the current ARPS complex cloud analysis is described step by step in detail below. Again, only contents that use the radar observation are addressed.

(i) State variables initialization:

All model state variables that will be used in the cloud analysis procedure, including pressure (p), potential temperature (θ), moisture (q_v), vertical motion (w), and mixing ratios of various cloud and precipitating hydrometeors (q_x), are firstly initialized by reading from either analysis fields or forecast fields from a previous model prediction. Note that for most analysis data, q_x fields are usually unavailable.

(ii) Cloud coverage analysis:

A background three-dimensional cloud cover field is first calculated from the background relative humidity (RH) analysis. In general, the cloud coverage is a function of humidity and height. For details of the formulation, please refer to Zhang et al. (1998). After the background cloud cover field is constructed, a series of cloud insertion is performed based on observations that are available.

As the radar observed reflectivity is remapped onto the model grids, the clouds are directly inserted (i.e., 100% cloud fraction assigned) into grids above the lifting condensation level (LCL), which can be determined from background temperature and humidity, or simply offered by the airport weather reports (i.e., METARs) if available.

(iii) Cloud associated variables analysis:

From the cloud distribution obtained in the previous step, cloud base and cloud top can be determined. Along with the background information of pressure and temperature at the cloud base, the liquid water content (i.e., cloud water mixing ratio q_c) throughout the entire cloud extent can then be calculated based on an adiabatic assumption. Another option adapted from the Smith-Feddes model (Haines et al. 1989) is available. With this model, a prevailing stratus cloud environment is assumed. Ambient temperature from the background is used to account for the depletion process of cloud water in forming cloud ice (i.e., q_i). In addition, effects of entrainment and dilution by glaciation are also included. Modifications of the Smith-Feddes model inherited in the ARPS cloud analysis are introduced in Albers et al. (1996),.

As the end of this these, other cloud-associated variables, such as in-cloud vertical motion (w_{cld}) and icing severity index, are calculated with. w_{cld} is a function of cloud thickness and cloud type. The cloud thickness is obtained from the cloud extent, while the cloud type can be determined by temperature and stability. The icing severity index is a function of temperature, liquid water content, cloud type and precipitation type. The determination of precipitation type in the current cloud analysis will be further described in the next subsection.

(iv) Cloud mass limit 1:

When there is significant cloud water or cloud ice present and their total mixing ratio is larger than the local saturated water vapor moisture (i.e., q_v^*), their summation is limited to q_v^* by reassigning their values based on their original ratio as

$$q_c(\text{new}) = \frac{q_c(\text{original})}{q_c(\text{original}) + q_i(\text{original})} q_v^* ,$$

$$\text{and} \quad q_i(\text{new}) = \frac{q_i(\text{original})}{q_c(\text{original}) + q_i(\text{original})} q_v^* \,. \tag{1}$$

(v) Precipitation mass analysis:

This step serves as the major part of the entire cloud analysis procedure that directly links the model hydrometeor state with radar reflectivity observation. To achieve the hydrometeor analysis, a set of radar observation operators and their inversed version are required. A number of observation operators have been developed for simulating reflectivity from model predictions. These operators primarily depend on the microphysical process and the associated features. Two sets of observation operators are currently available in the official version of ARPS. The first set of operators is relatively simplified based on the fitting results between model simulation and radar observations. Empirical exponential relationships in this option are given by Kessler (1969) for rain water and Rogers and Yau (1989) for snow and hail. This set of operators is denoted by KRY hereafter. The other set of operators, given by Ferrier et al. (1995), is constructed with more complicated formulation that involves the melting process of snow. Note that both sets of operators described above include only three precipitation species: rain, snow and hail. Furthermore, both of them are currently compatible with the single-moment (SM) bulk microphysics parameterization scheme only as the default constant intercept parameter N_0 is used.

The process to retrieve the simulated radar observations, such as reflectivity, is usually relatively easy and straightforward: after various hydrometeor mixing ratios from the model output are inserted into their respective reflectivity operators, the reflectivities for different species are then combined (summed up) as the simulated

reflectivity. The inverse process is, however, relatively complicated. As this problem itself is under-determined with only one known variable (i.e., observed reflectivity) but multiple unknowns (i.e., mixing ratio of different species) to be solved, additional information is required. How to partition one observed gross reflectivity into several portions corresponding to different precipitation species that are present is a major problem one will encounter while realizing the mixing ratio analysis. As noted earlier in the first step, the hydrometeor fields are usually unavailable in most analysis data, no information about the presence of hydrometeors can be obtained from the background fields. Consequently, a "mutual-exclusive-presence" condition is applied as a prompt resolution. Under this condition, there is only one dominating species on each analysis grid and the observed reflectivity is contributed by it completely. In other words, mixing ratio of one and only species can be analyzed for each grid. More related discussions are provided in the next subsection.

(vi) Cloud mass limit 2:

After the precipitation mixing ratios are analyzed based on radar reflectivity, cloud mixing ratios in regions of precipitation are gone through another limitation process for avoiding double counting. For now, a simple five percent is taken upon the total precipitation mixing ratio in representing the total cloud mixing ratio while the amount of precipitation analyzed is found more significant than the amount of cloud.

(vii) In-cloud temperature adjustment:

Before this point, the analysis of all hydrometeors is completed. Following are optional adjustments of in-cloud state variables based on the hydrometeor analysis and background state.

Two major in-cloud temperature adjustments are available in the current cloud analysis package. One adjustment is based upon the latent heat release associated with the hydrometeors that have been analyzed (Zhang 1999; referred to as the LH scheme), and the other one is based on assuming moist adiabatic temperature profile including the dilution effect due to the entrainment process (Brewster 2002; named herein the MA scheme). The impact of two schemes on the prediction of a tornadic thunderstorm is discussed in Hu and Xue (2007).

(viii) In-cloud moisture adjustment:

Currently, wherever there is radar echo present, the moisture for that local grid is simply set as saturated. This adjustment is based on an intuitive physical sense that moisture should be saturated for forming precipitation. The process is completed by assigning 100% RH, and then calculating q_v along with information of saturated moisture q_v^*, which is a function of local pressure and temperature (after the temperature adjustment if it was applied earlier).

For the case when the background hydrometeor information is available, a different option of moisture adjustment that slightly reduces the moisture can be selected. The activation of this adjustment is determined by comparing the total hydrometeor mass (all cloud species and precipitation species) from background and from analysis. When the analysis value is found to be less than the background value, q_v is set to 0.95 q_v^*. This procedure is designed for intermittent analyses (i.e., cycling) to avoid an over-moist environment and the resulting overforecast of precipitation.

(ix) In-cloud vertical motion adjustment:

As the final step of the cloud analysis procedure, the in-cloud vertical motion is adjusted to the larger value of either background w or w_{cld}, which is analyzed in step *(iii)*.

Table 2.1 is provided as a concise summary of the cloud analysis procedure described above.

Table 2.1 Summary ARPS complex cloud analysis procedure

Step		Content	State variables changed
1	State variables initialization	Model state variables (p, θ, q_v, w, q_x) read from background files.	None.
2	Cloud coverage analysis	Cloud coverage and cloud distribution variables (cloud base and cloud top) analyzed based on Z_{obs}.	None.
3	Cloud associated variables analysis	1) Cloud mass variables analyzed based on p_{bg}, θ_{bg}, and other cloud info (from step 2). 2) In-cloud vertical velocity (w_{cld}) analyzed based on cloud type and thickness.	q_c, q_i.
4	Cloud mass limit 1[#]	Cloud mass variables adjusted to confine to background q_v^*.	q_c, q_i.
5	Precipitation mass analysis[#]	Precipitation mass variables analyzed based on Z_{obs} using radar simulator formulation selected.	q_r, q_s, q_h.
6	Cloud mass limit 2	Cloud mass limited to 5% of precipitation mass in avoiding double counting.	q_c, q_i.
7	In-cloud temperature adjustment[#]	Temperature adjusted in selected physical manner (LH or MA).	θ.
8	In-cloud moisture adjustment[#]	1) Moisture saturated for grid with observed echo. 2) q_v limited to $0.5q_v^*$ for grids with analyzed total mass less than background total mass.	q_v.
9	In-cloud vertical motion adjustment[#]	w reassigned to the larger value between w_{bg} and w_{cld}.	w.

2.2.2 A Modified Mixing Ratio Analysis Procedure

As introduced in the previous section, the mixing ratio analysis procedure available in the current ARPS complex cloud analysis package is relatively simple. In other words, the physics involved are not sufficient in depicting realistic mechanisms and therefore may provide unbalanced analysis results that are incompatible with the complicated model microphysics schemes. As a result, the effect of analysis will not be able to last long as the model goes through a rapid adjustment.

Our study has developed a more general procedure to derive an analysis of the mixing ratios. This procedure is based on the radar operator built by Jung et al. (2008; referred to as JZX hereafter). Four major features that distinguish our approach from the currently utilized procedure are described below:

(i) Unlike the empirical fitting relationships used for developing the KRY operators, the JZX formulation includes the theory of electromagnetic wave propagation and scattering. Factors that affect the scattering results are considered in the derivation; for instance, the dielectric factor and canting behavior as the particle falls. Since the Rayleigh approximation is applied while formulating for the large sized particles such as hailstones, this procedure is currently good for assimilating radar data at long wavelengths (i.e., S band) only.

(ii) Compared to the simple exponential relation between reflectivity and hydrometeor mixing used in KRY, the drop size distribution (DSD) parameters corresponding to the hydrometeors are also included in expressing the radar variables, making this procedure more flexible and therefore compatible with the model using multi-moment (MM) microphysics schemes.

(iii) Although the melting process of snow is included in the Ferrier operators, this classifying criterion is purely based on temperature with an arbitrary threshold of 0 °C. As much more complicated microphysics and various hydrometeor phases can be expected for their existence in the real atmosphere, a melting ice model is included in JZX to account for sufficient variety of physical properties associated with the melting process (e.g., density change). With this model, the radar variables are not only contributed by the pure precipitating species (e.g., rain, snow, hail), but also by the mixing species (or mixtures, e.g., wet snow, wet hail) if present.

(iv) Considering that different combinations of precipitating species can be used in different NWP models and microphysics schemes, an equation set for graupel species is added to the original published JZX operators, which included only rain, snow, and hail. This addition allows the cloud analysis procedure to handle situations where both hail and graupel species are present.

As mentioned in the previous section, perquisite information about the distribution of multiple hydrometeor species is required before we can retrieve the corresponding mixing ratios based on the Z operators. In the current cloud analysis package, a simple strategy is used to classify for the hydrometeor type based on observed Z and background T when no hydrometeor field is available in the background:

$$\text{If } Z_{obs} \geq 50 \text{ dBZ} \rightarrow \text{pure hail is classified,}$$

$$\text{If } Z_{obs} < 50 \text{ dBZ, and} \begin{cases} \text{If } T_{wb} \geq 1.3℃ \rightarrow \text{Pure rain is classified} \\ \text{If } T_{wb} < 1.3℃ \rightarrow \text{Pure snow is classified} \end{cases}'$$

in which T_{wb} is the wet bulb temperature. After the hydrometeor type is determined, corresponding equations of Z operators is used to compute for the mixing ratio. With this strategy, only one type of hydrometeor can be found for each analyzed grid, which

is believed unrealistic compared to what is observed in the real atmosphere. Since one major advantage of our modified mixing ratio analysis procedure is the allowance of microphysical complexity (by implementation of the melting model), it is designed to enable the analysis result of a more flexible hydrometeor distribution. To realize our analysis with this modified procedure, the ratio among q_x of each pure precipitation species (i.e., rain, snow, graupel, and hail) is required in advance. As long as there is hydrometeor information available in the background field (usually from previous model forecasts), a more realistic hydrometeor analysis and accompanying microphysical features can be anticipated with our modified procedure.

Details about the formulation with associated parameters and coefficients, and how to perform this modified procedure for mixing ratio analysis in practice can be referred to Appendix A. Although there are observation operators built for other polarimetric variables (e.g., Z_{DR}, K_{DP}) in Jung et al. (2008a), only the reflectivity operators are adopted in this study to analyze the mixing ratios for its robustness of behavior to various hydrometeors, which also provides us confidence in the analysis results. Operators of other polarimetric variables could also be used; however, comprehensive understanding about the sensitivity of these variables to different hydrometeors and a thorough data quality control process are highly recommended before actual application.

2.3 The Use of Polarimetric Radar Measurements in the Cloud Analysis

2.3.1 Mixing Ratio Analysis Using Polarimetric Radar Variables

Given the additional measurements that polarimetric radar can provide, its advantage over the traditional Doppler radar in better characterizing the hydrometeor

features and their corresponding microphysical processes has been widely discussed and demonstrated in numerous present studies, particularly in the field of quantitative precipitation estimation (QPE; Bringi and Chandrasekar 2001; Vivekanandan et al. 1999; Zhang et al. 2001; Zrnic and Ryzhkov 1996). Toward the goal of improved short-range forecasts of cloud, hydrometeor, and precipitation, a modified mixing ratio analysis procedure that makes use of multiple polarimetric radar variables is proposed.

The JZX reflectivity operator as described in previous section is used to carry out the procedure. The major role of the extra polarimetric variables, in addition to *Z*, is to partition the portions of multiple precipitation species required as the prerequisite for the mixing ratio analysis. A fuzzy-logic based hydrometeor classification algorithm (HCA) proposed by Park et al. (2009) is adopted. Variables used for the HCA procedure includes Z, Z_{DR}, K_{DP}, and ρ_{hv}. These measurements are firstly interpolated to the model gridded coordinate. For grids where all four variables are available, the aggregation value A_i for each possible defined class of radar echo is computed as

$$A_i = \frac{\sum_{j=1}^{4} W_{ij} P^{(i)}(V_j)}{\sum_{j=1}^{4} W_{ij}},$$

where *i* represents the *i*th class of echo that could be classified by the algorithm, *j* represents the *j*th of radar variables, $P^{(i)}(V_j)$ is a trapezoidal shape membership function that characterizes the distribution of the *j*th variable for the *i*th class (shown as FIG. 2.1), and W_{ij} is a discriminating efficiency based weight between 0 and 1 assigned to the *i*th class and the *j*th variable. As a result, A_i values ranging from 0 to 1 for ten classes: 1) ground clutter (GC); 2) biological scatterers (BS); 3) dry aggregated snow (DS); 4) wet snow (WS); 5) ice crystals (CR); 6) graupel (GR); 7) big drops (BD); 8) light to moderate rain (RA); 9) heavy rain (HR); and 10) rain/hail mixture (RH) are obtained.

For specific values of W_{ij} or the X1, X2, X3, and X4 in $P^{(i)}(Vj)$, please refer to Park et al. (2009).

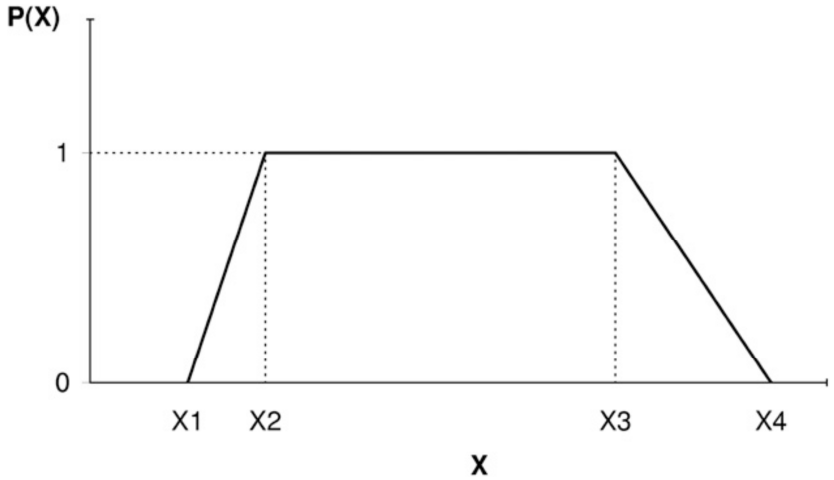

FIG. 2.1 Trapezoidal membership function, where X is an arbitrary radar variable. Adapted from Park et al. (2009).

In our adoption described above, couple simplifications upon the (Park et al. 2009)'s original proposal have been taken in calculating the aggregation values. First, two texture parameters SD(Z) and SD(Φ_{DP}) (along radial fluctuation of Z and Φ_{DP}, respectively) are excluded. As these two variables are mainly included to identify the non-meteorological echo, the impact of this omission on the classification results can be minimized by pre-processing radar data with some quality control (QC) algorithms (Hubbert et al. 2009). Second, the Q_j, confidence vector, present in both numerator and denominator of the original A_i equation is also omitted. As the Q_j is designed to account for the measurement error of each variable used, even confidence on each variable is accordingly implied while this simplification is taken.

After the A_i values are obtained, the results are further examined by some empirical hard thresholds (Table 2.2) to suppress apparently unrealistic class designations. For example, the radial velocity V interpolated on model grids is used to

eliminate the likelihood of the occurrence of ground clutter: when V is greater than 1.0 m s^{-1}, A_1 (1 is the order number for GC class) is directly set to 0. The rules are based on both physical model and observations (Straka et al. 2000).

Table 2.2 Empirical hard thresholds used to suppress apparently wrong designations (reproduced from Park et al. 2009)

Variables	Thresholds	Suppressed class
V	> 1.0 m s^{-1}	Ground clutter (GC)
ρ_{hv}	> 0.97	Biological scatterers (BS)
Z_{DR}	> 2 dB	Dry snow (DS)
Z	< 20 dBZ	Wet snow (WS)
Z_{DR}	< 0 dB	Wet snow (WS)
Z	> 40 dBZ	Ice crystals (CR)
Z	< 10 dBZ or > 60 dBZ	Graupel (GR)
Z_{DR}	< $f_2(Z)$ - 0.3 *	Big drops (BD)
Z	> 50 dBZ	Light to moderate rain (RA)
Z	< 30 dBZ	Heavy rain (HR)
Z	< 40 dBZ	Rain/hail mixture (RH)

*$f_2(Z)$ is a function of Z (in dBZ) that can be found in Park et al. (2009).

It has been indicated that additional routines that account for factors such as relative location of radar sampling volume with respect to the melting layer (ML) and precipitation nature (i.e., convective versus stratiform) are required for better classification results (Heinselman and Ryzhkov 2006). In our procedure, the background temperature is used for locating the ML top (where T begins to drop below 0 °C) and a constant depth of 500 m below the ML top is used for defining the layer. Any non-meteorological class (GC or BS), WS, and RA are excluded above the ML top regions, where strict frozen condition is presumed. On the other hand, the intensity of observed Z profile is used to classify the precipitation type. The following simple empirical strategy is used:

For grids below ML bottom, $\begin{cases} \text{if } Z \geq 35\ dBZ \rightarrow \text{Convective.} \\ \text{if } Z < 35\ dBZ \rightarrow \text{Stratiform.} \end{cases}$

For grids within ML, $\begin{cases} \text{if } Z \geq 35\ dBZ\ and\ \text{Lower successive grid is Conv.} \rightarrow \text{Convective.} \\ \text{otherwise} \rightarrow \text{Stratiform.} \end{cases}$

For grids above ML top, $\begin{cases} \text{if } Z \geq 30\ dBZ \rightarrow \text{Convective.} \\ \text{if } Z < 30\ dBZ \rightarrow \text{Stratiform.} \end{cases}$

The condition to check the lower successive grid is applied to prevent potential contamination of bright band, which is known for great Z intensity. Snow classes (i.e., DS and WS) are excluded for convective precipitation while the convective hydrometeor types such like BD, GR, and RH are avoided in stratiform area.

After all despeckling processes described above are gone through and all physical unreasonable classes are avoided, the survivals of A_i are used for determining relative portion of different precipitation hydrometeors. All eight meteorological classes are classified into three types as:

1) Rain type: BD, RA, and HR.
2) Snow type: DS, WS, and CR.
3) Hail/Graupel type: GR and RH.

The A_i maximum of each type is taken for representing the portion of that specific type. Specifically, the ratio among rain, snow, and hail/graupel is determined as:

$$\max(A_7, A_8, A_9) : \max(A_3, A_4, A_5) : \max(A_6, A_{10}).$$

The mixing ratio of each type is then analyzed using the JZX reflectivity operator to comply with the Z observation. Refer to Appendix A for detailed mathematical formulation.

The principal assumption incorporated in this procedure is that the aggregation values calculated from HCA are quantitatively proportional to the hydrometeor content (i.e., mixing ratio). One main feature of the analysis result from this HCA-based

procedure is that coexistence of different hydrometeors is possible at a same location, which is believed more realistic. Demonstrations of the analysis result will be shown and discussed in the coming sections with a real case application.

2.3.2 A Mei-Yu Front Mesoscale Convective Vortex and Model Configuration

During the intensive observing period (IOP) 6 (1800 UTC 4 June to 1200 UTC 6 June) of the Southwest Monsoon Experiment (SoWMEX) and the Terrain-influenced Monsoon Rainfall Experiment (TiMREX), a joint Taiwan-United States field experiment (Jou et al. 2010) taking place in 2008 Mei-Yu season (Chen and Chang 1980), a MCV embedded in a quasi-stationary mei-yu front across the southern China and middle Taiwan was observed. As the MCV-associated convective system moved in, serious flood was resulted in the southwestern coastal area of Taiwan with nearly 200 mm precipitation in two hours (Lai et al. 2011). FIG. 2.2 shows the track of the MCV.

In addition to the four S-band Doppler radars operated by the Central Weather Bureau (CWB), the National Center for Atmospheric Research's (NCAR's) S-band polarimetric Doppler research radar (as S-Pol hereafter) was deployed at southwest coast of Taiwan for the SoWMEX/TiMREX project. The radars locations are provided in FIG. 2.3.

The ARPS model and its data assimilation system are used to examine the impact of the mixing ratio analysis procedure based on polarimetric variables (as described in previous section) on the very short-range (1 hour) precipitation forecast. The domain, as marked by the red square in FIG. 2.2, is designed to cover the Southeast Asia with Taiwan in the center of the domain (121 °E, 24 °N). Although the MCV of interest was located very close to Taiwan in our study period, our domain is created as

large as this to avoid any potential over-stressed forcing from the lateral boundary conditions (LBCs). A northern hemisphere Lambert Conformal map projection is used. The domain has 803 (x-direction) × 803 (y-direction) × 53 (z-direction) grid points in total with 2.5 km horizontal spacing and an averaged 420 m vertical resolution. Terrain-following and stretching vertical coordinate is used with the lowest level of 50 m AGL.

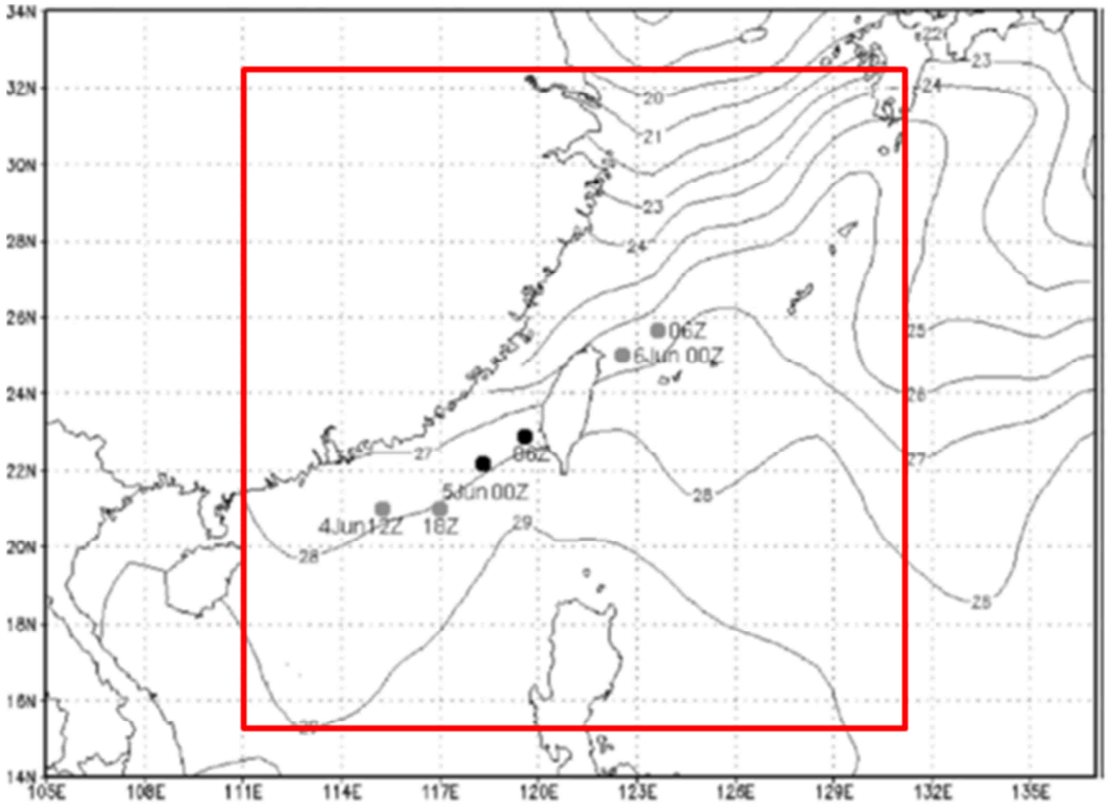

FIG. 2.2 Weekly averaged sea surface temperature during 2-8 June 2008 and MCV track. Gray dots and black dots are tracked by IR satellite images and radar radial velocity, respectively. Red square denotes the domain of our simulation. Reproduced from Lai et al. (2011).

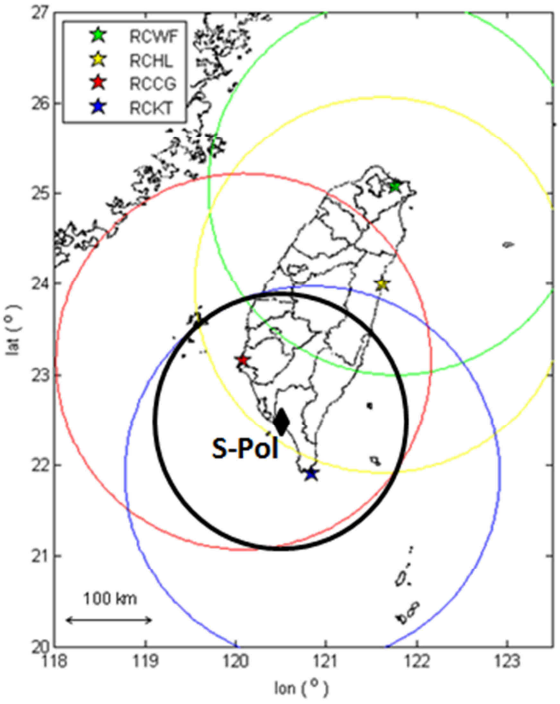

FIG. 2.3 Distribution of four CWB operational radars and NCAR S-Pol radar. Observing ranges are denoted by circles in corresponding colors (200 km for CWB radars and 150 km for NCAR S-Pol).

The simulation is initialized at 00 Z 5 June 2008 utilizing the CWB operational WRF analysis after interpolating from the original in 15-km grid spacing to our 2.5-km grids. The radial velocities (V_r) observed by S-Pol are assimilated using the ARPS 3DVAR package. Two sets of experiment are performed with different mixing ratio analysis procedures: one with current available procedure (based on *Z* only) using KRY operator, and the other with the HCA procedure (based on Z and other polarimetric variables) using JZX operator. Under each experiment, two microphysics parameterization schemes: Lin single-moment (Lin et al. 1983) and MY double-moment (Milbrandt and Yau 2005a, 2005b) are implemented; a total of four experiments are conducted (Table 2.3). To distinguish the impact purely owing to the

different mixing ratio analysis procedures, the other in-cloud field adjustments (T, q_v, and w) are turned off for all experiments. Other model configurations include: 1.5-order turbulence kinetic energy (TKE) scheme, atmospheric radiation transfer scheme, and stability dependent surface scheme. No convective cumulus parameterization is applied.

Table 2.3 Naming of experiments with corresponding settings

Microphysics \ q_x analysis	Z-based hydrometeor classification with KRY operator	HCA hydrometeor classification with JZX operator
Lin single-moment	KRY_S	JZX_S
MY double-moment	KRY_D	JZX_D

2.3.3 Results and Discussion

The radar reflectivity observed by the NCAR S-Pol at 00 Z 5 June 2008 are used for cloud analysis at the initial time of the simulation (FIG. 2.4). The leading convection of the MCV is just entering the S-Pol observing range at this time. However, the precipitating induced by MCV's outer circulation has reached the southwestern plain area of Taiwan. A meridional oriented cross section across the leading edge of most intense Z is selected for illustrating the mixing ratio analysis results.

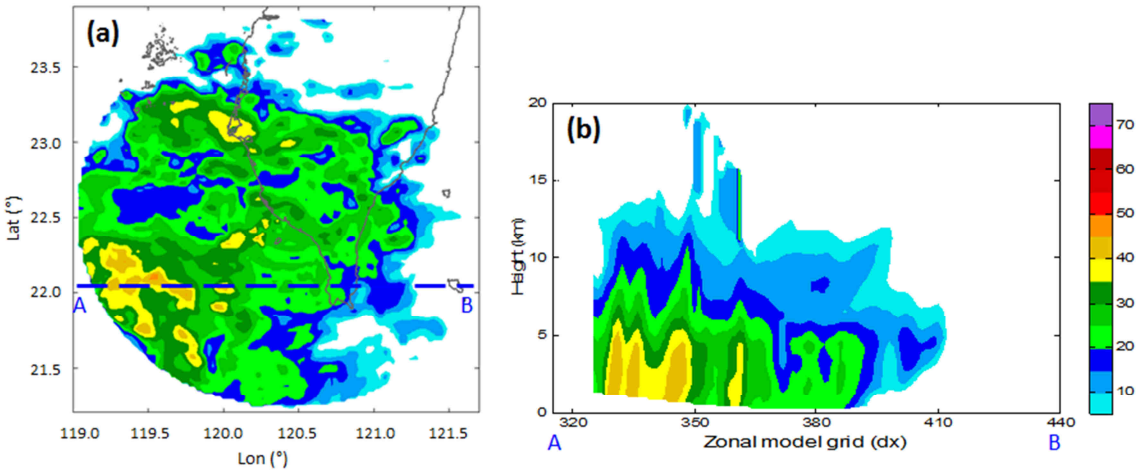

FIG. 2.4 (a) Composite reflectivity observed by NCAR S-Pol at 00 UTC 5 June 2008 and a (b) selected cross section **$\overline{AB}$**.

Mixing ratio analysis results using different hydrometeor classification procedures and reflectivity operators are shown in FIG. 2.5. Distinct differences can be found between two algorithms. Qualitatively, in terms of the rain distribution, it is found that the JZX analysis, with the HCA applied, is able to characterize the overshooting of the rain drops above the ML top, which is not available in the KRY analysis result, in which a nearly uniform cap is shown owing to the use of the background temperature. For the snow mixing ratio analysis, peak values show in the KRY analysis right above the ML top while in the JZY analysis these snow mixing ratio peaks are replaced by the overshooting rain and the significant q_s values are located slightly higher. A relatively broader distribution of the q_s analysis is found given by the JZY procedure, which is due to the different analyzing strategies used for the JZY and KRY procedures: in the KRY procedure, the mixing ratio analysis is carried out only when the observed Z exceeds 15 dBZ (for grids at 2 km or higher) while in the JZY procedure, the analysis of proceeds wherever the four radar variables (i.e., Z, Z_{DR}, K_{DP}, and ρ_{hv}) are available. A most significant difference between the KRY and JZY analyses is the presence of the hail. The complete absence of the hail species in the KRY analysis is mainly resulted from the simple strategy used to identify hails in the current analysis procedure: a 50 dBZ hard threshold (as described in the previous section). It is seen in the selected cross section (FIG. 2.4b) the maximum of Z observation is only around 45 dBZ, as a result, no hail is analyzed for the KRY. On the contrary, with the HCA used, higher likelihood of the hail occurrence is included in the JZX procedure through the introduction of the aggregation value calculation: some major presence of the hail is found within the intense convective cores.

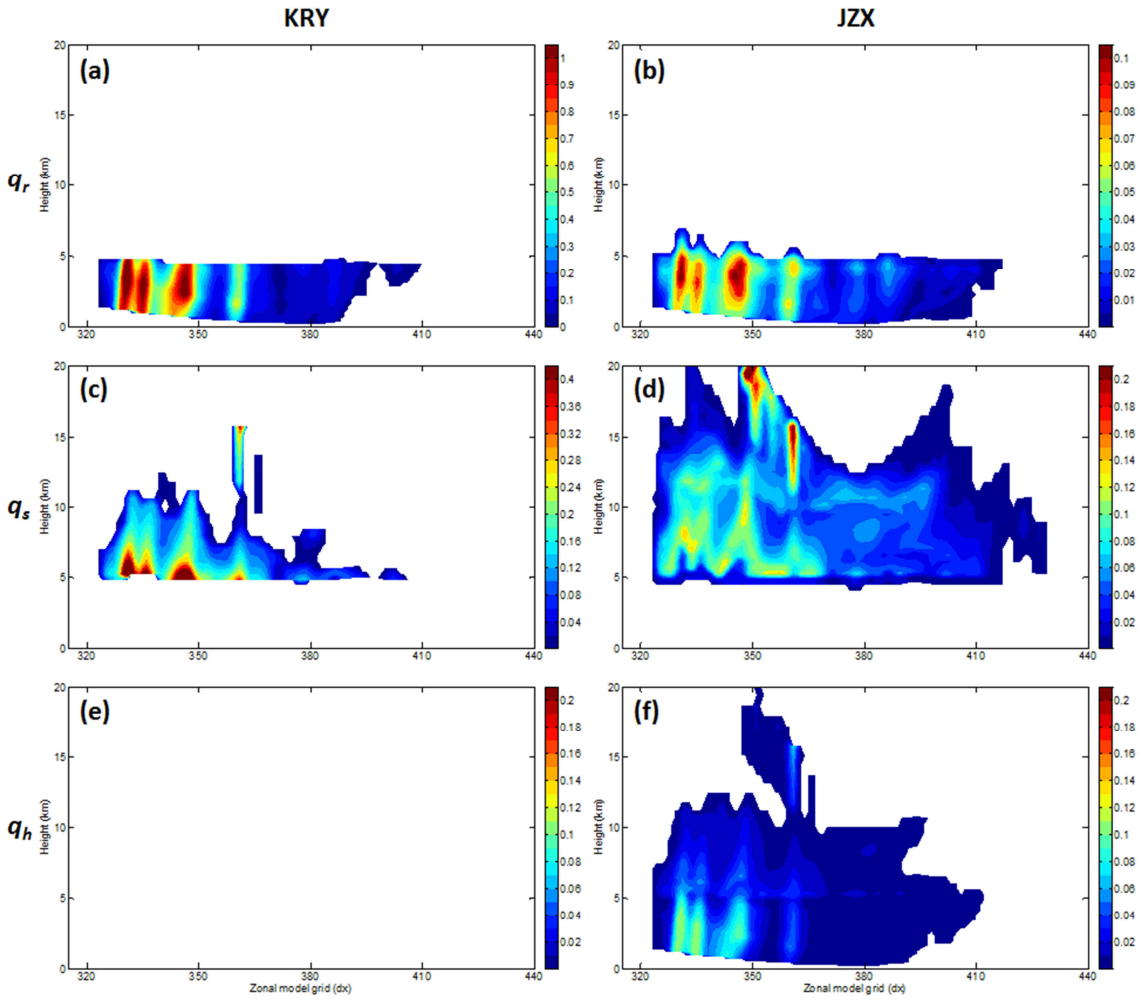

FIG. 2.5 Mixing ratio (g/kg) analyses for hydrometeor: (a)(b) rain, (c)(d) snow, and (e)(f) hail, using KRY (left panel) and JZX (right panel) procedure.

Other than the hydrometeor distribution, significant difference is also shown on the quantitative magnitude of the mixing ratio analyses given by the KRY and JZX procedure. In terms of q_r analysis, despite the generally similar distribution, the magnitude of q_r maxima of the JZX procedure (~0.1 g kg^{-1}) is found about an order smaller than that of the KRY procedure (~1.0 g kg^{-1}). This magnitude difference can be attributed to two main factors. First, as addressed earlier, the key advantage of the revised analysis procedure (i.e., JZX) is the inclusion of HCA that enables the analysis with coexistence of multiple hydrometeor species, which is also visualized by the

analysis results shown in FIG. 2.5b, d, and f. Unlike the traditional analysis procedure (i.e., KRY) that constructs mutually exclusive hydrometeor analysis and the only one single species is in charge of contributing the whole observed *Z*, the *Z* observation in the JZX procedure is partitioned by multiple hydrometeor species present one single grid based on the HCA. As a specific example, because of the coexistence with the hail above the ML, the snow mass content analyzed in the JZX procedure is smaller than its counterpart given by the KRY procedure, in which the snow is appointed with the whole contribution to the observed *Z*. The second factor is related to the melting model incorporated in the JZX operators: whenever liquid (i.e., rain) and iced species (i.e., snow or hail) coexist, the mixing ratios of these partially-melted iced species (i.e., melting snow or melting hail, or mixture) is calculated and their contribution to the *Z* is taken into account (refer to Appendix A for details). However, the contribution of these mixtures to the *Z* is "implicit" and therefore not able to be seen in our analysis results of the pure species. Nevertheless, the impact of these mixtures on reducing the magnitude of the mixing ratio analysis for the pure species is still retained. One demonstration of this effect can be found in FIG. 2.5b and f, where coexistence of the rain and falling hail occurs under the ML, inferring the one order smaller rain mass analysis from the JZY procedure in comparison with the counterpart from the KRY procedure is partially owing to the rain/hail mixture (or say, wet hail).

The one-hour forecast of the hourly rainfall given by all four experiments is provided with the CWB Quantitative Precipitation Estimation and Segregation Using Multiple Sensors (QPESUMS) hourly surface rainfall product, which is mainly derived from four CWB radar observation and ground checked (GCed) by the rain gauge measurements (direct to http://qpesums.cwb.gov.tw/taiwan-eng-html/index.html for details). The use of an observation independent from the source used for data assimilation (i.e., S-Pol) assures a more objective verification. Generally speaking, most experiments provide rainfall forecast coverage comparable to the observations except for the JZX_S, which produces too isolated intense precipitating cores with poorly-captured stratiform precipitation. On forecasting the major significant rainfall area on the open ocean (rainfall rate above 5 mm h^{-1}, shaded by dark green), it is found the experiments with the KRY procedure outperforms the ones with the JZX procedure by forecasting adequately wide coverage. To summarize the major difference between KRY and JZX forecast results (by comparing FIG. 2.6b to c and FIG. 2.6d to e), it is mainly shown on the prediction of the light rain. In a word, the JZX procedure with the HCA applied generally results in prediction of relatively weakened (in both intensity and coverage) stratiform precipitation but keeps proper intensity for the major convective precipitating cores. The rainfall forecast results of the similar distribution and intensity within two groups of microphysics experiments imply a greater relative importance of the microphysics scheme in comparison with the mixing analysis procedure applied. Furthermore, it is also found the experiments with the MY double-moment scheme are able to give prediction of the rainfall maximum much closer to the

observation while the Lin scheme turns to over-forecast the maximum rainfall with an over-100 mm exceedance.

From the one-hour forecast of the hydrometeor distribution in experiment KRY_S and JZX_S shown in FIG. 2.7, the domination of microphysics scheme over the mixing ratio analysis procedure can be further demonstrated. Quite similar results with only slight differences in mixing ratio magnitude are found for the two experiments just one hour into the forecast. Moreover, even with complete absence of hail analyzed at the initial time, the KRY_S can produce hail with both distribution and amount comparable to the JZX_S. Since the hydrometeor initialization given by different versions of analysis procedure fails to drive diverse hydrometeor forecast results through the model microphysics, we conclude a small sensitivity of the forecast to the mixing ratio analysis procedure difference.

Given the result from the revised hydrometeor analysis procedure does not provide better one-hour precipitation forecast in spite of the qualitatively more realistic hydrometeor analysis we believe it has provided, the possible uncertainties that could cause this result are further discussed. First of all, the central assumption used to build up our analysis procedure needs careful validation. As the aggregation values in the fuzzy logic-based HCA was original designed for determining a dominant (i.e., most likely) echo class in a radar sampling volume (in their application, only the class with largest aggregation value is confirmed), its appropriateness of quantifying the relative magnitude among multiple hydrometeors is questionable. Extra in-situ information such as the surface hail report may be helpful to evaluate the efficacy of the analysis.

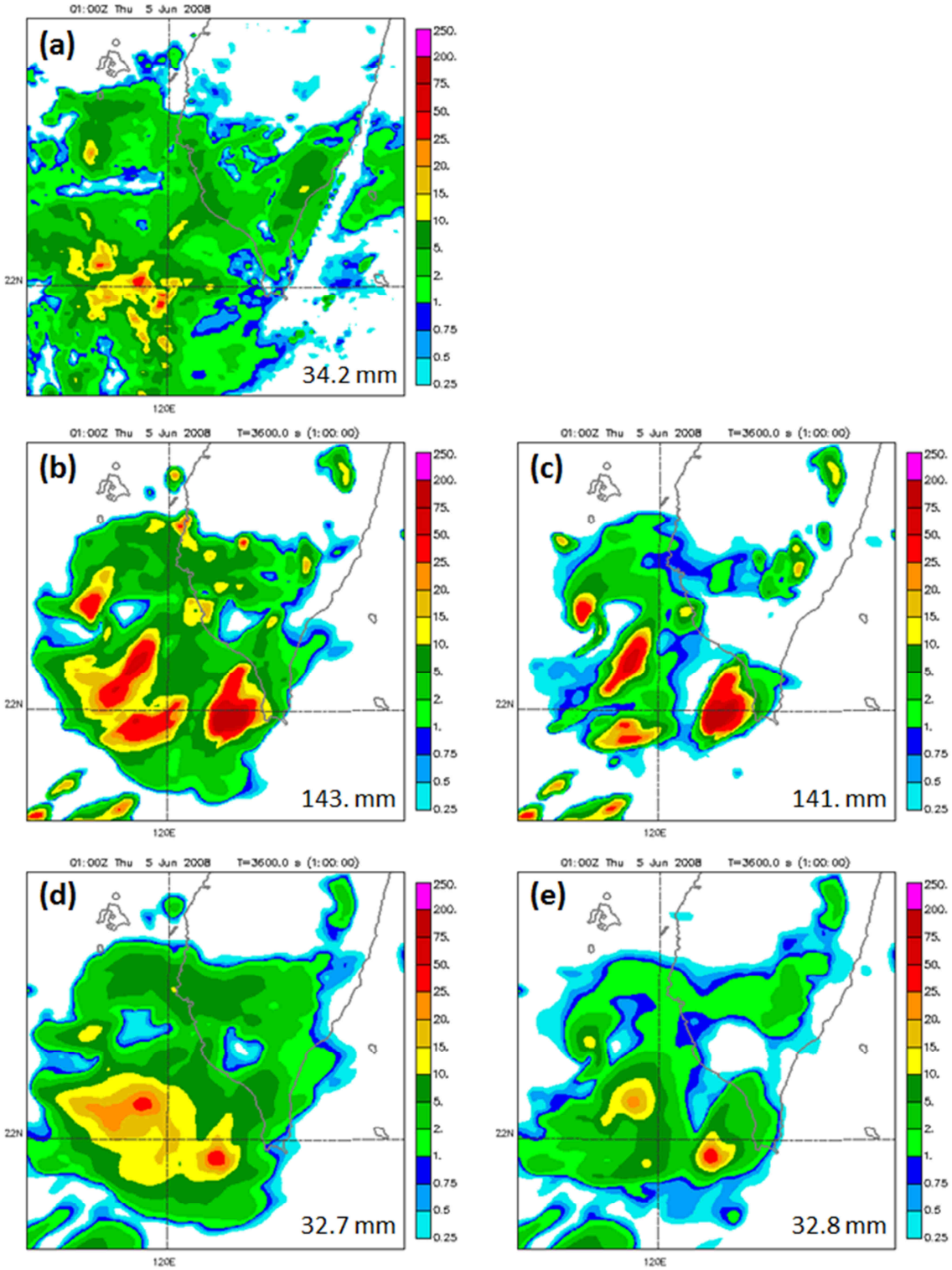

FIG. 2.6 Hourly rainfall accumulation (mm) of (a) CWB QPESUMS, (b) KRY_S, (c) JZX_S, (d) KRY_D, and (e) JZX_D valid at 01 UTC 5 June 2008. Hour rainfall maximum is written at the lower right corner of each plot.

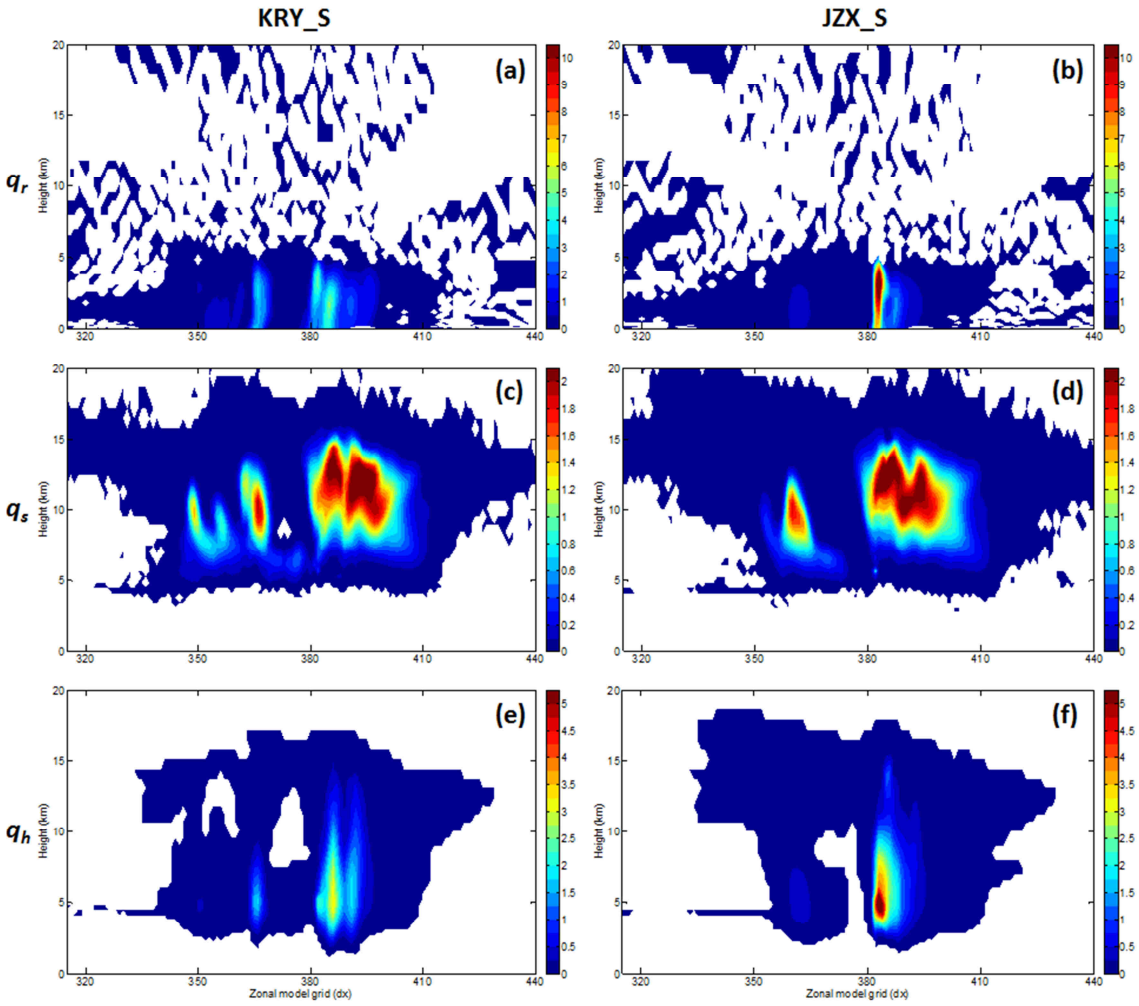

FIG. 2.7 One hour forecast of mixing ratio (g/kg) analyses for hydrometeor: (a)(b) rain, (c)(d) snow, and (e)(f) hail of experiment KRY_S (left panel) and JZX_S (right panel).

Other than the uncertainty of the validity of the analysis procedure itself, another issue could be its applicability on the case we examined. Essential difference of the precipitating mechanisms between the continental and maritime systems has been long and widely discussed (e.g., Pestaina-Haynes and Austin 1976; Phillips et al. 2007; Rosenfeld and Lensky 1998; Ulbrich and Atlas 2007; Wilson et al. 2011). To study the tropical MCV systems induced by the monsoonal flow, extra caution should be addressed while applying an analysis procedure in which certain assumptions based on

mid-latitude continental storm physics are applied. As a specific example, in a shallower developed (owing to the weaker updraft) maritime system where the warm rain mechanism plays a key role, excessive allowance of the presence of either surface hail or overshooting big drops could be unrealistic.

Moreover, it is also found from the preliminary examination that the sensitivity of the hydrometeor forecast to the initial analysis difference made by versions of procedure is relatively weak. It brings our consideration of the criticality of the initial hydrometeor accuracy. Since analyzing the hydrometeor content serves as a major part of the ARPS complex analysis, a comprehensive understanding of its actual effectiveness can guide us toward an efficient path to forecast improvements.

Many other error sources can result in the limitation of the hydrometeor analysis on the model forecasts in this real case study. For example, the model errors (or deficiency), in particular the microphysics scheme, can be responsible for the small sensitivity of the forecast results to the change of the hydrometeor initialization. On the other hand, possible improvement given by the hydrometeor fields through the analysis can also be limited by the poor accuracy of state variables at the initial time (i.e., IC uncertainty) of other non-hydrometeor fields such like winds, temperature, and moisture.

Motivated by the many remaining uncertainties revealed by this real case study reported here, further works presented in the following of this dissertation are carried on in the direction of better extracting and hopefully maximizing the benefit of cloud analysis on storm prediction.

Chapter 3: Observing System Simulation Experiments based on Direct Initial Variable Insertion

3.1 Introduction

Accurate quantitative precipitation forecasting (QPF) is critical because of the great impact on human lives and property. It is also a key input for models that predict water-related hazards (e.g., flooding and drought) and for monitoring near-future water resource availability (Vasiloff et al. 2007). The NWP models, in spite of their continuous advances, are still limited in providing accurate QPF, particularly for the warm season convective precipitation (Uccellini et al. 1999). One fundamental challenge can be attributed to the often poor initial conditions (ICs) of high-resolution forecasting systems, as well as the highly nonlinear physics and dynamics, as it was first pointed out by Lorenz (1963) and subsequently demonstrated by many studies based on practical applications.

A variety of radar data assimilation (DA) techniques in different degrees of complexity has been developed in recent decades for improved short-term convective storm predictions by providing more accurate ICs in better details. Among these many DA methods, the cloud analysis is known for its ability to construct three dimensional cloud-related fields (e.g., hydrometeor contents, temperature, moisture) from sources of measurements with the application of physical models (e.g., parcel theory) and semi-empirical rules. Given its relative simplicity and low computational demand, the general cloud analysis procedure, with variety in actual realizations, has been widely implemented in many operational forecasting institutes around the world [e.g., NOAA

FSL's LAPS (Albers et al. 1996); UKMO's NIMROD (Golding 1998); NOAA's Rapid Refresh RUC (Benjamin et al. 2004)].

The ARPS complex cloud analysis, usually used in combination with the ARPS 3DVAR wind analysis, has shown its effectiveness in assimilating radar reflectivity data for improving short range forecasts of various types of weather systems (Hu et al. 2006a, b; Dawson and Xue 2006; Zhao and Xue 2009). Even though some positive impacts of the cloud analysis have been obtained in a number of case studies, particularly in the alleviation of the typical precipitation spin-up problem (Dawson and Xue 2006), its benefit is found to reduce promptly within the very first hour of the forecast in terms of a significant drop in the verification score (Xue et al. 2008). The limitation is greatly associated with the semi-empirical nature and assumptions involved, which can result in analysis of model state variables that is not necessarily consistent with the prediction model. Accordingly, the impact of the information introduced by the cloud analysis is mostly eliminated by a rapid self-adjustment during the initial stage of the forecast. Understanding the relative importance of the accuracy of various related state variables in the ICs can lead to an increased efficacy of cloud analysis and potential forecast improvements.

In the past decade, a certain amount of efforts have been made to investigate the relative importance of different state variables on the skill of convective scale storm predictions. By performing a series of sensitivity test, Weygandt et al. (1999) found the perturbation horizontal wind, among all fields they examined, having the largest impact on the evolution of a simulated convective storm. Forecast errors on a supercell storm simulation were examined, using 4DVAR, in terms of the response of the cost function

by Park and Droegemeier (2000). It was found for both in-storm and out-of-storm (i.e., environment) perturbation, the cost function has the greatest sensitivity to the temperature over either pressure or water vapor. In Weygandt et al. (2002a, 2002b), a study developing a single-Doppler parameter retrieval technique for a short-range prediction of a supercell thunderstorm, the strong dependence on the initial moisture fields for the predicted storm evolution was concluded. By alternately removing the perturbation in each of the initial fields, Sun (2005) tested the sensitivity of a supercell storm prediction and found its greater sensitivity to the wind, water vapor, and temperature (over the rain water and cloud water mixing ratio).

Inconsistency among the conclusions is found for the studies reviewed above. Due to the variation of the contexts (e.g., weather system chosen, approach applied, verification method) in these studies, their findings could be case dependent. As the main goal of this study is to investigate the limitation and the potential of the cloud analysis on assimilating the radar reflectivity data to improve the model predictions, we would like to "more unambiguously" examine the relative importance of these cloud-related model state variables. For this purpose, the Observing System Simulation Experiments (OSSEs) can serve as the best approach by providing an absolute truth simulation, and therefore the accuracy of both analysis and forecast can be assessed and verified quantitatively. A relevant OSSE study was conducted by Ge et al. (2013); however, in their study the impact of individual state variables was examined as potential observations, which are presumed comprehensively available over the entire domain and the intermittent 3DVAR analyses were applied.

In addition to the initial condition, another key factor that keeps the convective scale prediction challenging is the prediction model errors. Among the many possible deficiencies of the NWP model, the cloud microphysics parameterization scheme can pose significant forecast errors owing to the uncertainties involved. For example, the superiority of the microphysics schemes with more accurate and sophisticated treatments involved (i.e., the multi-moment schemes) are found to play a crucial role on providing more realistic storm structure and cold pool strength of the supercell thunderstorm simulation (Dawson 2009; Milbrandt and Yau 2006). The impact of the microphysics error on the storm prediction will also be evaluated in this study within our QSSE framework.

In the remainder of this chapter, the methodology of this study is first introduced along with the design of the OSSEs in section 3.2. In addition to the development of the truth simulation and the control experiment, a model-error-containing experiment set is conducted in section 3.3 to investigate the impact of the errors in model microphysics on storm prediction. In section 3.4, we then perform a set of model error-free experiments in which the relative importance of different individual model state variables is examined by direct insertion from the truth.

3.2 The Truth Simulation and the Degraded Control Experiment

The linear mesoscale convective system (MCS) taking place on the Central Great Plains at the beginning of 19 May 2013 is selected for conducting our study. Given with strong synoptic forcing including the low pressure center, associated front, dry line, and southerly moist air flow supplied by the Gulf of Mexico at the near surface level (Fig. 3.1) and the upper layer positive vorticity advection (not shown) that provide

favorable environment, the MCS first initiated at the leading edge of the low pressure center around the west border of Kansas and Nebraska, and then developed into a north-south oriented convective line across from North Dakota to Oklahoma as it propagated northeastward with time.

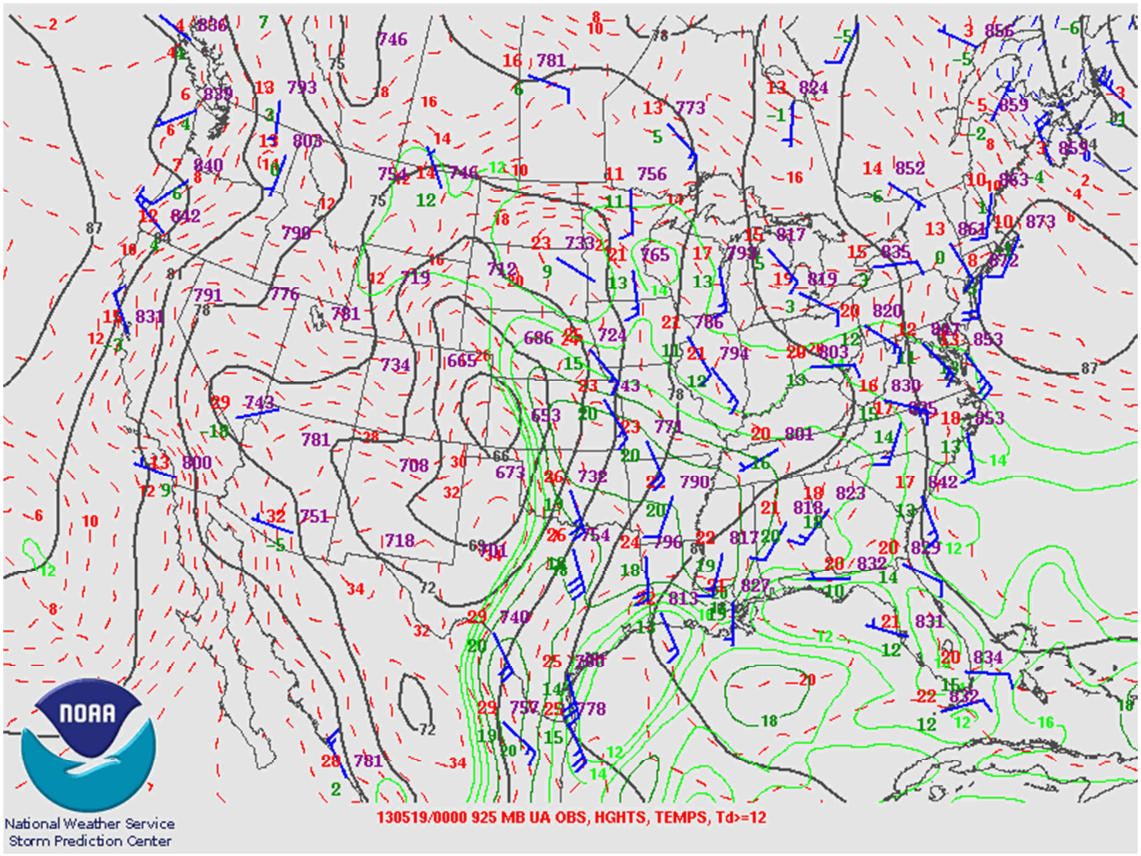

FIG. 3.1 Synoptic analysis at 925 mb valid at 00 UTC 19 May 2013. Geopotential height, temperature, and dew point temperature are provided with black solid contours, red dash contours, and green solid contours, respectively. Winds are provided in flags. Courtesy to the Storm Prediction Center of NOAA's National Weather Service.

3.2.1 The Model Configuration and Truth Simulation

From the collaborative Spring Experiment conducted by the Center for Analysis and Prediction of Storms (CAPS) and the NOAA Hazardous Weather Testbed (HWT), one of the ensemble members, arps_cn at 00 UTC of 19 May 2013, is acquired for the initial conditions (ICs) of our truth simulation. The analysis of arps_cn is generated by

applying procedures of both ARPS 3DVAR and cloud analysis to WSR-88D data and other available surface and upper air observations, and is available in 4-km grid spacing. A physical domain of our interest that covers most Kansas and Nebraska of 803 × 803 × 53 grids with 1-km horizontal resolution (FIG. 3.2) is then extracted from the arps_cn analysis. In vertical, the resolution is stretched with height from a minimum grid spacing of 50 m near the surface. The ARPS model is used to perform the forecast for our experiments.

All interpolated model state variables including three wind components u, v, w, pressure p, potential temperature θ, water vapor specific humidity q_v, mixing ratios of cloud water q_c, cloud ice q_i, rain water q_r, snow q_s, and hail q_h are adopted to serve as ICs, with which a six hour forecast is performed. The Milbrandt and Yau double-moment microphysics parameterization scheme (the MYDM scheme hereafter; Milbrandt and Yau 2005a, 2005b) with six hydrometeor species (cloud water, cloud ice, rain water, snow, graupel, and hail) is selected as its ability in giving microphysical features of storm closer to observation has been demonstrated in many present studies (e.g., Jung et al. 2010, 2012; Putnam et al. 2014). Besides, the 1.5-order turbulence kinetic energy (TKE) scheme, atmospheric radiation transfer scheme, and stability dependent surface scheme are included; however, the convective cumulus parameterization is omitted for the fine grid spacing used. For advection of model state variables, a fourth order scheme is applied in both horizontal and vertical direction for the momentum variables while a multi-dimensional version of flux-corrected transport (FCT) scheme is applied for scalar variables in better working with multi-moment microphysics scheme as recommended.

From the North American Mesoscale Forecast System (NAM), the three and six hour forecast fields of the 00 UTC run (same date) are interpolated from their original resolution of 12 km to our 1-km spacing domain for the lateral boundary condition (LBC) use at 03 and 06 UTC of our truth simulation. Note that six-hydrometeor-included MYDM scheme is used for the truth run while only five hydrometeor species are available in the IC. A spin-up period is therefore required for the model to reach its full complexity, at least in microphysics. Consequently, the first two-hour simulation is retained and excluded for analysis and verification, resulting in a four-hour studied period from 02 to 06 UTC. FIG. 3.3 is provided for a better understanding of the design of our experiment.

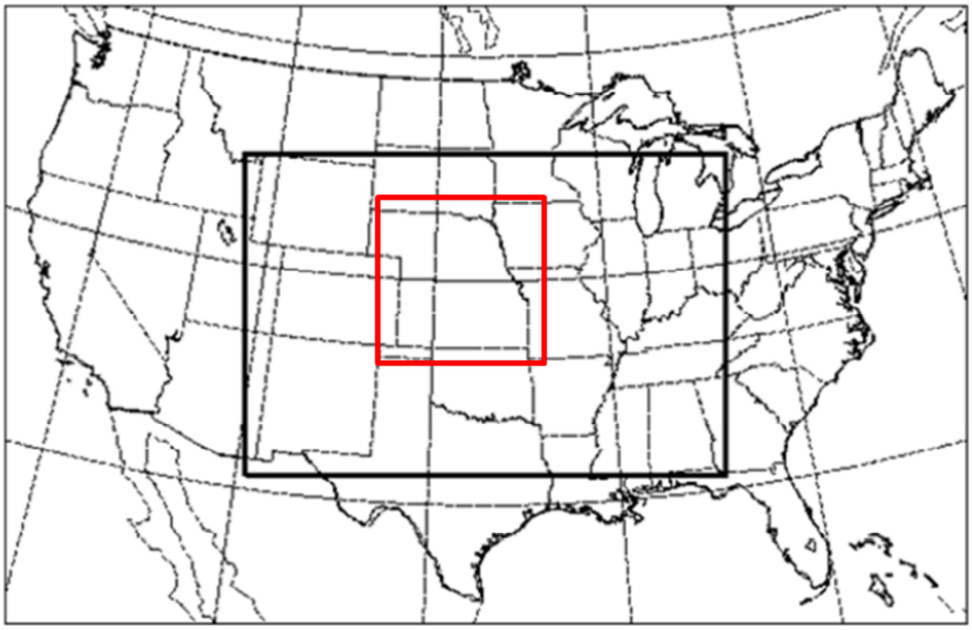

FIG. 3.2 Computational domains used for the experimental EnKF ensemble in 2013 Spring Experiment (600 × 400 grids with 4-km spacing denoted by black rectangle) and our study (803 × 803 grids with 1-km spacing denoted by red square).

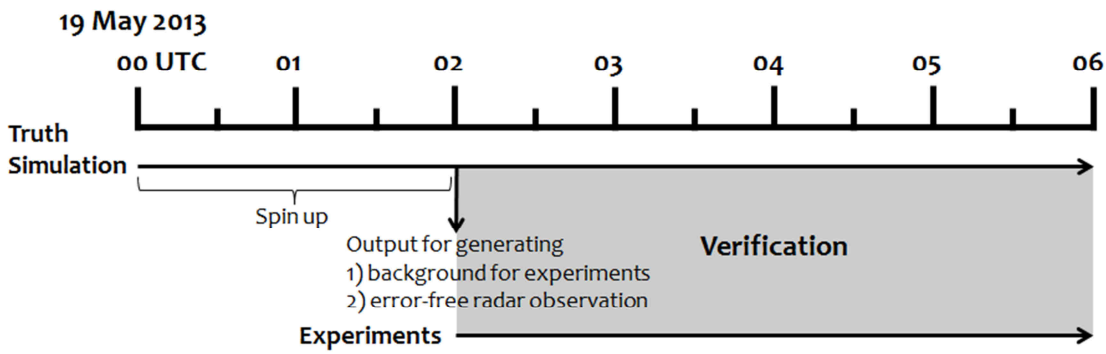

FIG. 3.3 Time line of the truth simulation and the experiments. Main studied period is marked by gray shading area.

The hourly simulated composite reflectivity of the truth simulation using the JZX operators is provided in FIG. 3.4, showing the MCS evolution during our studied period. The surface wind fields are also plotted in demonstrating the cyclonic flow and the associated low pressure center evolving along the west border of the states.

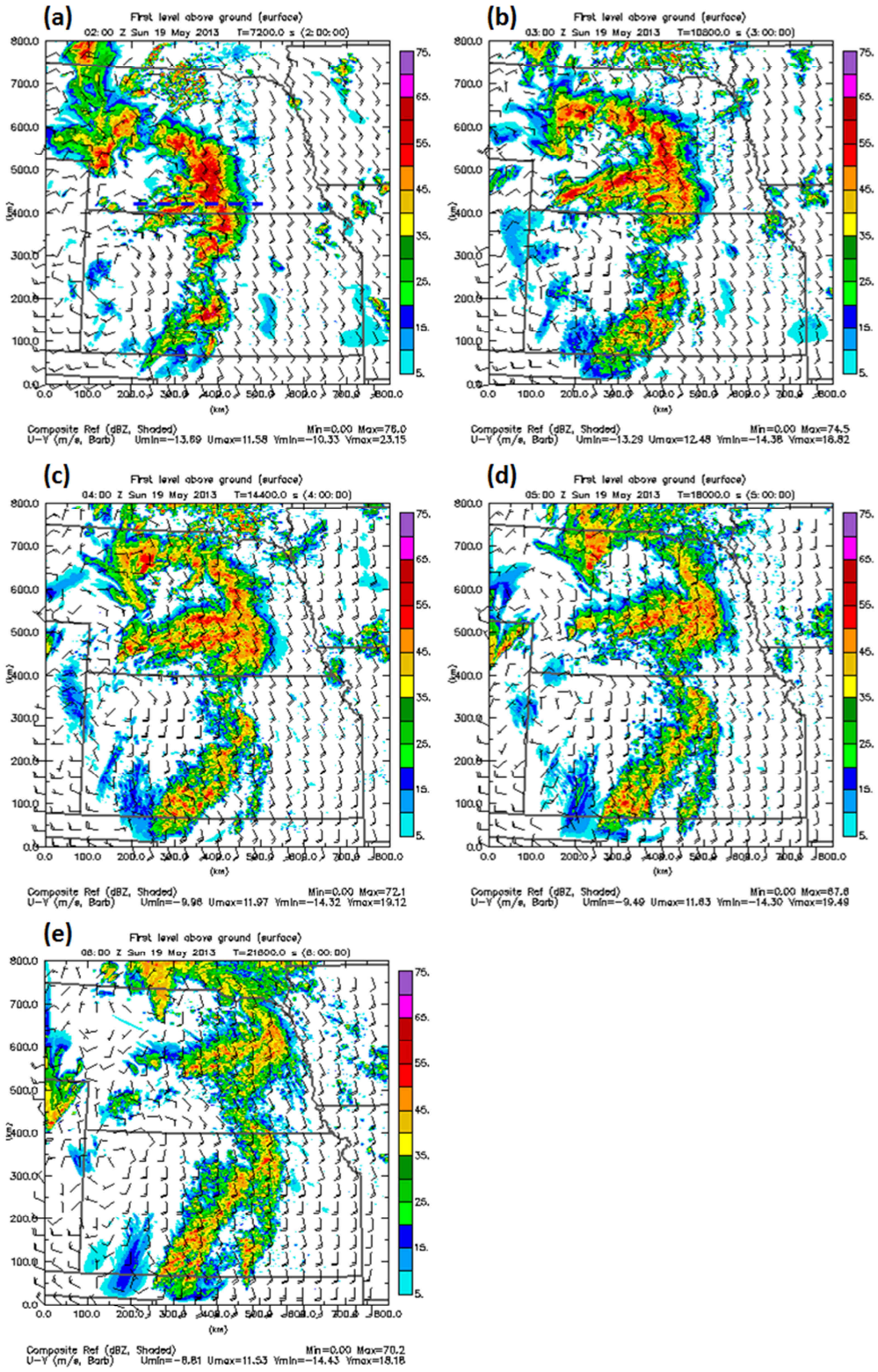

FIG. 3.4 Hourly simulated composite reflectivity (Z) and surface winds (V_h) of the truth simulation at (a) 02 UTC, (b) 03 UTC, (c) 04 UTC, (d) 05 UTC, and (e) 06 UTC. Wind flags are plotted in 40 km interval.

3.2.2 Degraded Control Experiment from Smoothed Initial Condition

After the truth simulation has been generated, we need to create a degraded IC upon which improvement is sought through various methods, including direct insertion of accurate state variables or by using the cloud analysis. The experiment starting from the degraded IC serves as a baseline, or control experiment (CNTL hereafter) for our sensitivity study. Considering that most ICs of regional NWP models do not contain detailed convective scale information, we create the degraded IC by applying three-dimensional smoothing to the 2-hour truth forecast fields at 02 UTC, and by setting the cloud and hydrometeor mixing ratios to zero throughout.

Model state variables u, v, w, θ, and q_v are smoothed horizontally on each model level by applying a running-mean average over a squared box of $2d$ width on each side. Therefore, the value at the center of the box is replaced by the average value of all grids within the box. As the point gets close to the boundary, reduced number of points is involved in the averaging. Given the method used, the wider is the averaging box, the stronger is the smoothing. After the horizontal smoothing is done, we then perform a three-layer averaging in the vertical direction.

Four experiments with varying degrees of smoothing in IC, SMT_d15, SMT_d35, SMT_d55, and SMT_d75, are first performed to find the most suitable candidates to use as CNTL. Different width of the smoothing box is used to achieve different degree of smoothing. In Table 3.1, four experiments and their smoothing configurations are listed along with simple statistics of the smoothed fields, and the truth simulation is also included as a reference. The statistics show that in general, the

extreme values are reduced as the smoothing degree increases (i.e., larger smoothing area applied).

Table 3.1 List of the truth simulation, four smoothing experiments, and their respective statistics

	Truth	**SMT_d15**	**SMT_d35**	**SMT_d55**	**SMT_d75**
Grid number in smoothing area	0	31 ×31	71 × 71	111 × 111	151 × 151
Smoothing area (km^2)	0	900	4900	12100	22500
Statistics, listed in form of maximum/minimum.					
***u* (m/s)**	24.1220/ -17.1698	19.0819/ -13.0527	18.3769/ -11.3160	18.1717/ -10.3630	17.8410/ -10.1474
***v* (m/s)**	32.5896/ -11.2516	28.4241/ -7.8982	27.0882/ -5.7812	26.3817/ -4.6936	25.7051/ -4.6351
***w* (m/s)**	12.1976/ -7.5282	1.2631/ -0.7680	0.6581/ -0.3714	0.5120/ -0.1873	0.4093/ -0.1511
***θ* (K)**	498.3150/ 297.4118	498.1960/ 297.5162	498.1078/ 297.5086	497.9968/ 297.5296	497.8345/ 297.5338
q_v (g/kg)	18.1776/ 0.0000	18.0348/ 0.0017	18.0575/ 0.0025	18.1092/ 0.0026	18.0936/ 0.0031

In FIG. 3.5, the perturbation potential temperature (θ') and wind fields at 6 km AGL at the IC time are shown for the truth simulation and for the four experiments after applying different degrees of smoothing. The 6 km AGL is shown because the MCS is found to initiate first around this level due to mesoscale convergence and the presence of warm unstable air. The positive θ' in the central part of this region is due to heating associated with the MCS in the truth simulation (FIG. 3.4a).

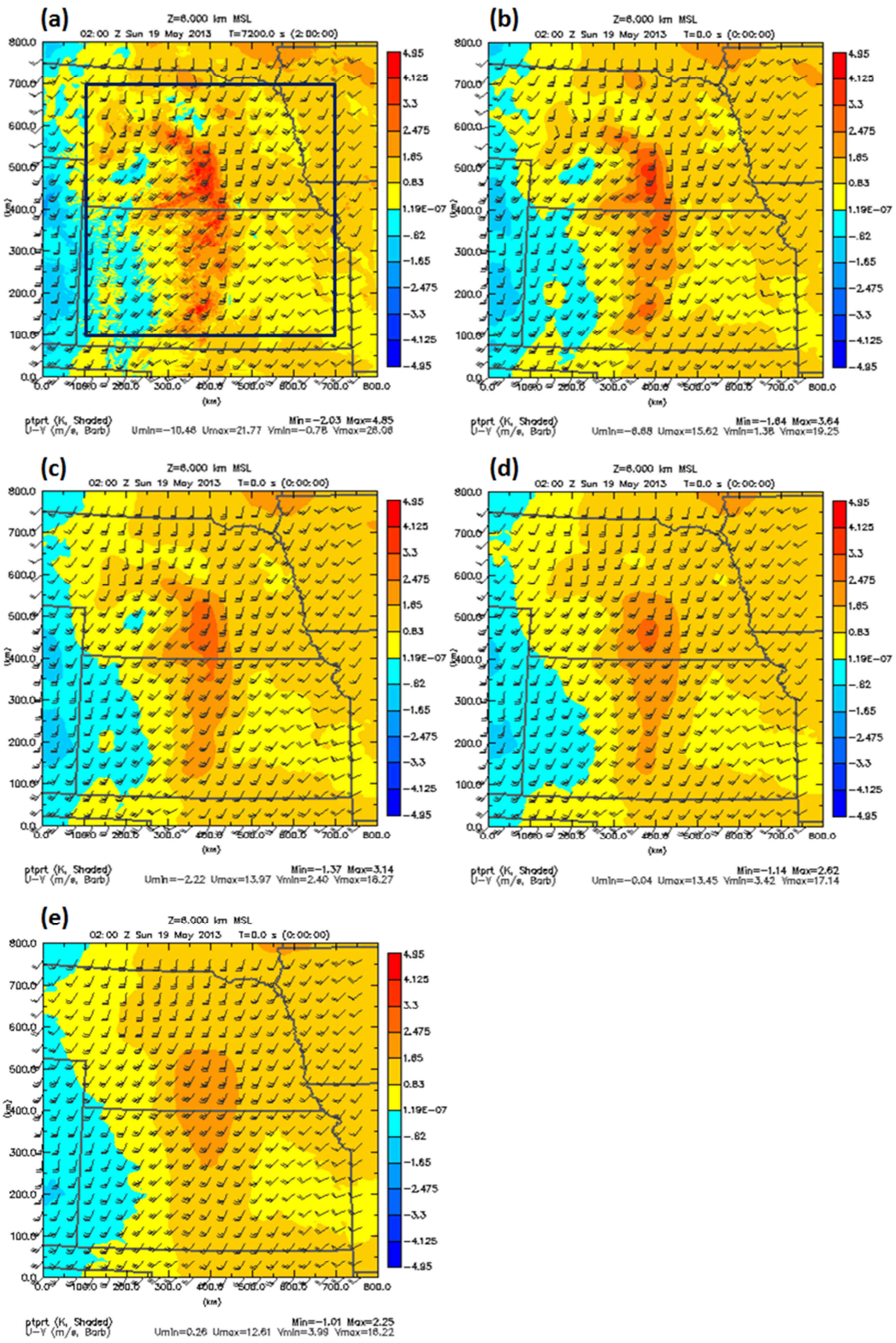

FIG. 3.5 Perturbation potential temperature (θ') and horizontal wind (V_h) field at 6 km AGL at 02 UTC for (a) the truth simulation, experiment (b) SMT_d15, (c) SMT_d35, (d) SMT_d55, and (e) SMT_d75. Wind flags are plotted in 40 km interval.

Throughout this study, scaled root mean square (SRMS) error is computed as a measure of the dissimilarity between the truth simulation and any experiment to be verified. Model state variables including wind components u, v, w, temperature T, specific humidity q_v, and total water mixing ratio q_w as the sum of all six hydrometeor species (i.e., $q_c + q_i + q_r + q_s + q_g + q_h$) are examined. The SRMS is equal to the regular RMS error scaled by the squared root of $\sigma_{\Delta X}^2$, which is the variance the initial condition error of X of the control experiment. The scaling non-dimensionalized the errors of different variables so that mean errors across different variables can be calculated. By simply averaging the SRMS results of all six variables listed above, we introduce a general measure of the overall forecast performance, the average SRMS (ASRMS) error. For detailed formulations of SRMS and ASRMS errors, refer to Appendix B.

FIG. 3.6a-e shows the SRMS errors of various model state variables and FIG. 3.6f shows the ASRMS errors of the forecasts of the four smoothing experiments. To reduce impacts from the lateral boundary, the verification is confined to an inner portion of the model domain that is 100 km away from the lateral boundaries (as denoted by the dark blue square in FIG. 3.5a), and excludes both top and bottom model layers in the vertical. Besides, the experiment with the strongest smoothing (i.e., SMT_d75) is used to provide the scaling factor for the errors shown in the figure. As we can see, for most variables including V_h, T, and q_v, the difference between the truth simulation and the experiments is proportional to their degree of smoothing. Generally, the smoother is the IC, the larger is the difference in the subsequent forecasts. This is expected since a smaller amount of smoothing will retain more fine-scale structures in the IC. However, there are some exceptions with w and q_w.

For *w* (FIG. 3.6b), the increasing dissimilarity with the degree of smoothing is only maintained during the first half an hour and partly near the end of the 4-hour forecast. Between 1 and 3 hours, the trend is mostly reversed, with the experiment with the least smoothing having the largest error in *w* forecast. This special behavior of *w* can be mainly attributed to the general nature of *w* field. Unlike other fields that commonly have gentle changes in spatial, the *w* field could have a rather localized abrupt increase or decrease due to isolated convective cores. For regions outside the convection, where *w* is relatively small (varying slightly around 0 m/s), the magnitude of *w* value can be significantly exceeded by the forecast error (i.e., difference from truth). When the updraft/downdraft in forecast has a displacement in its location from the truth, double penalty will occur, resulting in large RMS errors. In other words, the verification of the RMS error calculation of *w* is much more sensitive to small-scale displacement errors than other variables. Predicting *w* in wrong places will introduce double penalty. This is confirmed by looking at the errors of a *w* field with constant zero values everywhere – its SRMS errors calculated against the truth is actually the lowest after 1 hour, and decreases steady with time through the end of the 4 hour forecast (FIG. 3.4f). The fact that the *w* errors of SMT_d15 are the largest after half an hour and 2.5 hours of forecast suggests that smaller scale structures retained in the IC produce relatively large vertical velocities in the forecast that do not match exactly those in the truth simulation, leading to larger errors than in other experiments that have weaker vertical motion.

As for q_w (FIG. 3.6e), exactly the same initial SRMS_q_w is shared among all experiments as all hydrometeors were removed in the ICs. Within the first 1.5 hour of forecast, the expected relationship between IC smoothness and forecast error is

maintained. After that, irregular behavior of SRMS_q_w occurs as SMT_d35 shows the largest error from the truth. However, after 1.5 hours, the differences among the errors of the four experiments are relatively small. In spite of the exceptional behaviors with w and q_w, the overall forecast performance as measured by the ASRMS errors (FIG. 3.6f) still shows a clean relationship between the IC smoothness and the resulting forecast errors.

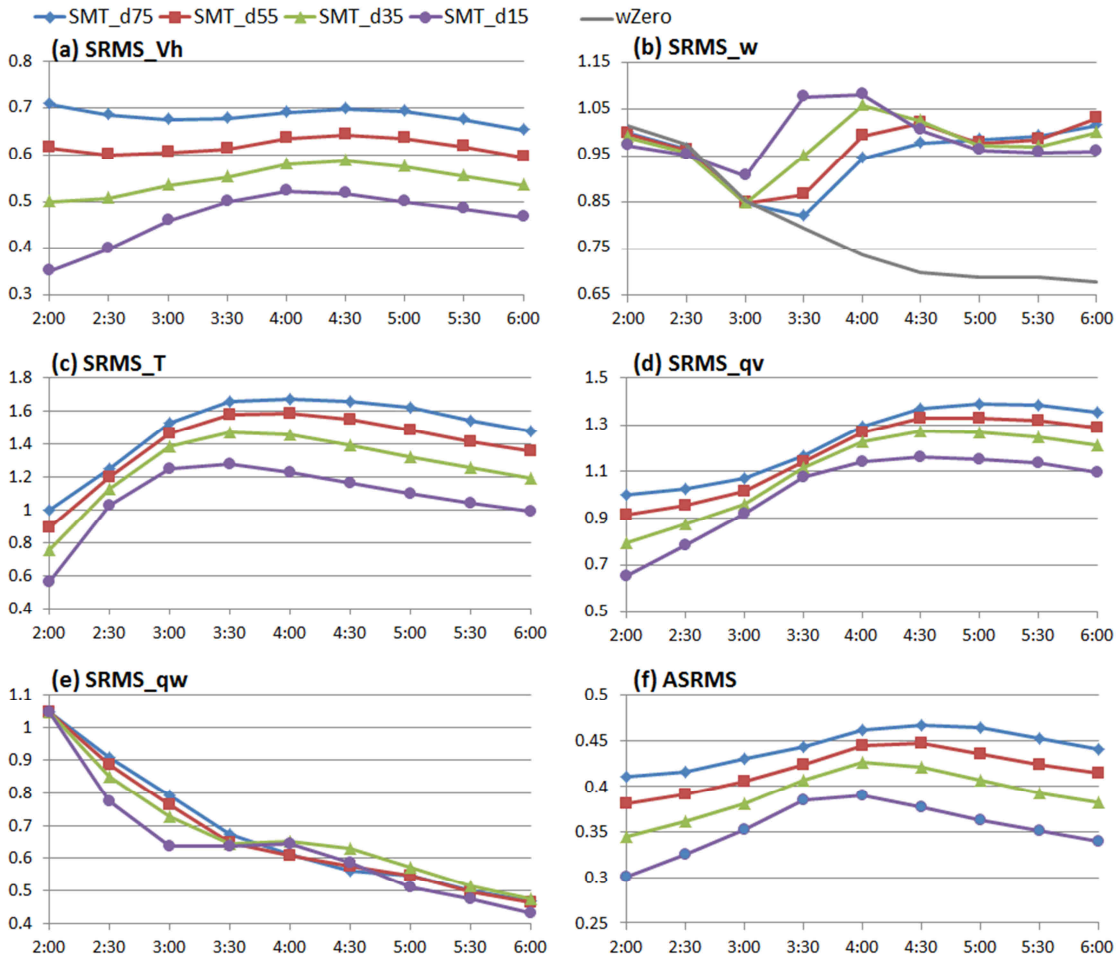

FIG. 3.6 SRMS error time series of (a) V_h, (b) w, (c) T, (d) q_v, (e) q_w, and (f) all variables for four smoothing experiments. The extra gray solid line in (b) is for a uniform 0 m s^{-1} w field.

The non-scaled RMS errors are also computed to examine the impact of initial smoothness on *Z* prediction (FIG. 3.7a). *Z* is examined in particular because it is an observed quantity and for real cases it is often used for forecast verification. Here, the JZX reflectivity operators are again used for simulating Z from the forecast state variables. Beginning with completely clear air, all four experiments share the same initial RMS error of *Z* (RMS_*Z*). As the forecast is carried on, the experiments with less smoothed IC begin to outperform by giving smaller RMS_*Z*. All four experiments share a decreasing trend of RMS_*Z* in general, owing to the gradual development of the MCS. Two other commonly used metrics, bias score and Equitable Threat Score (ETS), are also calculated for Z verification (provided as FIG. 3.7b and c, respectively). An arbitrary threshold of 30 dBZ that can be related to moderate precipitation is used. Similar to what has been seen in RMS_*Z*, a complete underforecast (i.e., bias score = 0) is obtained at beginning for the initial clear air field. An increasing trend is showing up as the storm gradually develops in the forecast. Among the experiments, the ones with less smoothed IC tend to be more efficient in storm development as their bias scores are getting closer to one (i.e., less underforecast) faster. Generally, ETS is also increasing with forecast time for all experiments, in which the one with least (most) smoothed IC gets the highest (lowest) score.

The MCS evolution of the experiments with the smallest (i.e., SMT_d15) and the largest degree (i.e., SMT_d75) of smoothing in IC are provided in FIG. 3.8 and FIG. 3.9, respectively, by which the verification results discussed above can be further illustrated. After comparing the four experiments with the truth simulation, it is found even with the largest degree of smoothing (i.e., SMT_d75), the storm can be rebuilt

within one hour of forecast as certain important mesoscale features have been kept in the smoothed initial condition (e.g., the warm core showing in FIG. 3.5e). The errors on the convective scale are much larger though in SMT_d75. Since the goal of our study is to examine the benefits of introducing convective scale information into the IC through various procedures, too good a baseline forecast is not desirable. For this reason, SMT_d75 is chosen to serve as the CNTL or baseline experiment.

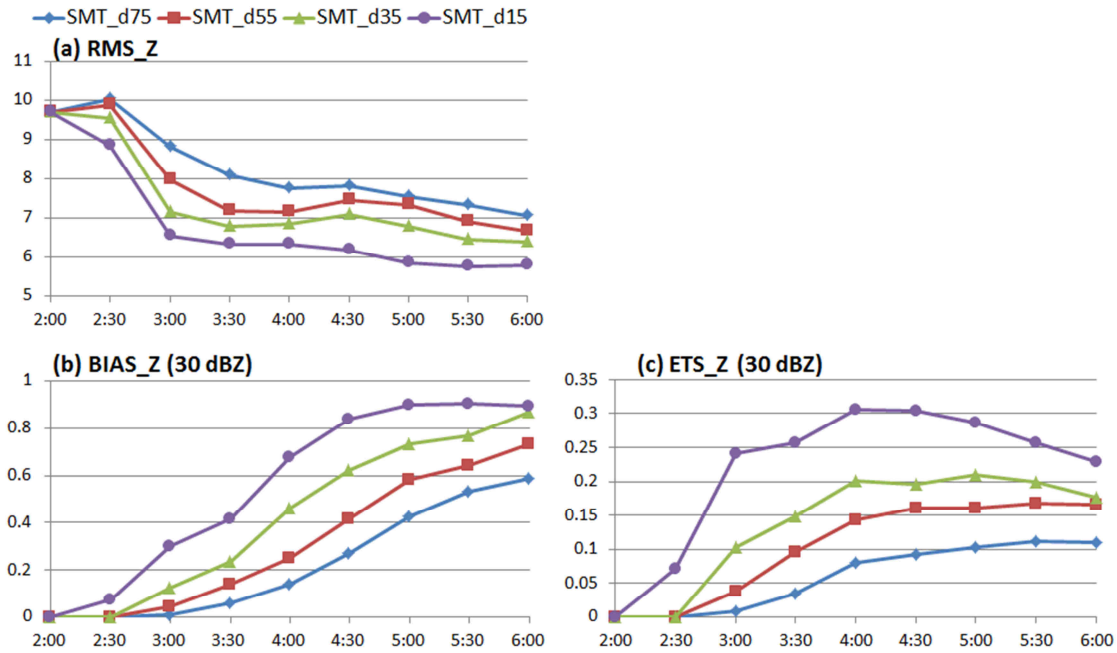

FIG. 3.7 (a) RMS_*Z*, (b) bias score, and (c) ETS calculated with threshold of 30 dBZ for four smoothing experiments.

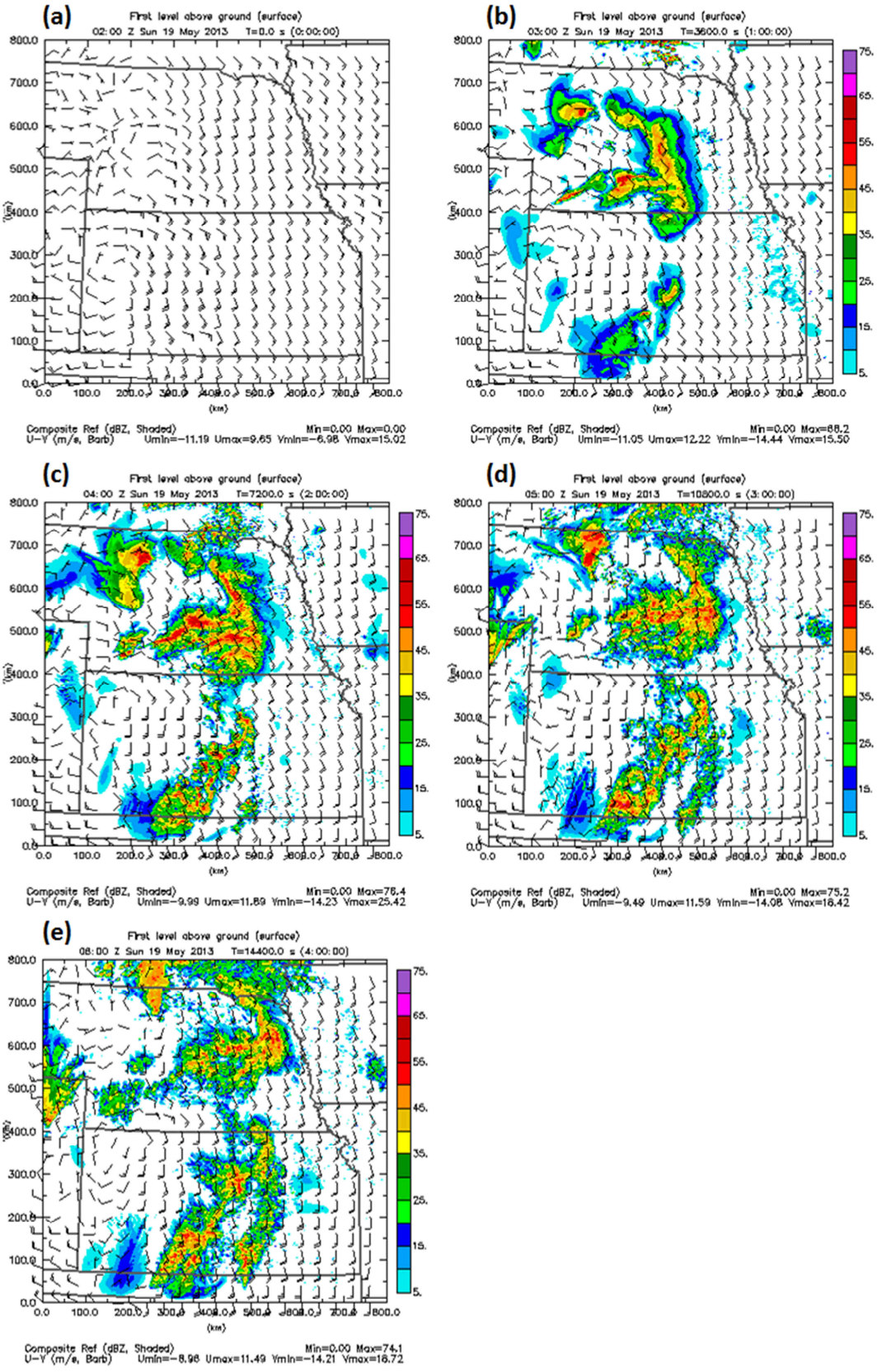

FIG. 3.8 Same as FIG.3.4, but for the experiment SMT_d15.

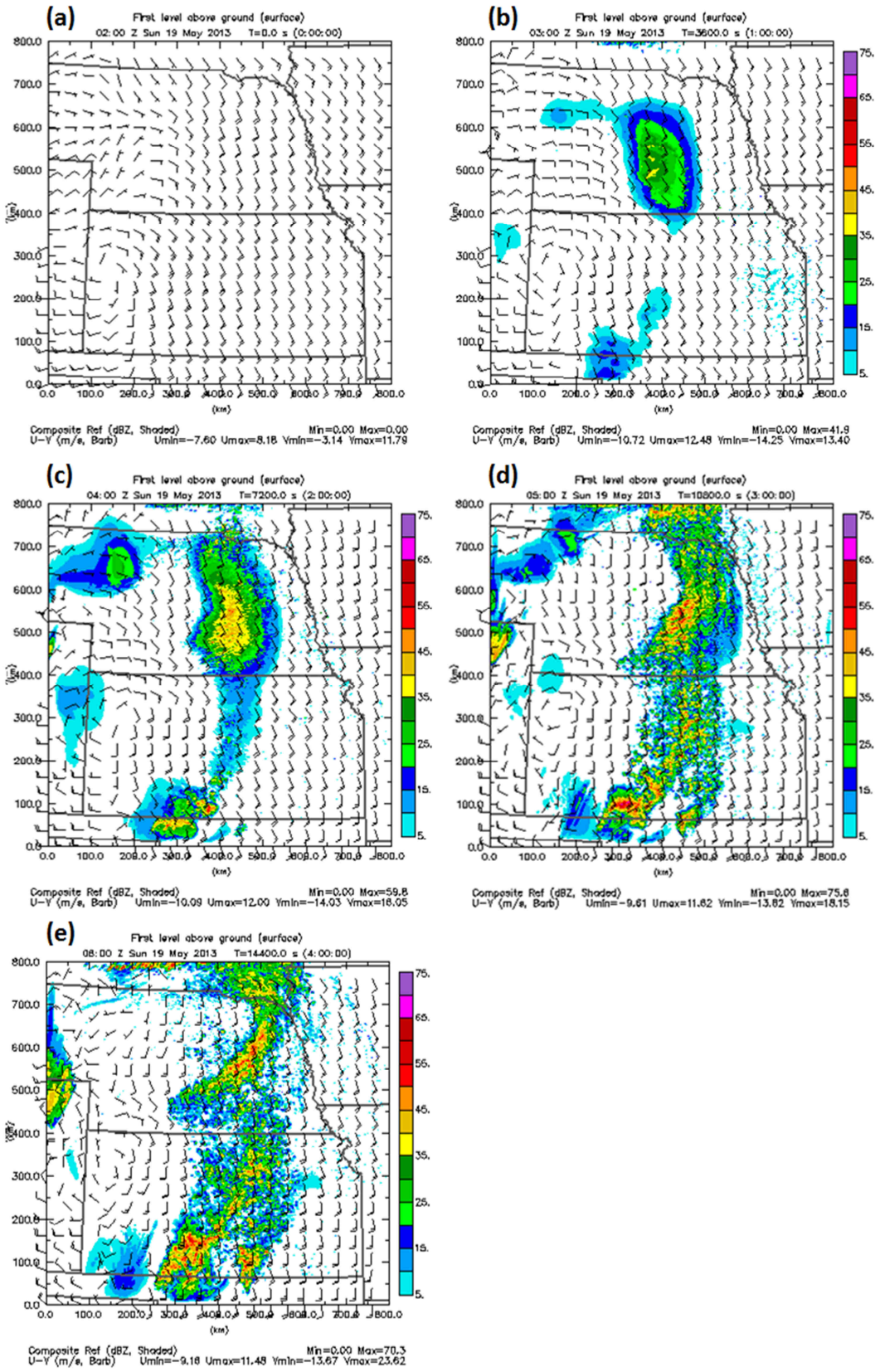

FIG. 3.9 Same as FIG. 3.4, but for the experiment SMT_d75.

In FIG. 3.10, the averaged scaled energy difference (ASED) of four smoothing experiments is shown. This index is calculated based on three energy differences (EDs): kinetic ED (KED, calculated upon u, v, and w), thermal ED (TED, calculated upon T), and latent ED (LED, calculated upon q_v), and used for evaluating the accuracy of the forecast results. These EDs of each experiment at every verification time are scaled by their own values at the initial time of the forecast before they are averaged into ASED. The scaling process results in ASED values of always unity at the initial time for all experiments verified. With both dynamic and thermodynamic structures are included in the verification, the ASED is ideal for the evaluation of the overall model forecast performance. In a word, the change of the ASED values along with forecast time within individual experiments represents the evolution of the forecast error relative to the initial error. Details about the formulation of ASED are provided in Appendix B. A similar trend of the forecast error are found for all four smoothing experiments (FIG. 3.10): the forecast errors are at first growing with time, reaching their peaks after 2 to 2.5 hour of the forecast, and then gradually decreasing in the later stage of forecast. It is found that experiments with larger degree of smoothing in IC result in larger error growths in terms of a relatively sharper increase in ASED (i.e., larger slopes) in the beginning stage of the forecast. This result is consistent with the ASRMS discussed earlier. According to these results, we conclude that the positive impact of the finer-scale environmental features retained in the ICs on the reduced forecast errors is not only significant but also systematic.

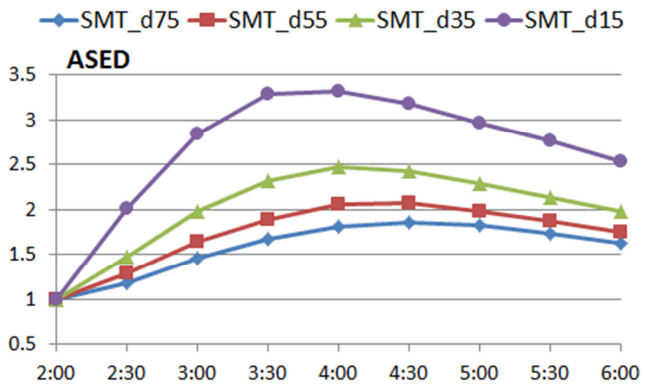

FIG. 3.10 ASED of four smoothing experiments.

3.3 Experiments with Model Error in Microphysics

Many sources can be responsible for the resulting forecast errors of NWP models. Other than the predictability limitation due to the nonlinear nature of the real atmosphere which has been demonstrated significantly sensitive to the ICs (Lorenz 1963), the prediction model itself can also introduce errors because of the deficiency in its design. Various cloud microphysics parameterization schemes (or shorten as microphysics schemes) have been developed for the NWP model use to characterize the hydrometeor-associated microphysical processes taking place in the spatial scale finer than the model-resolved grids. Given that the degree of sophistication varies among different microphysics treatments, the resulting forecasts can end with different accuracy. As the critical role of the microphysics schemes on predictions of the moist convection has been reported by many present studies (e.g., Dawson et al. 2010; Van Weverberg et al. 2011), a better understanding of the relative importance of the microphysics errors on storm prediction is favorable before we move forward to other model error-free experiments.

3.3.1 Design of Experiments

A set of experiments have been designed under our OSSE framework for us to examine the forecast accuracy resulting from the model error in microphysics schemes. In addition to the CNTL experiment as introduced in the previous section, three other experiments: MYDM, MYSM, and Lin, are performed. The main difference among these three experiments, as denoted by their names, is the microphysics scheme that has been implemented. Similar to the MYDM scheme introduced earlier, the MYSM is the acronym for the Milbrandt and Yau single-moment scheme. All six types of hydrometeor included in the MYDM scheme are also available in the MYSM scheme. Another experiment, with the application of a widely used single-moment ice microphysics scheme developed by Lin et al. (1983) with only five types of hydrometeor species (same as those in the MY schemes but with graupel excluded) is conducted as a contrast to the MYSM. Unlike the double-moment scheme that allows higher variability in drop size distribution (DSD) by predicting both mass content (q_x) and total number concentration (N_{tx}) of hydrometeors, the single-moment scheme only predicts the mass content with assumption of mostly fixed DSD parameters, resulting in limited microphysical complexity it can characterize.

All three microphysics experiments inherit most smoothed fields as used for the CNTL, except the hydrometeor variables from the truth simulation are remained in their ICs. To enable a full complexity that can be driven by respective microphysics scheme for storm prediction, both mixing ratios and the total number concentration are kept for the MYDM while the mixing ratios are kept for the other two single-moment experiments. For all experiments, the same JZX reflectivity operators are used for the

derivation of the simulated reflectivity, in which the DSD intercept parameter (N_0) is derived from the predicted N_t for the double-moment experiment while the fixed N_0 (default values) is used for the single-moment experiments. To compensate an expectable underestimation of the simulated reflectivity at the initial time for the Lin experiment owing to the lack of graupel species in its microphysics, the graupel is added into the hail category in the IC. Because the MYDM applies the same microphysics scheme to the truth simulation, it serves as the only model error-free experiment among the three microphysics experiments. We would like to note here the MYDM scheme is also used by the CNTL, but the hydrometeor fields are unavailable in its ICs. The configuration of the CNTL and three microphysics experiment is provided in Table 3.2 for a better perception. As a quick summary, at the initial time, all three microphysics experiments share the same error in most model state variables but retain perfect (i.e., error-free) hydrometeor information. Sensitivity of the model forecasts to different impacting factors, such as the microphysics error and the accuracy of hydrometeor and non-hydrometeor fields in ICs, is of our interests for exploration.

Table 3.2 Configurations of microphysics experiments

Experiments and microphysics scheme implemented	Number of hydrometeor type included	Initial fields of state variables u, v, w, θ, and q_v	Error-free hydrometeor information included in IC
CNTL[#]	6 (cloud water, cloud ice, rain, snow, graupel, and hail)	Smoothed	None
MYDM	6 (same as CNTL)	Smoothed	q_x and N_{tx}
MYSM	6 (same as CNTL)	Smoothed	q_x
Lin	5 (graupel unavailable)	Smoothed	q_x

is marked for CNTL to remark its application of MYDM.

3.3.2 Results and Discussion

In FIG. 3.11a-e, the SRMS errors of various model state variables are shown for the CNTL and three microphysics experiments. On the prediction of most variables including the horizontal winds, T, and q_v, the microphysics experiments with hydrometeor fields in the IC, regardless of the microphysics scheme used, generally outperform the CNTL in terms of the constantly smaller forecast errors throughout the entire four hours range. These outperformances of the microphysics experiments over the CNTL, in terms of the SRMS error difference, become even more significant in the later hours of the forecast. In fact, there is a slight exception found on the q_v prediction in the first hour of the forecast: the microphysics experiments have SRMS errors slightly larger than the CNTL. This exception suggests the great sensitivity of the model moisture prediction to the perfect initial hydrometeor fields introduced. It seems a certain degree of imbalance on prediction can be caused by the storm with convective scale structure, if provided with a supporting environment lacking the comparably fine features. Also, a much closer linkage of the hydrometeor fields to the moisture field than to other fields (e.g., winds or temperature) can be implied.

The same exception is also found on the w prediction in the first two hours of the forecast. However, the SRMS error difference between the CNTL and three microphysics experiments is much more significant compared to what is seen on the q_v prediction. A possible explanation for the larger error in the microphysics experiment is that the load put by the perfect hydrometeors in the IC generates extreme w values which do not match exactly with the truth given the degraded environmental features. As the forecast is carried on with time, the prediction of w given by the microphysics

experiments outperform that given by the CNTL in the last hour, indicating the benefit of the perfect initial hydrometeor fields finally overcomes the poor accuracy of other non-hydrometeor fields in the IC.

Given the perfect initial hydrometeor fields, the microphysics experiments show an absolute advantage over the CNTL on predicting q_w in terms of a zero initial error. However, the error difference decreases quickly after the forecasts are launched and becomes barely discernible after two hours.

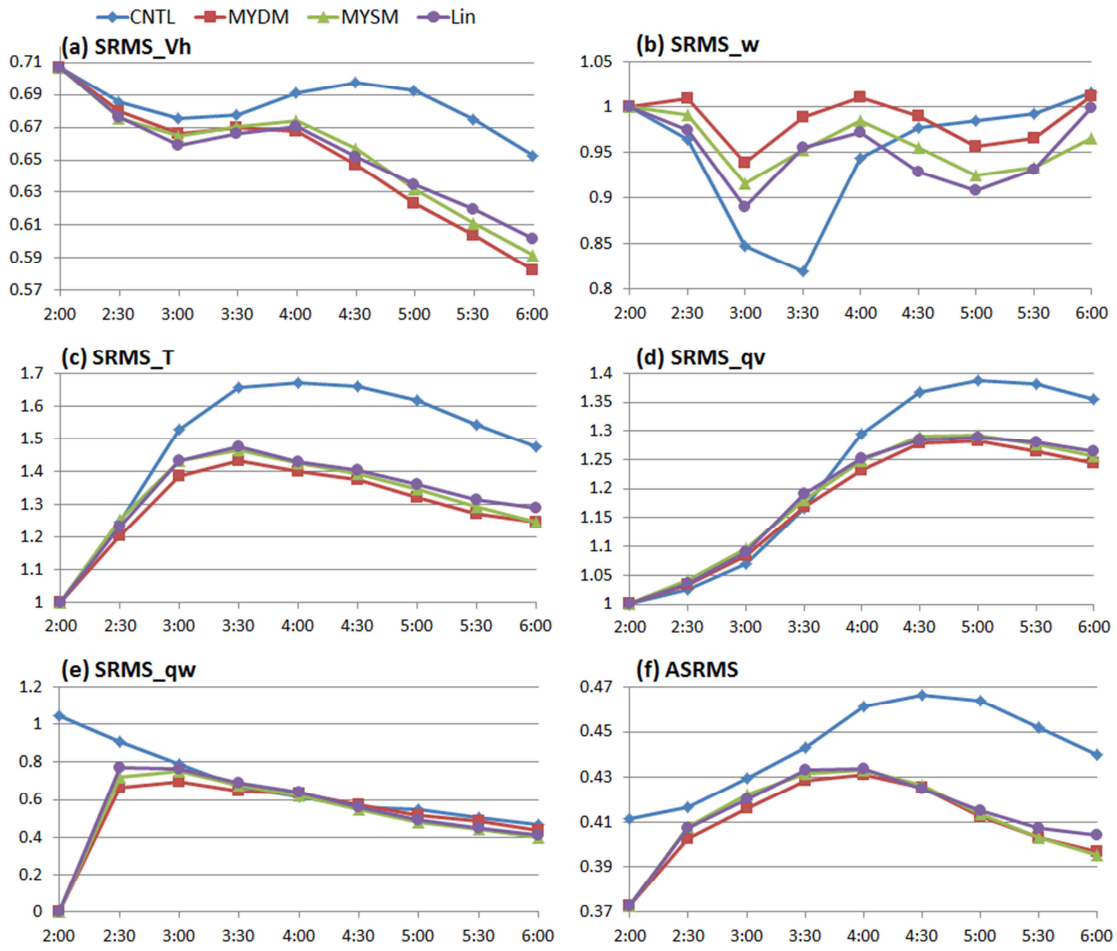

FIG. 3.11 Same as FIG. 3.6, but for the CNTL and three microphysics experiments.

While comparing the forecast performance among the three microphysics experiments, one may expect a systematic outperformance given by the MYDM since it is the only experiment with no microphysics errors involved (i.e., model error-free). However, it turns out the constant outperformance throughout the entire four hours range of the MYDM is only found on the predictions of T and q_v. On the prediction of V_h and q_w, the better performance of the MYDM over the other two microphysics error-containing experiments is found limited in the last two hours and the first one and a half hours, respectively. It can thus be conclude the forecasts of T and q_v, compared to forecasts of other state variables, have greater sensitivity to the microphysics error. The better q_w forecast performance of the MYDM over the other two single-moment experiments in the beginning stage can be attributed to the better details of the particle size distribution given by the extra predicted moment N_t. On the other hand, the forecast error difference between two single-moment experiments is relatively insignificant on most state variables, suggesting no one of them has substantial superiority to the other.

Overall, given by the ASRMS (FIG. 3.11f), the general forecast performance of the three microphysics experiments is significantly better than the CNTL throughout the four hours range of the forecast. This advantage (i.e., error difference) is initially provided by the introduction of the perfect hydrometeors in the ICs, and then maintained and continuously grown by the sequential outperformances of more accurate V_h, T, and q_v predictions. Among three microphysics experiments, the overall forecast given by the MYDM surpasses the other two single-moment experiments throughout mostly the four hours range, especially within the first two hours. However, even the MYDM, the microphysics error-free, experiences a significant forecast error growth due

to the errors in the initial non-hydrometeor fields, which is also believed to be the key impacting factor that limits the significance of the relative advantage of the MYDM to the other two single-moment experiments. No significant relative advantage is found between the MYSM and Lin, except for the last hour of the forecast in which the MYSM outperforms the Lin on predictions of most variables. Furthermore, in terms of the overall trend of the forecast error evolution, it is found the three microphysics experiments share a similarity on reaching their forecast error maxima around 4:00 UTC while the CNTL shows its peak a little later at 4:30 UTC, highlighting the different efficiency on constructing the structure of the storm and associated environment due to the availability of hydrometeors in the ICs. Same trend is shown in the ASED verification (FIG. 3.12): the model forecast error growth of the CNTL is steeper and lasts longer than that of the microphysics experiments. With the contrast between the CNTL and two single-moment experiments, it is concluded the perfect hydrometeors in the ICs, compared to the model microphysics error, play a relatively important role on giving more accurate predictions of the model state variables.

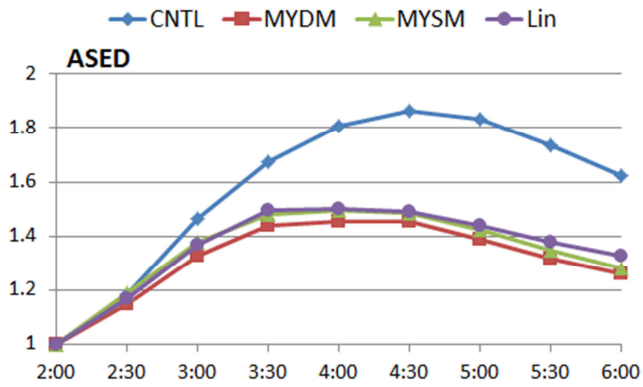

FIG. 3.12 Same as 3.10, but for the CNTL and three microphysics experiments.

The composite reflectivity and surface wind fields of the truth run, CNTL, and various microphysics experiments at the initial time (2:00 UTC) and two hours forecast range (4:00 UTC) are provided in FIG. 3.13 and FIG. 3.14, respectively. Note that instead of the entire domain used for the simulations, only the inner domain (as denoted by the blue square in FIG. 3.5a) on which the verification indices are calculated is focused and shown in the rest of our study. In FIG. 3.13 we see that even the same JZX reflectivity operators are applied on the same set of perfect hydrometeor fields at the initial time for all microphysics experiment, the intensity of the simulated Z shown for the MYDM is significantly higher than that of two other single-moment experiments, especially at the leading areas with the intense convective cores. On the contrary, the two single-moment experiments show relatively significant stratiform precipitation. These differences are mainly due to the different degree of freedom on microphysical process that can be characterized by the various microphysics schemes. Specifically, as the single-moment schemes only predict the hydrometeor mass content, their variability in DSD is reduced by the fixed intercept parameter (N_0) applied. On the contrary, extra variability of the MYDM is provided by the variable N_0, derived from the extra predictable moment N_t. More discussions about the variability of N_0 can be found in following sections and next chapter.

For the surface winds at the initial time, it is found most of the general features such as the cyclonic circulation associated with the low pressure center at the southwest corner of the domain are still kept in the smoothed fields for the microphysics experiments. However, certain features at smaller scale associated with localized storm developments are smoothed out. For example, there is a convergence line (as shown in

FIG. 3.13a) located behind the north tip of the convective line present in the truth simulation. Its occurrence can be attributed to the prevailing southerly winds and the northerly flows associated with the storm downward motions, which is localized but significant in its intensity. After the 3D smoothing, these storm-related flows are greatly weakened, and so is the associated convergence line (as shown in FIG. 3.13b-e). Unfortunately, small scale features like this usually play a critical role on storm evolution and large errors can be caused on the subsequent forecasts as a result. As a demonstration in our case, in the truth simulation, right at the location of the convergence line there is a convective line initiating in the later hours (as shown in FIG. 3.14a). On the contrary, the formation of this convective line, however, is not seen in other experiments with smoothed ICs. Even with the perfect initial hydrometeor fields and perfect model microphysics as provided in the MYDM (FIG. 3.14d), the convective line is still not able being regenerated for the lack of the required kinetic feature.

A qualitative idea about the impact of different microphysics schemes on storm prediction is given by FIG. 3.14, the two hours forecast of the reflectivity. Generally, similar storm distribution is shown among all three microphysics experiments. The major difference is seen in the intensity of the forecast convection: the MYDM tends to give storm prediction with more dominant intense convection, which is most close to the truth simulation, while the MYSM tends to generate more stratiform precipitation with less organized convective cores embedded within. The Lin, compared to the two MY schemes, is an intermediate case. On the whole, none of the single-moment experiments is able to provide storm prediction with intensity comparable to the truth. Underforecast in the storm intensity is also found for the MYDM, but it is relatively

small. As the key driver of the storm movement/propagation played by the horizontal wind fields has been reported in existing studies, the small sensitivity of the horizontal wind forecast to the microphysics scheme used can be implied by the similar predicted storm location/distribution among different microphysics experiments shown in FIG. 3.14c-e. This implication is also consistent with our earlier SRMS error verification.

Even with no hydrometers at the initial condition time, the CNTL can build up the storm with intensity comparable to the truth in a considerable efficiency (within two hours, specifically, as shown by FIG. 3.14) through the use of the perfect microphysics treatment. The advantageous application of the error-free model microphysics (i.e., the MYDM) on spinning up the moist storm from a dry IC will be further demonstrated by the quantitative verification of reflectivity later.

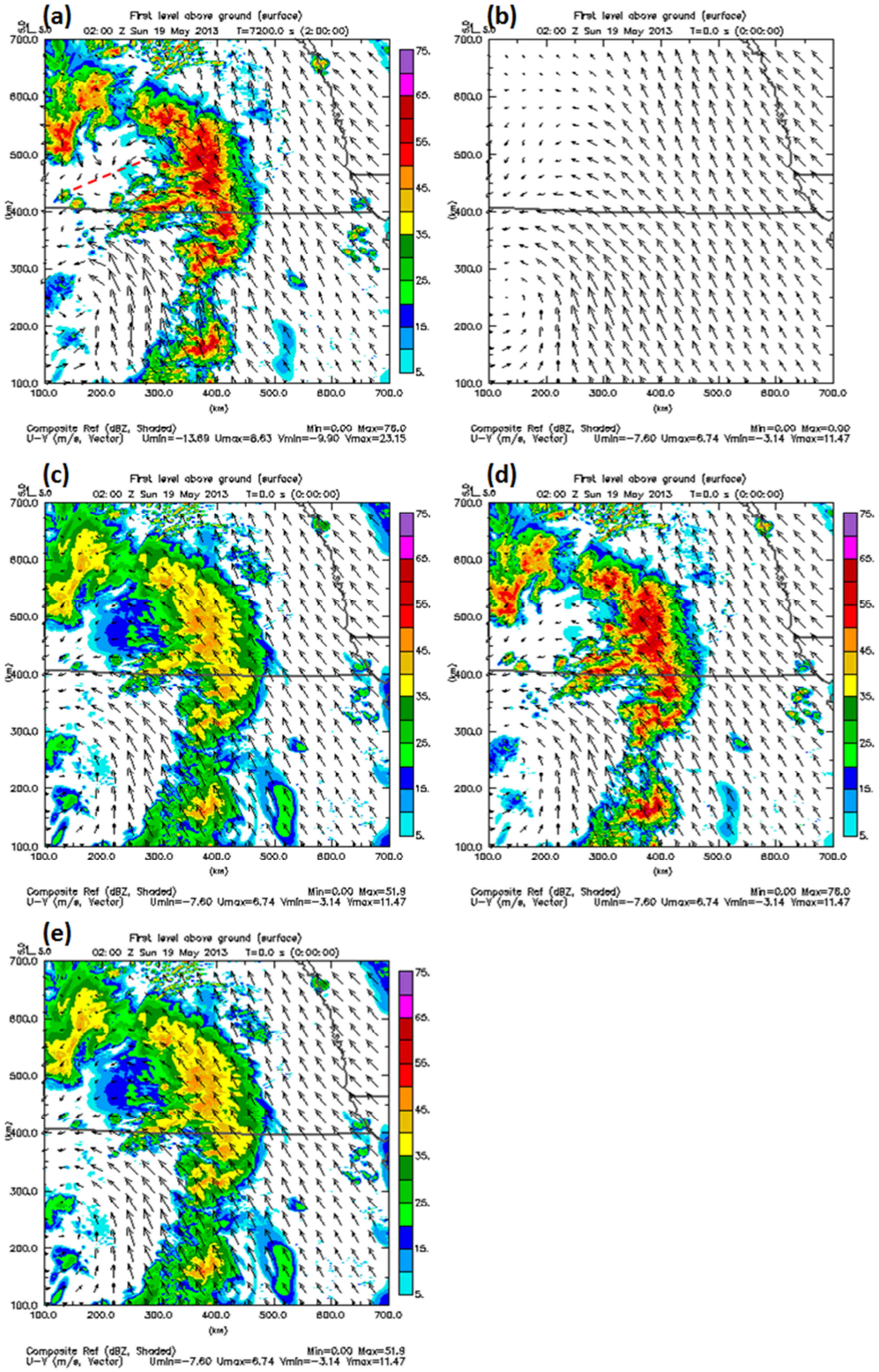

FIG. 3.13 Composite reflectivity and surface winds at 02 UTC for (a) truth simulation, (b) CNTL, (c) MYSM, (d) MYDM, and (e) Lin. The convergent line is indicated by a red dash line in (a). Wind arrows are plotted in 30 km interval.

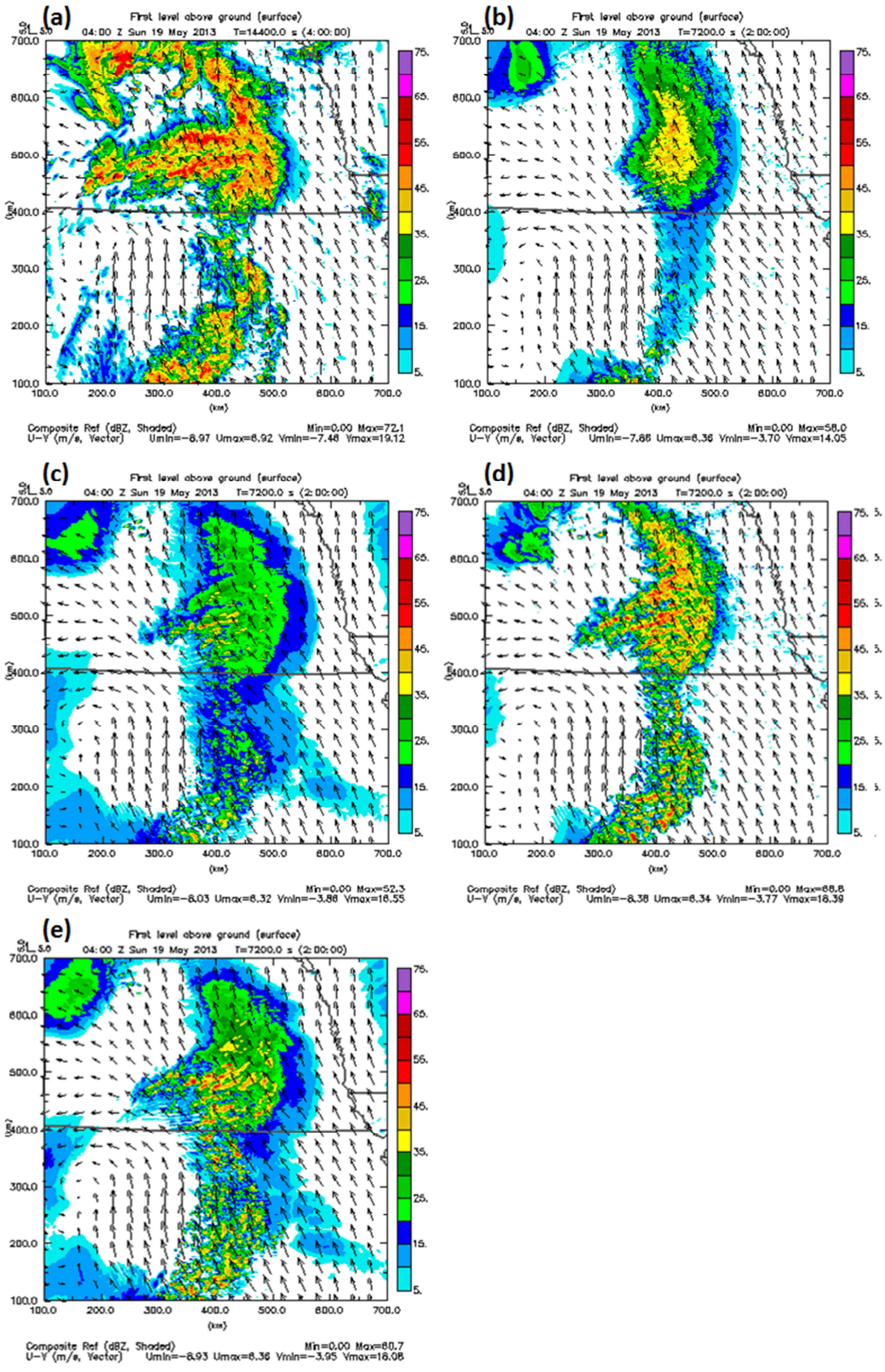

FIG. 3.14 Same as FIG. 3.13, but for 04 UTC.

FIG. 3.15, the verification of simulated reflectivity, provides qualitative insight into the overall performance of the storm prediction given by the CNTL and three microphysics experiments. In terms of the general similarity, given by the RMS error, between each experiment and the truth simulation, the MYDM is found to be the only one that keeps performance better than the CNTL over the entire four hours range. On the contrary, the other two single-moment experiments both have their performance surpassed by the CNTL at 3:30 UTC and beyond. Similar result is also seen in the ETS verification that evaluates the experiment performance on predicting storms with moderate intensity (here, 30 dBZ and above). Indicated by the result, even with the benefit of the perfect hydrometeor fields in ICs, the outperformance of the single-moment experiments over the CNTL can only last for one hour in presence of the microphysics errors. The difference between these reflectivity verification results and those of the model state variables discussed earlier implies a greater impact of the microphysics error on the Z prediction than on the other model state variables. On the comparison between the two single-moment experiments, although the MYSM is found to outperform the Lin with Z prediction generally closer to the truth (in terms of smaller RMS errors, provided in FIG. 3.15a) at most times throughout the four hours range (with only one slight exception at 3:30 UTC), its tendency of producing fast-dissipating storms, as illustrated by FIG. 3.14c with relatively weak stratiform precipitation as well as demonstrated by the significantly low bias scores (FIG. 3.15b), makes it no better than the Lin after 3:30 UTC on predicting intense convection (also demonstrated by FIG. 3.15c).

Because the hydrometeor mixing ratios are the main input to calculate the simulated reflectivity, one may expect similar results with the q_w and Z verifications among the experiments using different microphysics schemes. However, we find that noticeable differences in q_w prediction among different experiments is limited to the very first hour of forecast, while MYDM outperforms other microphysics schemes in terms of Z throughout the 4 hours of forecast and the differences are quite significant. The seemingly inconsistency can be explained by the fact that Z depends on many more variables than q_w. For one thing, q_w is a simple sum of all hydrometeor mixing ratios; it is therefore not sensitive to the distribution of water and ice among the individual species while the actual species with the existence of ice and water mass matters to the Z calculation. In addition, Z is also a function of the intercept parameters N_{0x} for each of the species, which are assumed fixed values in single moment schemes but derived from predicted total number concentrations N_{tx} in the case of a double moment scheme. Therefore, compared to the q_w, Z is much more sensitive to the details of the hydrometeor species, including their mass distribution among the species and their particle size distributions. As a result, Z difference provides a more stringent measure of the differences among experiments. For these reasons, the better performance of MYDM in the later forecast was not seen in terms of q_w but could still be seen in Z, indicating better prediction of microphysics details in MYDM.

One thing we would like to point out here that in FIG. 3.15c, the ETS of the MYDM is able to remain above the CNTL as long as four hours. Given the key difference between the CNTL and MYDM, the advantaged performance of the MYDM, therefore, suggests potential improvements on the storm predictions can be theoretically

achieved by the accurate hydrometeors in the ICs. However, this length of advantage is rarely found in the practical experience of real case simulation, which could be attributed to the limitations of 1) the analysis error in initial hydrometeor fields, and 2) the imperfectness of the microphysics schemes.

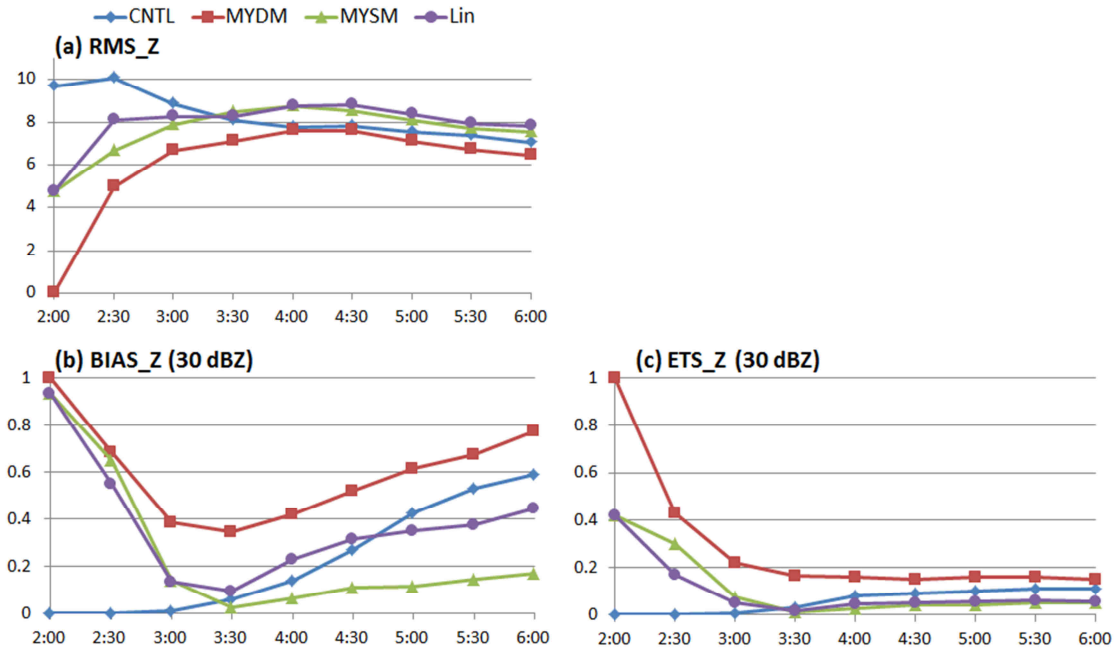

FIG. 3.15 Same as FIG. 3.7, but for the CNTL and three microphysics experiments.

3.3.3 Summary

Impact of model errors due to the incorporated microphysics schemes on storm prediction has been investigated. The MYDM serves as the model error-free experiment as the same scheme is used for carrying out the truth simulation. Two other single-moment microphysics schemes with different degrees of complexity, the Lin and MYSM, are also tested. Compared to the CNTL that incorporates perfect microphysics but hydrometeor-free ICs, three microphysics experiments are initialized with perfect

hydrometeor fields. The relative importance between the availability of initial hydrometeors and the model microphysics accuracy is examined.

Among the individual model state variables we examined, the advantage of perfect microphysics (i.e., MYDM) over two other single-moment schemes in providing constantly better forecast throughout the entire four hours verification period is found on prediction of T and q_v. Overall, no significant advantage is found given by either the MYSM or the Lin. Positive impact of perfect microphysics on predicting q_w is limited in a very short forecast range (about 1.5 hour) as the evaluation of hydrometeor number concentration is not included in this verification. Model microphysics accuracy appears to have relatively small impact on predicting kinetic fields (i.e., V_h and w) according to the irregular forecast error behavior found among the experiments. In general, the impact of the microphysics errors is relatively insignificant compared to the initial errors. In spite of the microphysics scheme selected, even with perfect initial hydrometeor fields, large forecast error of model state variables grows quickly within the first two hours of the forecast. The significant error growth is most likely owing to the IC uncertainty introduced by the smoothed non-hydrometeor fields. In contrast to the microphysics error, the impact of the perfect initial hydrometeor fields is significant. Systematically better forecast of most state variables over the CNTL is ensured by the perfect initial hydrometeor information equipped in the microphysics experiments. In other words, the deficiency of model microphysics schemes could possibly be expected compensated through an accurate hydrometeor initialization.

A much more crucial impact of the microphysics errors is found on prediction of reflectivity, in which greater sensitivity to the microphysics details is granted. While all

experiments suffer the inaccuracy of the non-hydrometeor fields, due to the smoothing, at the initial condition time, the MYDM is found to provide the systematically best forecast with the least under-forecasted Z intensity. Two other single-moment microphysics experiments, compared to the MYDM, tend to predict too much stratiform precipitation and fail to maintain desirable convection intensity. Even launched from a completely clear air (i.e., CNTL), forecast with decent storm intensity can be achieved efficiently within two hours (i.e., spin-up time) by the use of the perfect microphysics scheme. Furthermore, after this spin-up time required, the CNTL is able to outperform two single-moment microphysics experiments that have perfect initial hydrometeor fields, again highlighting the importance of the microphysics errors on storm prediction.

3.4 Experiments with Direct Insertion of State Variables

Beginning at this point, the model microphysics errors are completely excluded in our following experiments by applying the MYDM scheme as implemented in the truth simulation. By ensuring a perfect model, the impacts purely due to the IC uncertainty can be distinguished. As more and more efforts have been made in the field of data assimilation toward the goal of improving the ICs for improved model forecasts, a deeper investigation of the relative impact of IC accuracy on storm prediction is valued and useful.

Before we explore further to the impact directly given by the cloud analysis process, we would like to first examine the impact of different individual state variables, particularly those are taken care of in the cloud analysis, by alternately inserting their perfect values from the truth simulation back to the ICs. Through this set of experiments,

the relative importance of these cloud-related state variables will be revealed and further discussed.

3.4.1 Design of Experiments

In our OSSE framework, five experiments: Pt, Qv, Qcld, Qpcp, and Qall, are performed in addition to the CNTL in examining the sensitivity of model prediction to the accuracy of five respective sets of state variables: 1) θ, 2) q_v, 3) cloud hydrometeors (q_{cld}, including cloud water and cloud ice), 4) precipitation hydrometeors (q_{pcp}, including rain, snow, graupel, and hail), and 5) all hydrometeors (i.e., $q_{cld} + q_{pcp}$) in the IC. Again, most smoothed fields are directly inherited from the CNTL for all experiments; however, for each experiment, one set of specified variable, as denoted by the experiment name, from the truth simulation is directly inserted back into the ICs. For example, the experiment Pt has the error-containing wind and q_v fields, cleared hydrometeor fields, but the error-free θ field. For three hydrometeor experiments Qcld, Qpcp, and Qall, both mixing ratio and total number concentration are included in the perfect insertion for the application of the MYDM scheme in our simulation. Table 3.3 is provided in the form of a checklist, with which the configuration of each experiment is shown. We would like to point out that the experiment Qall here is in fact, identical to the experiment MYDM in the previous section.

Table 3.3 Configurations of direct insertion experiments

Experiments	Perfect (non-smoothed) wind field	Perfect (non-smoothed) θ field	Perfect (non-smoothed) q_v field	Perfect (un-removed) cloud hydrometeors	Perfect (un-removed) precipitation hydrometeors
CNTL	x	x	x	x	x
Pt	x	V	x	x	x
Qv	x	x	V	x	x
Qcld	x	x	x	V	x
Qpcp	x	x	x	x	V
Qall	x	x	x	V	V

3.4.2 Results and Discussion

Again, for each experiment, a four hours range of forecast is performed and the results are ouput every 30 minutes for quantitative verifications. The SRMS errors on predictions of various model state variables are shown in FIG. 3.16.

On the prediction of horizontal winds (FIG. 3.16a), most of the experiments are able to provide forecasts better than the CNTL throughout the four hours range. However, there is one notable exception occurring to experiment Qv in the first hour. This slightly larger prediction error could be attributed to the nonlinear interactions between the perfect q_v field and other error-containing fields. Also, the relatively efficient impact of the initial q_v accuracy on horizontal wind prediction is suggested. In spite of the larger dissimilarity from the truth in the first hour of the forecast, the Qv shows an abrupt decrease of the prediction error and significantly outperforms all other experiments beginning at 4:00 UTC. Based on this finding, we further conclude the significant impact of the perfect initial q_v on horizontal wind prediction is not only instant but also systematic with the forecast range. In contrast to the Qv, the Pt firstly shows an overwhelmingly best performance within the first one and a half hours, but experiences a sudden increase in the prediction error after then. Besides the Qv, the Qall

is found to give the second best performance on V_h prediction in terms of better forecasts in longer ranges.

A similar trend of forecast error is found on *w* prediction (FIG. 3.16b): a significantly large error growth in the first 1.5 hours is given by the Qv, but the error then decreases to the smallest in the later stage of the forecast. Unlike most of the experiments maintaining forecast errors in a little variation in the last hour of the forecast, the Pt shows a dramatic peaking-up of the *w* error, resulting in a performance seriously worse than that of the CNTL. The very-short-range negative impact of introducing finer resolved environmental features on *w* prediction, as discussed earlier in the experiment with different degree of IC smoothing provided in section 3.2, is again presented by the contrast of the performances between the CNTL and the perfect state variable insertion experiments in the first two hours of the forecast.

On the prediction of *T* (FIG. 3.16c), it is found generally, all experiments result in giving forecasts better than the CNTL throughout the entire four hours range. An exception is found given by the Pt with an unusual significant error growth in the last 30 minutes of the forecast, resulting in a forecast performance even slightly worse than that of the CNTL in the end. On the contrary, no other experiment, even beginning with the imperfect initial *T* field, is found to have this later stage error growth on *T* prediction. Among all perfect state variable insertion experiments, the Qv and Qall perform competitively best in the first 1.5 hours, but after then the Qall is significantly surpassed by the Qv. On the other hand, no significant forecast error difference is found among the Pt, Qcld, and Qpcp until the Pt shows the sudden worsen performance at last. It is

worth noting that the perfect initial θ field does not necessarily end with the best temperature prediction, but actually the worst.

A great sensitivity of the q_v prediction to the introduction of any of the perfect state variables at the initial time is suggested by their relatively larger forecast error compared to the CNTL within the first one and a half hours range (FIG. 3.16d). A quick forecast error growth is again found for the Qv, resulting in a largest forecast error among all experiments at 3:00 UTC even though it begins with the prefect initial q_v field. Afterward, the forecast error of Qv holds nearly constant with time and eventually becomes the smallest when all other experiments experience significant error growth. Other than the Qv, the Pt also shows a relatively significant instant error growth in the first hour of the forecast and ends with the second best performance. On the other hand, the Qall is able to keep a fairly good performance lasting as long as two hours before getting significantly surpassed by the Pt.

Among the three experiments with no hydrometeors in the ICs (i.e., CNTL, Pt, and Qv), the Qv exhibits the largest storm-rebuilding efficiency in terms of a significantly reduced q_w prediction error in the first hour of the forecast (FIG. 3.16e). Regardless of the various magnitudes of the total water mixing ratio error at the initial time owing to the different degree of the hydrometeor completeness, all experiments have their errors converged, with the hydrometeor-equipped experiments (i.e., Qcld, Qpcp, and Qall) increase their errors and the hydrometeor-free experiments (i.e., CNTL, Pt, and Qv) decrease their errors, after one hour of the forecast. A noticeable larger error is found given by the Qv between 3:30 and 5:00 UTC, which could be possibly related to the significant error on the w prediction present beforehand since the close linkage

between the vertical motion and hydrometeor loading has been discussed in the previous section.

Finally, the general performance of each experiment on predicting model state variables can be represented by the ASRMS error shown in FIG. 3.16f. Overall, experiments with direct insertion of perfect q_{cld}, q_{pcp}, or q_{all} could provide forecasts constantly better than the CNTL. Other than that, the Qv experiences an instant forecast error increase, mainly from the winds and q_v predictions, making its performance worse than the CNTL in the first hour. However, after the first hour, the error of Qv rapidly decreases and becomes the lowest among all experiments beginning at 4:00 UTC. The Pt is found to perform competitively with the Qcld and Qpcp for most of the times before it experiences an abrupt error increase resulting from the w and T predictions in the last hour. The impact of the unique significant error growth in the later stage of the forecast caused by the perfect initial temperature field calls for deeper investigation on the interaction among individual state variables before we can determine whether it is universal-existing or case-dependent. As a conclusion, the accurate initial q_v is found to have the largest impact on giving better predictions of state variables, while a complete set of initial hydrometeor fields is secondarily beneficial. Our finding is generally consistent with the results in Ge et al. (2013) for examining the impacts of different state variables as potential observations.

For discussions about the forecast error trend, we focus on the ASRMS error (FIG. 3.16f) again. The results of the ASED are omitted here because of the unavailability of Pt and Qv: the scaling factors at the initial time for these two experiments are zero for TED and LED due to their error-free θ and q_v fields, making

the subsequent scaled results end in infinity. In general, experiments Pt, Qcld, Qpcp, and Qall share a quite similar forecast error trend as they all have the error growing to their maxima at 4:00 UTC, which is 30 minutes earlier than the CNTL. An exceptional error increase is found for the Pt in the last hour. Among these four experiments, the Qall is found to have forecast errors in the smallest magnitude. The Qv its own shows a peculiarly quicker error increase that maximizes at 3:00 UTC, which is one hour earlier than other four experiments and 1.5 hours earlier than the CNTL. After reaching the peak, the forecast error of the Qv rapidly decreases in significantly high efficiency overwhelming all other experiments. According to the trend, the greatest impact of the initial q_v accuracy on model prediction is again demonstrated.

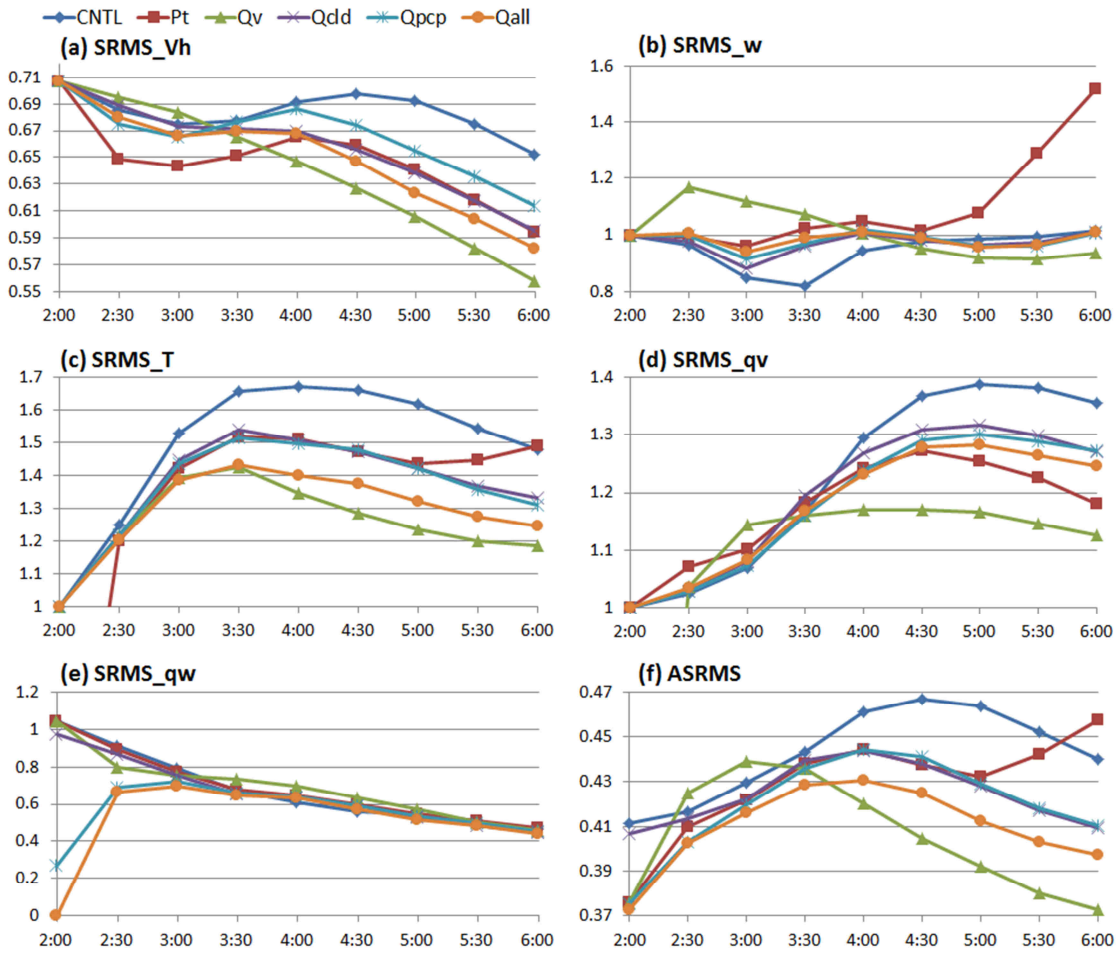

FIG. 3.16 Same as FIG. 3.6, but for the CNTL and five direct insertion experiments.

To verify how the experiments perform on predicting storm structure, evolution, and related microphysical process, their simulated reflectivity is quantitatively evaluated and provided in FIG. 3.17. In terms of the dissimilarity of the forecast *Z* from the truth (i.e., the RMS error, shown in FIG. 3.17a), the experiments with any perfect fields specified is able to provide *Z* prediction systematically better than the CNTL throughout the four hours range of the forecast, suggesting improvement on *Z* predictions of different degree can be achieved by introducing perfect fields of any state variables in the ICs. The best performance is ensured by both the Qpcp and Qall at the

beginning as they have the perfect precipitating hydrometeors, which are the key inputs used for deriving *Z*. No significant RMS error difference is found between the Qpcp and Qall in the entire four hours range, suggesting the absence of initial cloud hydrometeors does not have as critical impact on the *Z* prediction as it does on the prediction of other variables (e.g., V_h, *T*). With no precipitating hydrometeors at the initial time, the CNTL and three hydrometeor-free experiments (i.e., Pt, Qv, and Qcld) begin with a large RMS error (nearly 10), and then have the error gradually reduced as the storms begin to rebuild in their forecasts. Among these three experiments, the Qv shows the most remarkable efficiency on developing the storms from the completely clear air while the error difference between the other two experiments (i.e., Pt and Qcld) is not as significant. After only one hour of the forecast (beginning at 3:00 UTC), the Qv overwhelms all other experiments, even those beginning with perfect precipitating hydrometeors, in terms of significantly lowest RMS errors continuing to the end. The outperformance of the Pt and Qcld over the CNTL, however, is relatively insignificant and only limited in the first two hours.

On predicting the intense convection (30 dBZ and above), the experiments with any of the perfect fields can develop the storms in a decent intensity faster than the CNTL, although underforecast of different degree is still seen for all experiments throughout all times (FIG. 3.17b). Also, it is found the perfect initial q_v field can significantly improve the underforecast issue after one hour of the forecast. On the contrary, all other experiments suffer more serious underforecast, which could possibly be attributed to the failure on maintaining the precipitating hydrometeors from unfavorable evaporation owing to the smoothed (weakened) initial q_v. Even beginning

with a perfect set of precipitating hydrometers, without the support of the favorable q_v field, the Qall and Qpcp soon significantly underforecast the Z intensity and have their bias scores worse than the Qv only after one hour. Similar results are also shown in the ETS verification (FIG. 3.17c): the performances of the Qall and Qpcp are competitively well and also the best among all experiments within the first hour of the forecast, but then significantly surpassed by the Qv at 3:00 UTC and afterward. Performances of the Pt and Qcld are relatively indistinctive compared to other experiments, but their advantage over the CNTL can still be seen. One hour forecast of the composite Z for five direct insertion experiments are shown in FIG. 3.18 for qualitative illustration of the discussions above. Check back to FIG. 3.4b and FIG. 3.9b for the corresponding results of the truth simulation and CNTL, respectively. 3:00 UTC is selected as it is when the Qv begins to exhibit its significant outperformance over other experiments. The distribution of the convective storms with remarkably similarity to the truth simulation given by the Qv distinguishes itself from any of other experiments, again highlighting the great importance of the initial q_v accuracy on storm predictions.

It is also found the values of these verification indices for all experiments tend to converge together as the forecast range gets longer. This phenomenon can be explained by the domination of the model physics which increases with forecast length over that of the IC fineness which is believed to have the larger impact limited in the beginning stage of the forecast. Besides, the mesoscale environmental features retained in the smoothed ICs for all experiments also have continuous effect that gradually contributes to the storm development. Based on the findings throughout this set of experiments, better storm prediction can be ensured by improved IC accuracy through direct insertion

of perfect values. Since the perfect ICs are not accessible in practice, further study is devoted to an investigation into the practical capability of the complex cloud analysis system on improving the cloud-related ICs and subsequent forecasts.

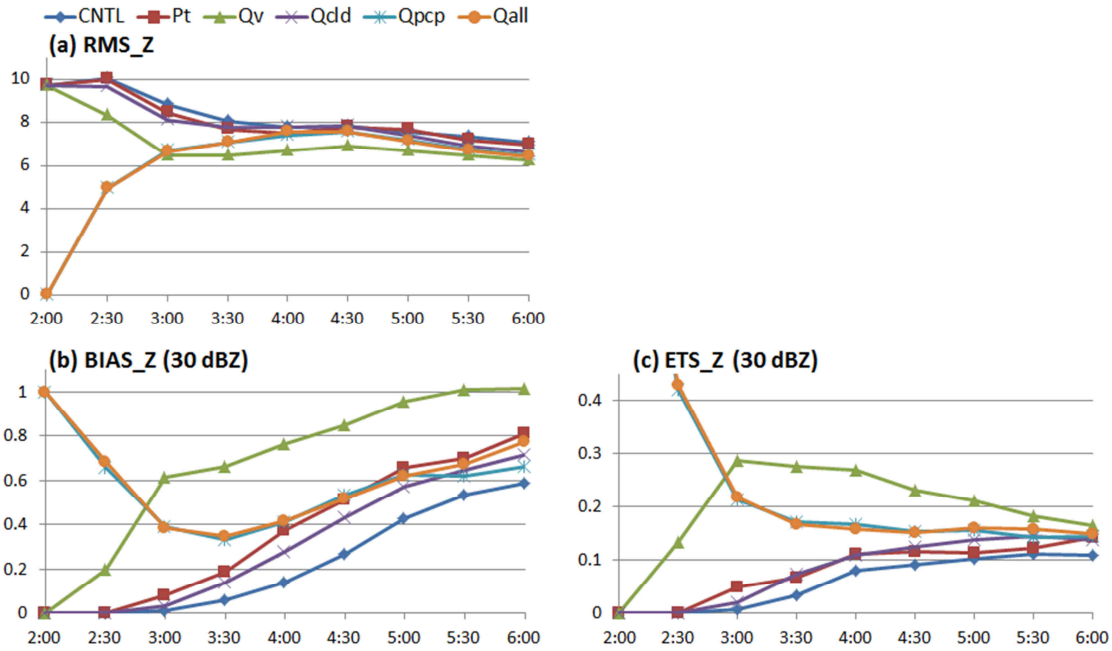

FIG. 3.17 Same as FIG. 3.7, but for the CNTL and five direct insertion experiments.

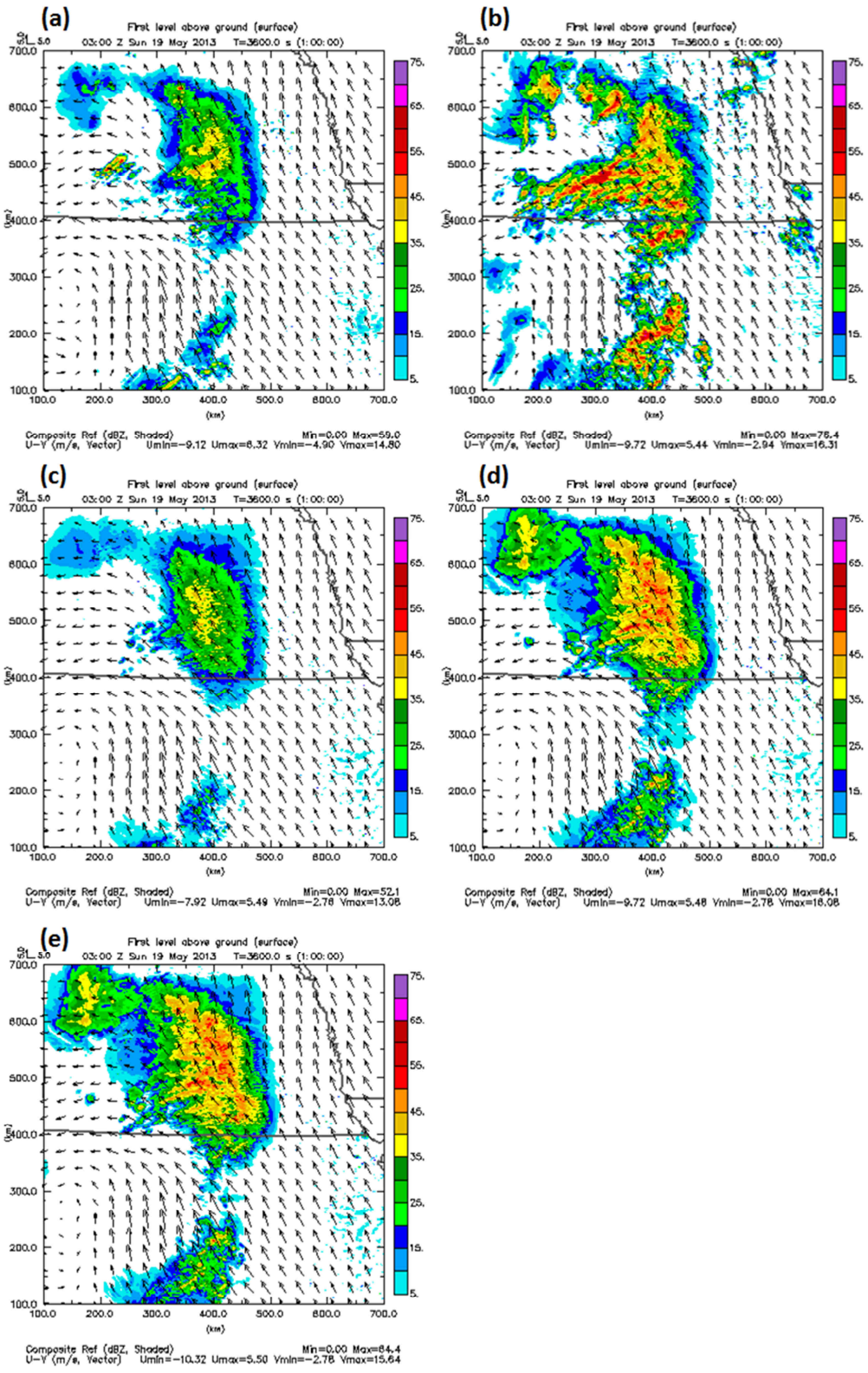

FIG. 3.18 Composite reflectivity and surface winds at 03 UTC for (a) Pt, (b) Qv, (c) Qcld, (d) Qpcp, and (e) Qall. Wind arrows are plotted in 30 km interval.

3.4.3 Summary

Relative importance among the accuracy of various cloud-related state variables in the ICs, including temperature (T), moisture (q_v), cloud hydrometeors (q_{cld}) and precipitation hydrometeors (q_{pcp}), is examined. Experiments are initialized with direct insertion of alternately specified perfect fields from the truth simulation, which are universally available over the entire modeling domain. Model errors are excluded in all experiments by the application of the presumed perfect MYDM microphysics scheme.

On predicting most of the state variables we examine, the accuracy of initial q_v is found to have the largest impact in terms of two aspects: 1) instant very-short-range (within the first hour, specifically) forecast error growth, and 2) significantly absolute advantage on the forecasts at the later stage (two hours and later). The former phenomenon is inferred to be associated with an instant forecast imbalance induced by the perfect and finer resolved q_v field interacting with other error-containing fields while the latter is attributed to the essential criticality of the q_v accuracy required for favorable predictions of the storms and their supportive environment. Other than q_v, the initial availability of the hydrometeor appears to be the second greatest impacting factor, particularly on giving better T forecasts of a longer range, with which the importance of the hydrometeors on developing reasonable cold pools is suggested. Accurate initial T field is found to be relatively crucial on giving the best V_h prediction of a very-short-range (first 1.5 hours, specifically). Benefit of the initial precipitation hydrometeors is more significant than that of the cloud hydrometeors.

The great positive impact of the initial q_v accuracy is again found, and appears to be even more significant on the Z prediction. Even initialized with no hydrometeors, the

experiment with perfect initial q_v can quickly build up the storms in favorable intensity and distribution in only one hour (i.e., spin-up time), when the benefit of the perfect hydrometeors initialization is significantly surpassed by it. Significant improvement on the underforecast Z issue is also promised by the perfect initial q_v after the spin-up time. Impact of the inclusion of cloud hydrometeors appears to be even indistinctive as the storm forecast given by the precipitation hydrometeors alone is competitively good as that given by the all hydrometeors (i.e., cloud + precipitation).

Chapter 4: Cloud Analysis Experiments

4.1 Introduction

Given the importance of the initial condition (IC) accuracy on numerical weather prediction (NWP) modeling which is well demonstrated in existing studies and our earlier investigation, especially for the meso/convective-scale systems that possess highly nonlinear nature, continuous efforts have been made in the current couple decades on developing a variety of data assimilation (DA) techniques toward the goal of a better initialization of model states through optimally combining information from the available observations and background. However, owing to increased complexity in utilization of these modern DA techniques, such as four dimensional variational (4DVAR; Lewis and Derber 1985) DA, the ensemble Kalman filter (EnKF; Evensen 1994; Houtekamer and Mitchell 1998), and the hybrid ensemble/variational approaches (Hamill and Snyder 2000), the considerably expensive computational requirement makes them barely affordable for the real-time operations but only limited within the research scenario.

Several cloud analysis systems/algorithms have been implemented operationally in many weather forecasting/nowcasting institutes worldwide (Auligne et al. 2011): the Local Analysis and Prediction System (LAPS; Albers et al. 1996) first developed by the National Oceanic and Atmospheric Administration's (NOAA's) Forecast Systems Laboratory (FSL), the Nowcasting and Initialisation for Modelling Using Regional Observation Data Scheme (NIMROD; Golding 1998) used by the United Kingdom Meteorological Office (UKMO), and the Rapid Refresh version of the Rapid Update Cycling model (RUC/RR; Benjamin et al. 2004) used for current operations at the

National Center for Environmental Prediction (NCEP). The main goal of these cloud analysis systems, in spite of various approaches, is to specify the hydrometeor (i.e., cloud and precipitation) fields and adjust related in-cloud thermodynamic fields (i.e., temperature and moisture) for the use of NWP modeling. Compared to those advanced DA algorithms described earlier, most of these cloud analysis procedures are realized in a relatively efficient way with the employment of simple physical models or semi-empirical rules.

The complex cloud analysis in the Advanced Regional Prediction System (ARPS; Xue et al. 1995, 2000, 2001) was at first developed by inheriting procedures of the LAPS (Zhang et al. 1998). Since then, a number of modifications (or extension) has been made (added) to improve its efficacy. In additional to the currently available hydrometeor analysis that applies the empirical fitting equations from Kessler (1969) and Rogers and Yau (1989) for rain water and ice species (i.e., snow and hail), respectively, a new procedure, based on the radar reflectivity operators built by Jung et al. (2008), is developed and adopted in this study. The theory of electromagnetic wave propagation that accounts for scattering effects such as dielectric factor and canting behavior of various particles is included in the derivation of these operators. Furthermore, a simple melting model was also involved in charge of the physical feature changes due to the melting process. According to these additional features, the new hydrometeor analysis procedure, with relatively higher complexity, is considered more generally applicable and capable of providing more realistic results. For detailed information about the practical realization of this procedure, please refer to Appendix A. In addition to the original in-cloud temperature adjustment based on the hydrometeor-

associated latent heat release, a new version of adjustment that adjusts the temperature profile towards the moist-adiabat of a low-level lifted parcel with the dilution effect due to the entrainment process included is introduced by Brewster (2002) and available in the current cloud analysis package. The impact difference between these two methods is examined and discussed in Hu and Xue (2007) by the application to a tornadic thunderstorm case study. For the in-cloud moisture adjustment, a simple saturation strategy of the cloudy regions, which has been widely adopted in many studies (Albers et al. 1996; Zhang et al. 1998; Wang et al. 2013) is applied.

In the previous chapter within our OSSE framework, a precursory investigation on the impact of IC accuracy through direct insertion of various sets of perfect (i.e., error-free) state variables is performed. The relative importance of these state variables, in particular the cloud-related ones, is examined and discussed. With these preliminary findings, the room for potential improvement that could be achieved by the cloud analysis is revealed. Since the perfect IC is practically unaccessible, the previous experiments can stand for a set of highest standards. In this chapter, aiming to the ultimate goal of this study, the experiments are directly initialized by the ARPS cloud analysis procedure. Same truth simulation and control run as the previous chapter are used. Besides the hydrometeor mixing ratio analysis, the impacts of two other in-cloud field adjustments, temperature and moisture, as described earlier, will also be examined. The improved ICs, obtained from the cloud analysis, are expected to lead to forecasts better than the CNTL (the baseline) and more importantly, as closer to the standards set by the previous direct insertion experiments as possible. All potential analysis errors will also be listed and described in details.

This chapter is organized as follows. In section 4.2, the setup of the cloud analysis experiments with different configurations are introduced. The comparison among experiments and the independent impact of the applied procedures, including the hydrometeor analysis, temperature, and moisture adjustment, are presented with discussions. At last, a conceptual model of forecast error evolution is provided in section 4.3 based on the findings of our experiment sets from both previous and this chapter. Detailed discussions about various potential error sources and their impacts are provided.

4.2 Experiments with Different Configurations of Cloud Analysis

4.2.1 Design of Experiments

Based on the degraded ICs as used for the CNTL, we conduct four additional experiments which are initialized using the ARPS complex cloud analysis with configurations of different completeness, listed from low to high as: 1) NoAdj, mixing ratio analysis only, without any in-cloud fields adjustment, 2) PtAdj, mixing ratio analysis, with in-cloud potential temperature adjustment, 3) QvAdj, mixing ratio analysis, with in-cloud moisture adjustment, and 4) BothAdj, mixing ratio analysis along with both θ and q_v adjustments.

For the mixing ratio analysis of various precipitation species, the modified procedure, based on the JZX reflectivity operators, as introduced in subsection 2.1.2 is applied. The radar reflectivity observation used for carrying out the analysis is derived directly from the hydrometeors output of the truth simulation (both q_x and N_{tx}). Thus the observation error is excluded. As pointed out in subsection 2.1.2, the ratio among the mass contents (or mixing ratios) of different precipitation species (i.e., q_r, q_s, q_g, and

q_h) is required as the prerequisite for realizing this modified mixing ratio analysis. We reserve this information directly from the truth simulation for more realistic analysis results. However, to emulate the utilization in practice, the constant default values of the intercept parameter N_0 of 8×10^6, 3×10^6, 4×10^5, and 4×10^4 (in m^{-4}) are used for rain, snow, graupel, and hail, respectively in our analysis. With the application of default N_0, certain analysis errors are introduced as the N_0 is actually variable in the truth simulation.

For the in-cloud temperature adjustment, the MA scheme (refer to subsection 2.1.1 for detailed descriptions) is applied. The selection of MA scheme over the LE scheme is owing to its better consistency with the physics of convective storms and corresponding improved forecasts that have been demonstrated in Hu et al. (2006a). Besides, the final in-cloud vertical motion adjustment is omitted for all experiments here since the impact of the thermodynamic variables are of our main interest in this study.

4.2.2 Results and Discussion

An arbitrarily selected 300-km wide cross section across over the intense convective core of the storm denoted by a blue dash line in FIG. 3.4a is shown to exhibit the result of mixing ratio analyses. Mixing ratios of four different precipitation species, rain, snow, graupel, and hail, are provided in FIG. 4.1 and FIG. 4.2 for the truth simulation and the cloud analysis experiments, respectively. In Table 4.1, the mixing ratio maxima of each precipitation species in both selected cross section and the entire modeling domain are listed, from which the general magnitude difference between the truth and the cloud analysis results (i.e., analysis errors) can be discerned intuitively.

First of all, in the truth simulation, the hail species is found in a significant minority with magnitudes two orders smaller compared to other species. It is also seen that the hydrometeors in the truth has wider spatial coverage than the cloud analysis results, especially for the snow and graupel in the upper air (9 km AGL and above). This difference is mainly due to an artificial analysis thresholds set upon the *Z* observation, under which the analysis will not be carried out while zero valued mixing ratios are directly assigned instead. These thresholds are originally designed to eliminate possible contamination from either insignificant precipitation or non-meteorological objects (as described in Hu et al. 2006a). In our cloud analysis experiments, specific *Z* thresholds of 20 dBZ and 15 dBZ are set for the hydrometeor analysis under 2 km AGL and above 2 km AGL, respectively.

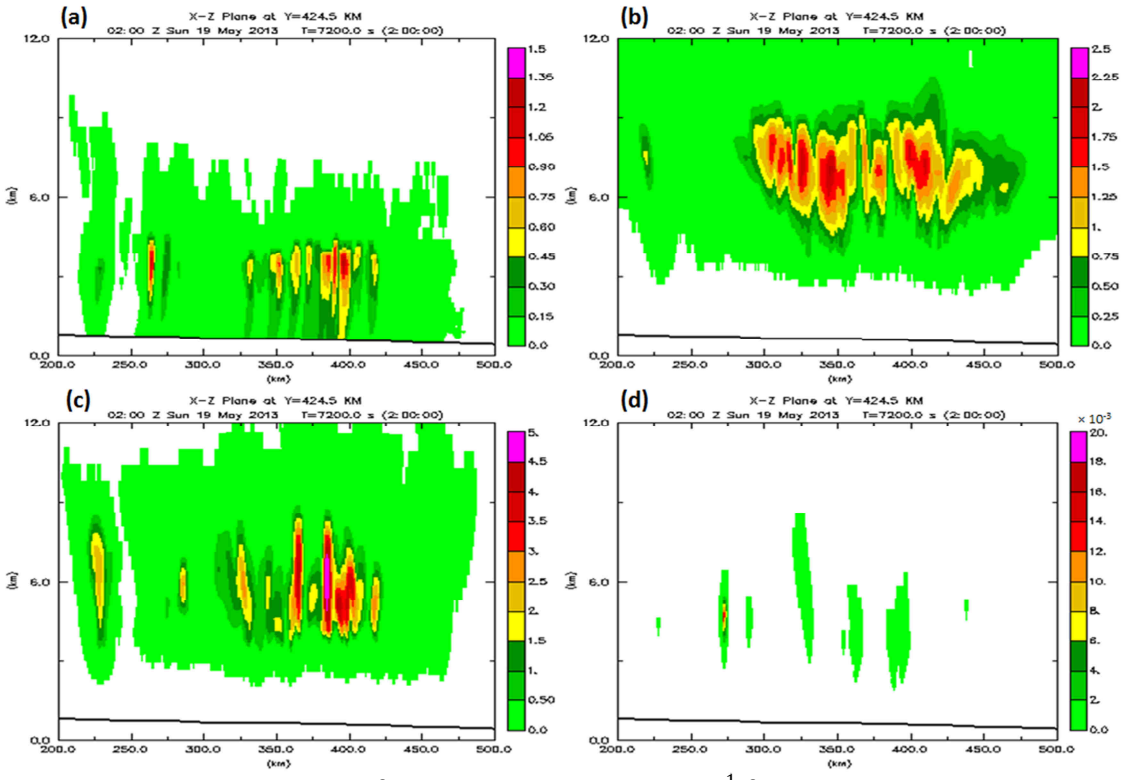

FIG. 4.1 Cross section of truth mixing ratio in g kg^{-1} for (a) rain water, (b) snow, (c) graupel, and (d) hail.

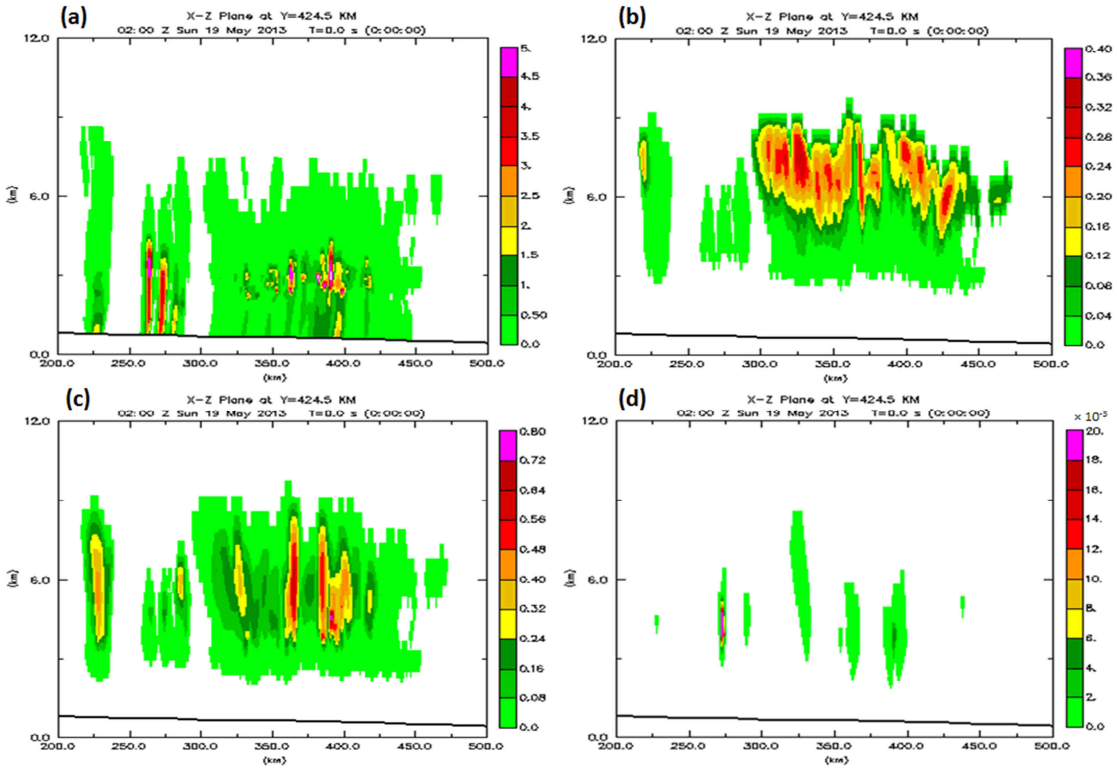

FIG. 4.2 Same as FIG. 4.1, but for the cloud analysis experiments.

Table 4.1 Mixing ratio maxima of the truth and analysis

	q_x maxima (cross section/entire domain) in g/kg			
	Rain	Snow	Graupel	Hail
Truth simulation	1.256 / 3.228	2.099 / 3.614	4.969 / 8.133	0.016 / 0.220
Cloud analysis experiments	19.429 / 20.000	0.326 / 1.750	0.832 / 2.856	0.028 / 0.233

Noticeable analysis errors on mixing ratio are found in our experiments: in contrast to the truth simulation which has rain, snow, and graupel mixing ratios in nearly comparable magnitudes, the analysis result of the experiments is mostly dominated by the rain species which has magnitude one to two order(s) larger than that of the snow or graupel. In other words, the cloud analysis produces a more warm rain-

like result. The main reason that causes this difference is the N_0 values used in our analysis procedure. As mentioned in the previous subsection, default N_0 of constant values is used in our experiments for their solely availability and the readily convenience in most practical applications. However, as the DM microphysics scheme is applied, additional freedom of the spatial variability of N_0 is granted by the predictable N_t, which has been demonstrated in several observation-based studies (e.g., Dennis et al. 1971; Federer and Waldvogel 1975; Knight et al. 1982). The spatially variable N_0, in logarithmic forms for displaying convenience, of rain, snow, and graupel from the truth simulation is provided in FIG. 4.3 for better interpretation of the analysis errors. The hail species is omitted here because of its minority. The default values of different precipitation species used for the analysis are marked in their respective color bars. According to the formula used for carrying out the mixing ratio analysis, as provided in details in Appendix A, the final value of the analyzed mixing ratio is positively-proportional to the N_0. It can be seen in FIG 4.3a that for most regions with presence of significant rain water, for example below the freezing level (FL; around 4 km AGL in our case), the N_0 values are mostly overestimated by the default value if compared to the true values. As a result, positively biased analysis result (i.e., analysis errors) of q_r is led. Similarly, the negative biased analysis errors of q_s and q_g can be explained by the underestimated constant N_0 values compared to the true ones.

Other than the issue regarding the N_0 usage discussed above, there are two other sources of analysis errors we would like to address. First, due to the essential limitation on algebraic formulation, there is incomplete reversibility between the reflectivity forward operators and the mixing ratio analysis procedure. Specifically, this limitation

is owing to the different exponents possessed by the reflectivity operators of rain and non-rain species. Because of this difference, certain approximation has to be made before the contribution of different species on the reflectivity can be combined for retrieving the mixing ratios. Details about this computational error and the practical implementation of approximation can be found in Appendix A. The second error source is from a post-screening process, realized by a set of preset thresholds, applied to the analyzed mixing ratios. To avoid any potential harm on the subsequent forecasts resulted from unrealistic mixing ratio analyses, a set of artificial thresholds is used to screen out analysis result with unreasonably large values. In our study, 20 g kg^{-1} is used for all species, which also explains the maximum of q_r seen in Table 4.1.

Both analysis error sources described above could make the post-simulated Z field, computed from the analyzed hydrometeor fields with Z operators, slightly differ from the original Z observation originally used for carrying out the analysis. In FIG. 4.4 the composite reflectivity simulated from our mixing ratio analysis result (valid at 2:00 UTC; FIG 4.4b) is provided along with the truth simulation (also the error-free reflectivity observation; FIG. 4.4a). Overall, the analysis result matches the truth in decent similarity except for some misses on the weak echoes (as shaded in light blue) at certain regions, mainly the edge of the storm, due to the artificial Z thresholds set for realization of the analysis as described earlier. Besides, some spotted extreme echoes in the truth are absent in the analysis as a result of the post-screening process. Given its relatively minor magnitude compared to the analysis result (~12% negative bias based on the Z maxima), the analysis errors are considered acceptable and believed from resulting in unfavorable impacts on the forecasts

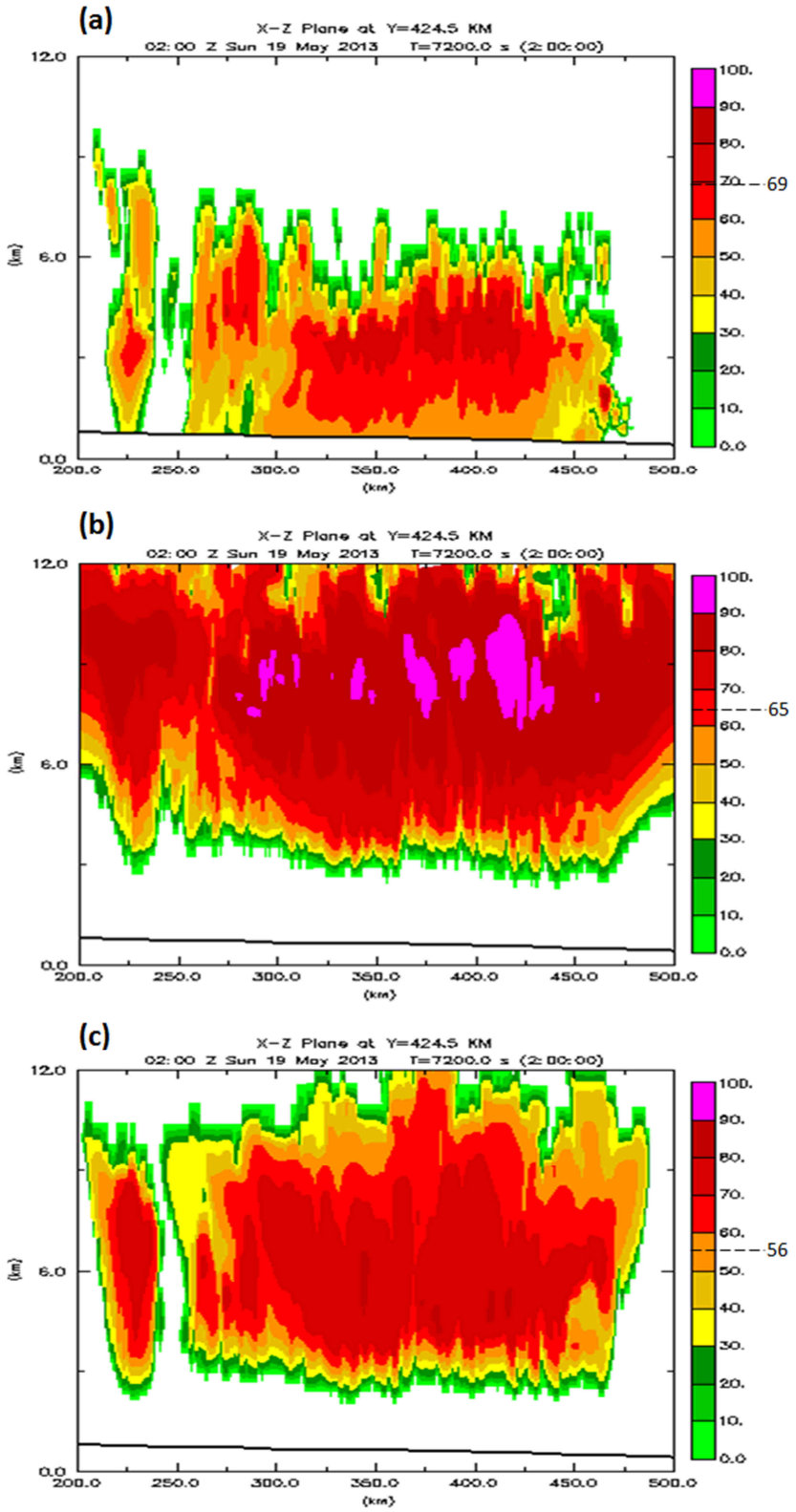

FIG. 4.3 Cross section of 10log(N_0) from the truth simulation for (a) rain, (b) snow, and (c) graupel. The default N_0 values are marked by black dash line on the color bar.

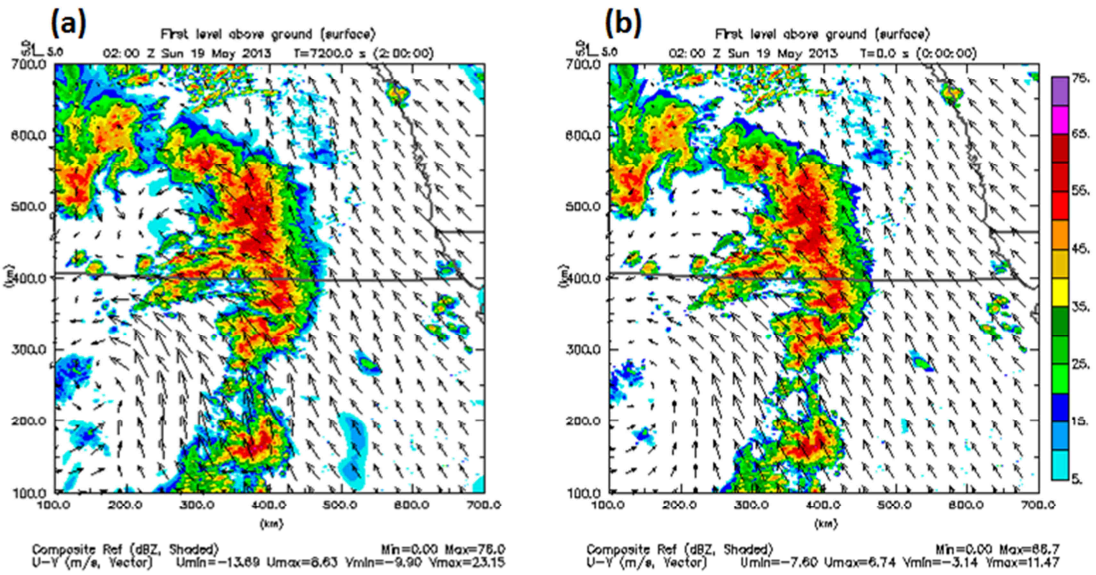

FIG. 4.4 Composite reflectivity and surface winds at 2:00 UTC for (a) truth simulation and (b) experiments with cloud analysis.

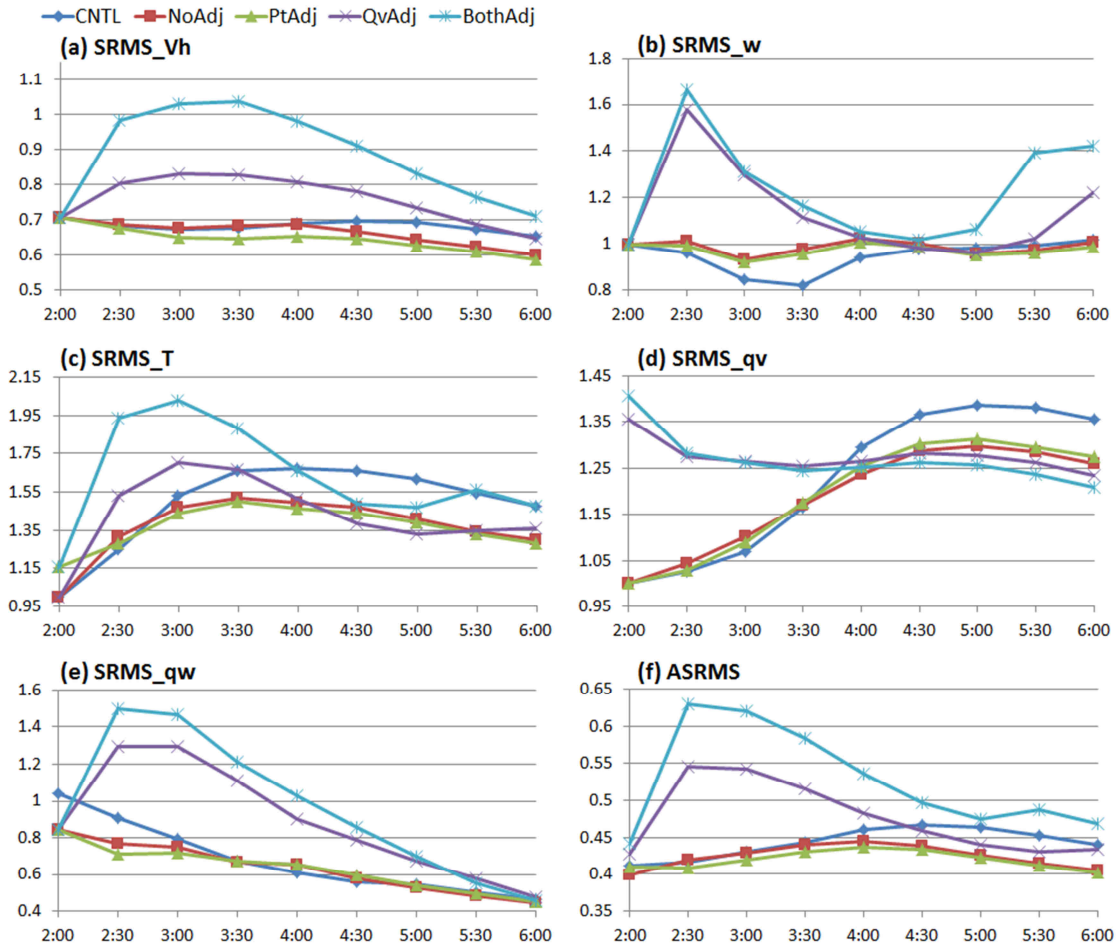

FIG. 4.5 Same as FIG. 3.6, but for the CNTL and four cloud analysis experiments.

In FIG. 4.5, the SRMS error of various model state variables along the forecast range is shown for the CNTL and four cloud analysis experiments. On the prediction of winds (FIG. 4.5a-b), throughout the entire four hours range, the experiments with moisture adjustment (i.e., QvAdj and BothAdj) are found to result in significantly larger error compared to the CNTL, except for an relatively insignificant error difference occurring at 4:30 UTC. It is also noticeable that the significant error growth of the QvAdj and BothAdj is considerably rapid after the initial time once the forecasts are launched. In contrast to the moisture adjustment experiments, experiments without the application of moisture adjustment (i.e., NoAdj and PtAdj) have relatively small errors. Specifically, on V_h prediction, the forecast errors of these two experiments are smaller than the CNTL throughout the entire forecast range, while on w prediction, they are larger than the CNTL within the first two hours and then the error difference turns indiscernible later. By comparing the PtAdj to NoAdj or the BothAdj to QvAdj, the impact of the temperature adjustment is discussed. Between the QvAdj and BothAdj, the BothAdj gives even larger error on prediction of both V_h and w, which may imply certain negative impact associated with the temperature adjustment. However, between the NoAdj and PtAdj, the PtAdj is able to result in systematically smaller forecast error even though their error difference is not as significant as that between the BothAdj and QvAdj. As a conclusion, the benefit of the temperature adjustment on the wind prediction remains valid only in absence of the application of moisture adjustment.

On the prediction of temperature (FIG. 4.5c), it is found the temperature adjustment causes slightly larger SRMS errors at the initial time for both PtAdj and BothAdj, indicating this moist-adiabatic profile based temperature adjustment applied

here does not necessarily provide quantitatively reduced analysis error. The QvAdj and BothAdj again, are found with rapid error growth which makes their errors significantly greater than the other two non-moisture-adjusted experiments within the first two hours of the forecast. While comparing with the CNTL, the moisture adjustment experiments, with the significant error growth in the beginning stage, are even surpassed by the CNTL in the first 1.5 hours. However, after one hour of the forecast, the moisture adjustment experiments runs into a quick error drop and have their forecasts outperforming the CNTL beginning at 4:00 UTC. The QvAdj even outperforms the two non-moisture-adjusted experiments during 4:30 and 5:00 UTC with the lowest forecast error. For the other two experiments without applying moisture adjustment, the error grows more gently and slowly. Compared with the CNTL, slightly worse forecast of the temperature adjustment experiments is found only at the very beginning stage of the forecast (2:30 UTC) while significantly better forecasts are ensured constantly after then. Similar to what is found on the wind prediction, the QvAdj outperforms the BothAdj while the PtAdj outperforms the NoAdj even though the PtAdj has a slightly larger error due to the analysis at the beginning. In general, the group of experiments without moisture adjustment performs better than the group with moisture adjustment, except for a short period between 4:30 and 5:00 UTC during which the QvAdj has the smallest error of all.

On the performance of q_v prediction (FIG. 4.5d), remarkably large RMS errors are found at the initial time given by the two experiments with moisture adjustment, indicating significant q_v analysis errors can be resulted from the current moisture adjustment based on a simple saturation strategy. A slightly larger initial analysis error

of the BothAdj, however, is found compared to that of the QvAdj. This difference is due to procedure for applying these in-cloud field adjustments: as the temperature adjustment is designed to be applied before the moisture adjustment, its effect has also been included in the later-realized q_v adjustment, in which the q_v is retrieved based on the adjusted θ field. Beginning with large errors at the initial time, the QvAdj and BothAdj go through a significant error drop in the first 30 minutes, and then show a nearly constant error trend afterward. As the CNTL show an error trend generally growing with the forecast range, the QvAdj and BothAdj outperform the CNTL beginning at 4:00 UTC and their advantage over the CNTL becomes even significant in the later stage of the forecast. On the other hand, sharing a similar error growing trend with the CNTL, the NoAdj and PtAdj have errors slightly larger than the CNTL in the first hour, but after then, they outperform the CNTL with a significantly slower error growing trend. The four cloud analysis experiments, even beginning with large initial error differences, have their error converged gradually with the forecast range and ended with significantly reduced error differences. Systematic outperformance provided by the group with moisture adjustment over the group without moisture adjustment is found beginning at 4:30 UTC. The impact of the temperature adjustment on q_v prediction is found, by comparing NoAdj with PtAdj or QvAdj with BothAdj, on providing better forecasts at the later stage (1.5 hours and later).

On prediction of the total water mass content (FIG. 4.5e), the great and abrupt error growth is again found given by the experiments with moisture adjustment (i.e., QvAdj and BothAdj). Because of the error growth in these experiments, their initial advantage from the hydrometeor analysis over the CNTL quickly reduces in terms of

significantly larger forecast errors. Even though the errors significantly decrease after one hour of the forecast, the QvAdj and BothAdj still cannot outperform the CNTL within the entire four hours range. On the contrary, the group without application of the moisture adjustment is able to maintain the initial advantage by providing forecasts no worse than the CNTL throughout most of the forecast hours (a slight exception occurs at 4:00 UTC). Similar impact of the temperature adjustment as seen earlier for the wind prediction is again shown here: with the application of moisture adjustment, the temperature adjustment significantly increases the forecast errors throughout the entire four hours range, while in absence of the moisture adjustment, the temperature adjustment shows positive impact, but mostly limited in the very first hour.

On the general forecast performance (FIG. 4.5f), the significant error growth at the beginning stage of the forecast is once again shown in the experiments with moisture adjustment (i.e., QvAdj and BothAdj), further demonstrating the sensitivity of the model prediction to the introduction of storm-scale q_v features as it has been shown in the earlier experiment set with direct insertion of perfect state variables. According to the similar forecast error trend shared, four cloud analysis experiments can be divided into two groups: 1) NoAdj and PtAdj, and 2) QvAdj and BothAdj. Without the application of moisture adjustment (i.e., the first group), the experiments are able to keep a slower error growing trend and earlier error decreasing timing compared to the CNTL, indicating the initial benefit from the hydrometeor analysis is successfully kept in these experiments. When there is no moisture adjustment applied, the temperature adjustment itself, even with a slightly increased temperature analysis error at the initial time, is able to ensure systematically better forecast throughout the entire four hours

range of the forecast. However, while the moisture adjustment is included, the additional application of temperature adjustment tends to further increase the forecast error which is originally found significant. It is worth noting that the experiment with application of moisture adjustment only (i.e., QvAdj) is able to outperform the CNTL with better T and q_v forecasts in the later 1.5 hours after going through the stage of significant error growth, suggesting the moisture adjustment is not necessarily harmful to the prediction of model state variables.

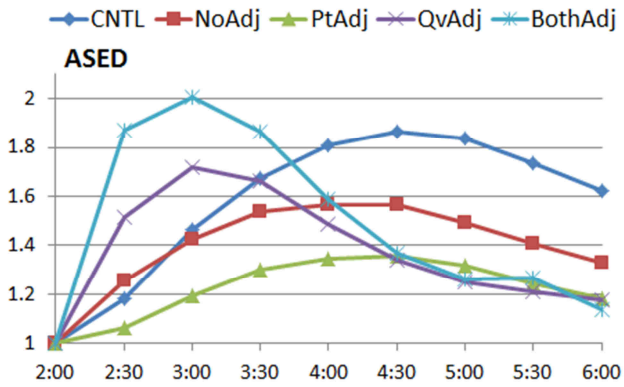

FIG. 4.6 Same as 3.10, but for the CNTL and four cloud analysis experiments.

Similar result of the forecast error trend is further demonstrated by the ASED shown in FIG. 4.6. Significantly more rapid error growth in terms of steeper slope of the ASED is found in experiments with the application of moisture adjustment; however, after reaching the forecast error maxima at 3:00 UTC, relatively sharper error decreasing rates are also shown for them. For experiments without applying moisture adjustment, the forecast errors both increase and decrease in a much slower rate. Among the four cloud analysis experiments, the PtAdj has the smallest error growing rate while the BothAdj has the greatest.

On the *Z* prediction (FIG. 4.7a), it is found the initial advantage from the hydrometeor analysis in the two non-moisture-adjusted experiments can be maintained throughout the entire four hours range in terms of providing forecasts significantly better than the CNTL. The advantage is also seen in the experiments with moisture adjustment, but only limited in the first hour, after which their performances are significantly surpassed by the CNTL. Within the moisture-adjusted group, a relatively advantaged performance is given by the QvAdj at most of the forecast times, except for 3:00 and 6:00 UTC, at which the QvAdj is slightly surpassed by the BothAdj with relatively insignificant RMS error differences. The better performance of the QvAdj over the BothAdj is consistent with the earlier findings on the prediction of most model state variables. On comparison within the non-moisture-adjusted group, relatively significant outperformance of the PtAdj over the NoAdj occurs only between 4:00 and 5:00 UTC, other than which both experiments provide competitive forecasts with similar RMS errors.

While evaluating experiment performances on predicting the intense convection, it is seen that improvements to the underforecast issue (i.e., bias scores significantly smaller than one), which is found serious in the CNTL, can be achieved in different degree by four cloud analysis experiments. However, the experiments with moisture adjustment are found to result in overforecast (FIG. 4.7b) throughout the entire forecast range. The overforecast issue is even more significant for the BothAdj compared to the QvAdj. On the contrary, without applying moisture adjustment, both PtAdj and NoAdj tend to underforecast the intensity of the convection. Additional application of the temperature adjustment (i.e., PtAdj), however, is found capable of significantly

mitigating the underforecast, which is more serious in the NoAdj. One hour forecast of the composite reflectivity of four experiments are shown in FIG. 4.8, from which the overforecast of the QvAdj and BothAdj on storm intensity with extreme echo values (red shaded) is illustrated. Please check back on FIG. 3.4b for the comparison with the truth.

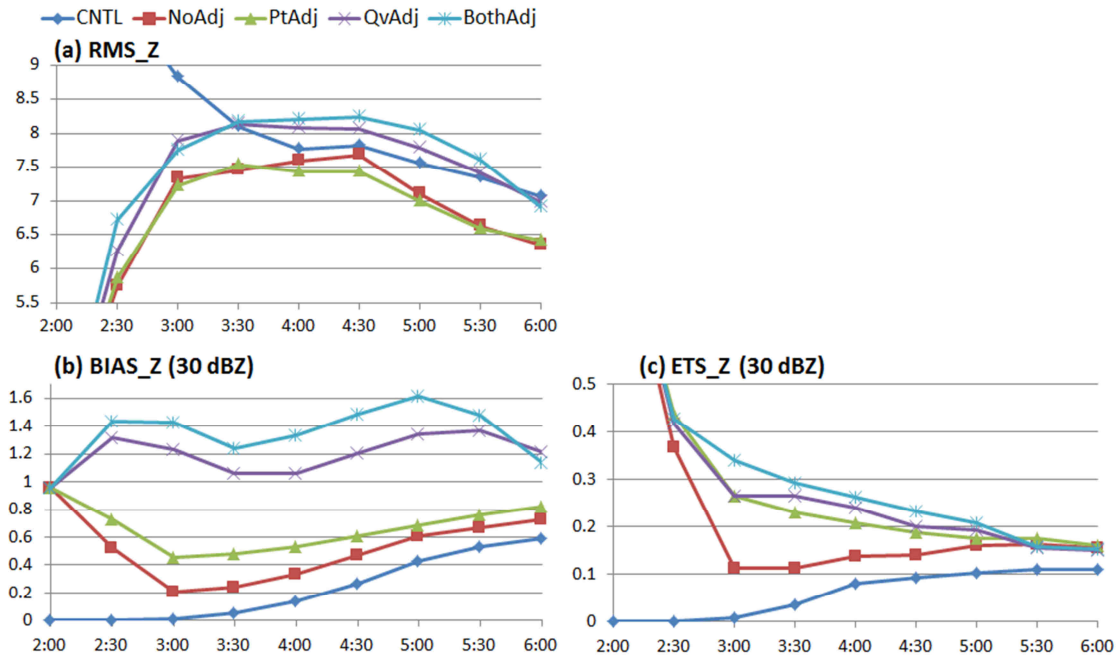

FIG. 4.7 Same as FIG. 3.7, but for the CNTL and four cloud analysis experiments.

In terms of the ETS (FIG. 4.7c), the experiment group with moisture adjustment appear to give higher scores within the first three hours of the forecast. Within the group, the BothAdj scores higher than the QvAdj, which contradicts the general better performance of the QvAdj on *Z* prediction found in the RMS error. The advantage of the BothAdj on the ETS verification is mostly resulted from the design of the ETS calculation (Schaefer 1990). Based on the contingency table used for the statistics of the forecast result in association with the standard (can be either observation or the truth as

in our case), binary result of either “hit” or “miss” (corresponding to the preset threshold) is given. Therefore, no penalty is granted for those hits with over-forecasted magnitudes. In our case, as the cloud analysis updates the cloud-related variables only within the cloud regions, given the perfect reflectivity observation, the overforecast of Z reflects mainly on its intensity, but not the spread (see FIG. 4.8 for demonstration). As a result, even with significantly over-forecasted Z intensity, by providing an in-cloud environment which is highly conducive to the storm development, the BothAdj is able to assure least misses and provide the highest ETS. Conclusions on judging the Z forecast performance, therefore, have to be made with extra caution while verified with the ETS. The issue of the overforecast tendency resulting from the current q_v adjustment is also reported in Schenkman (2012); however, it is addressed for the repeated applications in a manner of high frequent cycling analysis. In his study, this issue is indicated to be associated with the unrealistic middle-troposphere warming, which can be linked with the rapid error growth in T prediction we found earlier (FIG. 4.5c).

The impact of the hydrometeor analysis error on Z prediction can be assessed by comparing the results between the NoAdj and Qall (from the previous chapter). Recall that all hydrometeors in Qall’s ICs are directly inherited from the truth, which is error-free. Note that the differences between these two experiments include not only the errors in precipitation species analysis (as shown in FIG. 4.1, FIG. 4.2, and Table 4.1), but also the errors in cloud species analysis. In general, two experiments share the similar trend in terms of both the RMS error and bias score. Specifically, compared to the NoAdj, the Qall has smaller RMS error by less under-forecasting (i.e., higher bias scores) the convection intensity throughout the entire forecast range. A more significant

impact of the analysis error is seen on the ETS within the first 1.5 hours: the ETS of the NoAdj drops more seriously compared to that of the Qall, which can be also related to the greater underforecast. As a conclusion, the warm rain-like analysis errors generally keep the forecast storms from maintaining proper intensity. We found this deficiency on hydrometeor analysis, however, can be compensated through the application of the moist-adiabatic-based temperature adjustment.

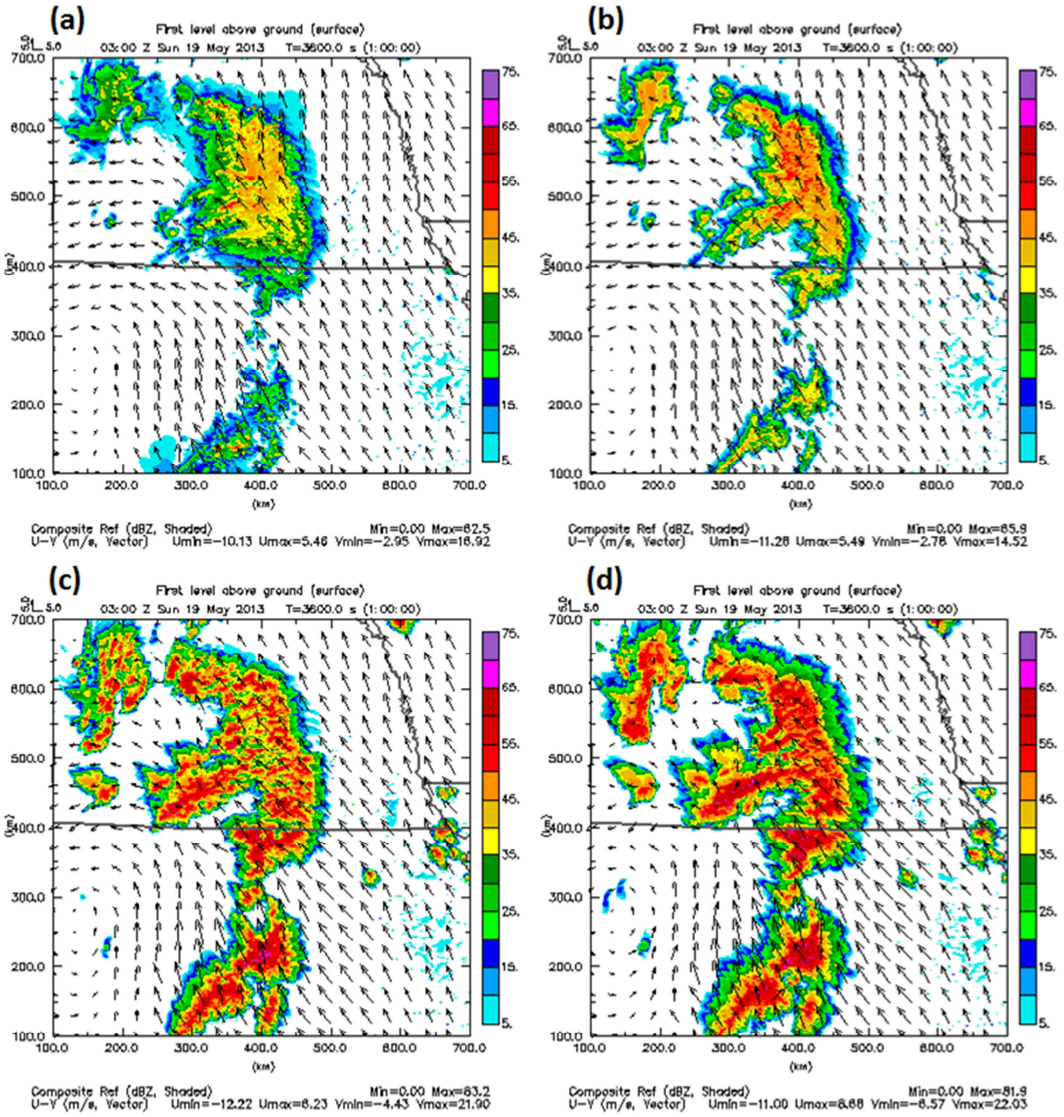

FIG. 4.8 Same as FIG. 3.18, but for four cloud analysis experiments (a) NoAdj, (b) PtAdj, (c) QvAdj, and (d) BothAdj.

4.2.3 Summary

Experiments are initialized using the ARPS complex cloud analysis procedure. Hydrometeor mixing ratios are analyzed with the simulated reflectivity from the truth simulation based on the JZX reflectivity operators, in which the default N_0 values of different precipitation species are applied. Owing to the analysis errors introduced by the constant N_0, the analysis shows a quasi-warm rain result with overestimated rain water mass content and underestimated ice-phased hydrometeor mass contents in comparison with the truth. Besides the hydrometeor analysis, the impact of other in-cloud field adjustments, including the simple saturation moisture adjustment based on the presence of observed radar echo and the temperature adjustment based on moist-adiabatic ascent, are also examined.

It is found the simple saturation in-cloud moisture adjustment results in a q_v analysis with significantly large analysis errors. Beginning with these errors, instant and great forecast error growth, which usually peaks within the first hour, can be resulted on the prediction of most state variables (e.g., V_h, w, T, q_w). While being applied alone, the additional application of in-cloud temperature adjustment is able to provide improved forecast results, especially on the prediction of winds and T. Based on the hydrometeor analysis, the additional application of the temperature adjustment is found capable of reducing the forecast error growing rate while the additional application of the moisture adjustment tends to increased error growing rate. However, while both adjustments are applied, an even significantly enlarged forecast error growing rate can be resulted.

On the prediction of the reflectivity, the greatest impact of the moisture adjustment is shown on over-forecasting the Z intensity with nearly unrealistic extreme

values. Under-forecasted Z intensity, on the contrary, is found for the experiments without applying moisture adjustment. However, the temperature adjustment appears to work well on alleviating the underforecast issue. While evaluating the experiment performance on predicting intense convection (30 dBZ and above), higher ETS can be achieved by the experiments with moisture adjustment because their significant overforecast tendency. Based on our findings, we conclude that further improvements on the current moisture adjustment based on a simple saturation strategy are required for avoiding unfavorable precipitation forecasts. Besides, the under-forecasted result given by our error-containing hydrometeor analysis also calls for potential improvements on this procedure, from which more properly maintained precipitation intensity is expected to be achieved through a more accurately specified hydrometeor fields.

4.3 Conceptual Model of Forecast Error

Based on the findings from the experiment sets conducted in this and the previous chapters, we construct a conceptual model of forecast error that enables a general understanding of the relative importance of various individual impacting factors as discussed earlier. General forecast performance, including the predictions of winds, temperature, moisture, and hydrometeors, is assessed in developing this model, from which the storm predictability, both intrinsic and practical (Lorenz 1995), is revealed and discussed.

Before looking into the conceptual model, we would like to provide an overview of a relevant study on the scale dependence of the predictability of precipitation patterns, conducted by Surcel et al. (2015). In their study, a quantitative measure of the

precipitation predictability, realized with a decorrelation scale, was proposed and applied to examine various forecasting methods. Specifically, the decorrelation scale λ_0 is defined as an upper scale limit, below which the forecasts show no predictability. It was concluded from their results, based on 22 precipitation cases during the 2008 HWT Spring Experiment, the λ_0 always increases with forecast lead time, regardless of the forecasting methods. Furthermore, they found the longer-than-two-hours predictability of the model state at meso-γ and meso-β scales can be introduced by the radar data assimilation, while comparing to those non-radar data-assimilating ensemble members.

The study reviewed above focused on predictability mainly at the mesoscale. In addition, because of the practical forecasting systems used for conducting their study, the practical predictability, which is defined with the inclusion of the model errors (Lorenz 1995), was referred. Compared with their study, the predictability at up to convective-scale is included in the object of our exploration with the set-up of the 1-km model spacing, and the forecasts in a four-hours short range are examined. Furthermore, within the OSSEs framework, most of our experiment sets are performed under the assumption of perfect model, from which the intrinsic predictability can be investigated with the specifiable IC errors. In addition to the intrinsic predictability, the practical predictability is also available for discussion in our study through certain experiments with microphysics errors (presented in section 3.3).

Discussions upon the forecast error conceptual model (provided as FIG. 4.9) and associated impacting factors for the storm prediction are summarized point by point as follows:

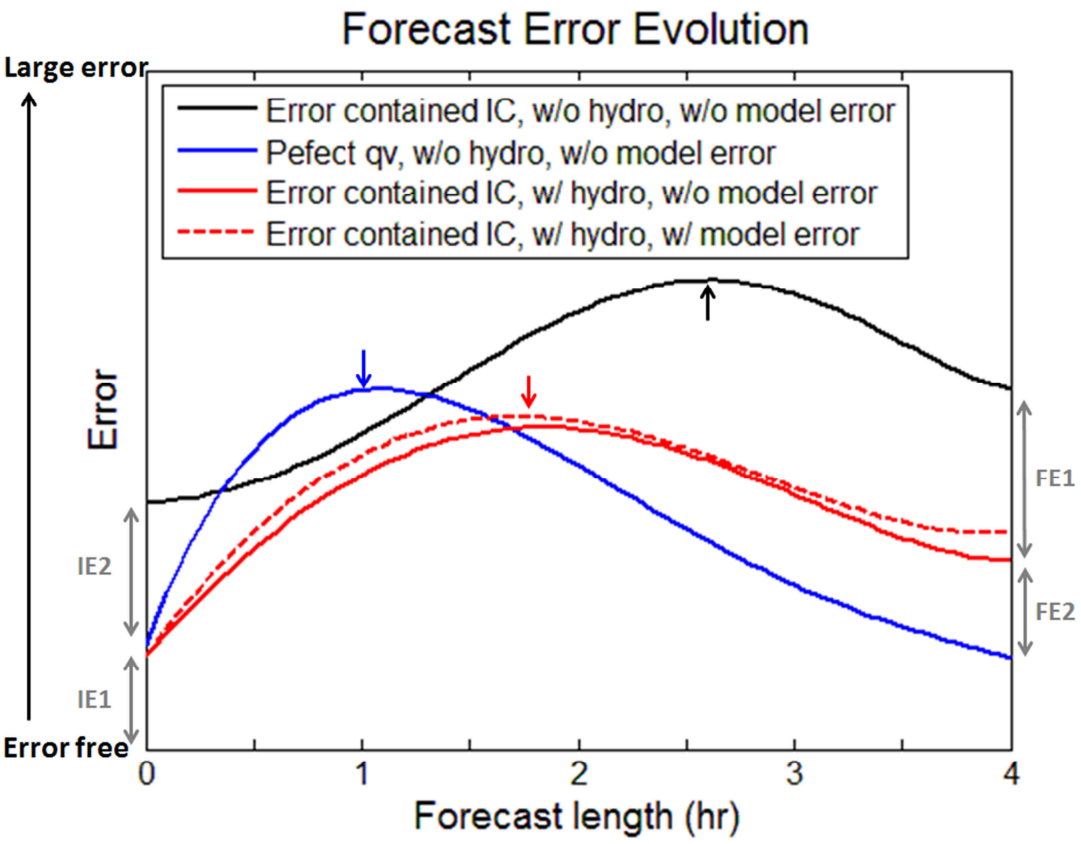

FIG. 4.9 Conceptual model of the forecast error evolution corresponding to IC accuracy (including the resolution fineness of moisture field and hydrometeor availability) and model perfectness. Details about the arrow marks are provided in the context.

(i) Initial condition error (shorten as IE, denoted by the gray double headed arrows in the conceptual model):

While the model perfectness is assumed, the initial condition error is the major source that causes the subsequent forecast errors. This is also the scenario under which the intrinsic predictability has been discussed. The critical impact of the IC uncertainty on the NWP model forecasts was first addressed by Lorenz (1963) and all the subsequent data assimilation studies were dedicated to the improvements of this issue. For most regional forecasts, the initial condition errors usually come from the application of the global model outputs or global analyses, which are coarse in their

spatial resolution insufficient for characterizing the critical features at finer scales. Besides, the unavailability of the hydrometeor information, which is common in these global-based ICs, also introduces the uncertainty that can significantly limit the predictions of moist convection. In our OSSE study, the uncertainty described above is emulated by a degraded IC. In the conceptual model, the total IC error magnitude of the black curve featured by the summation of IE1 and IE2 includes both 1) spatial resolution deficiency and 2) hydrometeor unavailability. This great error can be significantly reduced in a magnitude of IE2 after the inclusion of either perfect moisture field (as the blue curve) or hydrometeors (as the red curves). These improvements, theoretically, can be expected by utilizing reasonable hydrometeor mixing ratio analysis or in-cloud thermodynamic field (i.e., θ or q_v) adjustments through the cloud analysis procedure. However, the magnitude of the improvement may not be as large as the IE2 owing to the analysis errors in practice.

(ii) Impact of the initial condition error

While observing the forecast error evolution of the various experiments, we always see a trend of error growth showing at the beginning of the forecast regardless of the IC variety, from which the impact of the initial condition errors is inferred. In other words, as long as there is initial error present, this general behavior of the forecast error can always be expected. When the NWP model reaches its full physical complexity and with which a reasonable storm-associated environment is built, the negative impact of the initial error is eventually overcome and as a result, the forecast error begins to decrease. We simply refer the beginning error growth period as the “initial-condition-error-dominated stage” and the later period as the “model-physics-dominated stage”.

Another reasonable explanation for the error decrease at the later stage of the forecast in our OSSE experiments can be associated with the design of the smoothed initial condition. As shown earlier in section 3.2.2, certain critical mesoscale environmental features are still kept in the background for most experiments. Along with the forecast range, these mesoscale signals continuously contribute to force and eventually develop a mesoscale structure of the storm comparable to the truth. The longer impact on the forecast given by the larger-scaled features in the IC we find here is consistent with the predictable scale which is concluded in Surcel et al. (2015) to increase with the forecast lead time.

(iii) Length of the initial-condition-error-dominated stage

With different informative IC (denoted by curves in different colors), the length of the initial-condition-error-dominated period (IED period, hereafter) varies. The end of the IED period is marked with arrow in respective color for each experiment. It is seen the least informative IC (black curve) results in a longest IED period (~2.5 hour). Compared to that, the additional hydrometeor information in the IC (red curves) appears to shorten the IED period for nearly an hour. This advantage, mostly in terms of alleviating the model spin-up time, is also what one can expect from the utilization of a reasonable hydrometeor analysis. Again, the practical magnitude of the advantage would be dependent on the fineness of the analysis (i.e., analysis errors). An even shorter IED period of only one hour is found for the experiment with perfect initial moisture field (blue curve), even though no hydrometeor information is included in the IC. The advantage of the moisture accuracy on quickening the forecast error decrease is relatively significant since no other state variables we examine (i.e., θ, q_{cld}, or q_{pcp}, not

shown in the conceptual model) is able to shorten the IED period in a competitive efficiency.

(iv) Forecast error magnitude

The impact of the IC uncertainty also reflects on the forecast error magnitude. Beginning with a largest IC error given by the least informative initial condition, the experiment denoted by the black curve is most likely to be expected to show the forecast error greater than other experiments throughout the forecast range. However, a larger forecast error is found given by the experiment with perfect initial moisture field but no hydrometeors in its IC which is denoted by the blue curve within the first 1 to 1.5 hours. This large error magnitude at the very beginning stage of the forecasts suggests a great sensitivity of the model forecast to the moisture accuracy in the IC, which induces certain forecast imbalance through its interactions with other error-containing fields. However, as soon as its IED period is passed, the perfect initial moisture experiment turns to drop its forecast error rapidly in a most significant efficiency (i.e., with a steepest slop) and ends up with a smallest final error (FE) magnitude among all experiments. For the experiments with perfect initial hydrometeors denoted by the red curves, their forecast errors remain in relatively smaller magnitudes compared to the no initial hydrometeor experiment (the black curve) in the entire four hours of the forecast range. Around 1.5 to 2 hours of the forecast, the perfect initial moisture experiment begins to surpass the perfect hydrometeor experiment with significantly smaller forecast errors, suggesting the greater positive impact of the initial moisture accuracy over the hydrometeors. The final forecast error difference (as denoted by the FE1 and FE2 in the conceptual model) is also found mostly associated with the IC uncertainty: the FE1 is

attributed to the benefit of initial hydrometeors, while with the perfect initial moisture field alone (hydrometeor is not even included), a greatly reduced magnitude of the final forecast error as large as FE1+FE2 can be obtained.

(v) Impact of the model error

The model error we discuss here is mainly caused by the microphysics treatments. The forecast performance difference resulted from the applications of perfect and imperfect microphysics schemes is distinguished by the solid and dash line (both in red). The general trend of the forecast error evolution, in terms of the length of the IED period, remains quite similar for the two experiments. Beginning with the same IC, the experiment with perfect microphysics tends to give smaller forecast errors throughout the entire four hours range in comparison with the imperfect microphysics experiment. However, the impact of the model microphysics errors on the prediction of model state variables (in terms of the forecast error difference between two experiments here) is not as significant as that caused by the initial condition error. On the other hand, in terms of providing a systematically better prediction of reflectivity in up to four hours range, the perfectness of microphysics is found much more crucial (not shown here; Refer to section 3.3 for details).

The significance of the forecast error conceptual model we propose above is further discussed here. Since the model is constructed based on the findings of a single case study using one specific forecasting system, its universal validity has to be addressed. Besides, it is worth noting that in this conceptual model, instead of the absolute values such as the SRMS errors shown earlier in each experiment set, only the relative magnitudes among the curves (i.e., experiments) are valid. Quantitative

variations in the properties described above, such as the initial errors, length of the IED period, and error growth magnitude, may be found among different cases studied or different forecasting systems applied (i.e., case- or system-dependent); however, according to the general trend of the predictability varying with forecast range concluded with various forecasting methods and the dataset of a reasonable size (22 cases) in Surcel et al. (2015), these variations are expected to stay in a relatively insignificant magnitude that would not alter the relative positions appearing among our experiments. As a result, we conclude our conceptual model should be robust in a qualitative sense and its significance is thus assured.

Chapter 5: Improving Moisture Adjustment in Cloud Analysis

5.1 Impact of Moisture Accuracy

From the experiment sets presented in the previous chapters, it has been established that among the various state variables the cloud analysis attempts to improve, the moisture (q_v) plays the most important role in terms of its prompt and significant impact on storm prediction. Even with no errors included, the insertion of hydrometeor fields can only provide limited benefit in the presence of initial moisture error. The impact of the initial moisture accuracy is found even more critical on predicting reflectivity.

Realizing the importance of moisture accuracy on model predictions and the limited efficacy of the current in-cloud moisture adjustment, efforts are made in this chapter to examine the validity of the simple saturation strategy and an optimally-specified in-cloud moisture field, upon which a modified procedure making use of the vertical velocity information is proposed and its effectiveness on providing improved forecasts is preliminarily demonstrated.

5.1.1 Validity of Current Moisture Adjustment

As described earlier in subsection 2.1.1, in the current ARPS complex cloud analysis a simple empirical rule-based strategy is used to adjust the in-cloud moisture field: 100% relative humidity (RH) is assigned for the cloudy regions based on both LCL analysis and the presence of significant radar echoes. Under this strategy, it is likely that the background moisture field is actually gone through a one-way enhancement process instead of a so-called “adjustment”. In our OSSE framework with

the availability of the truth, it is possible for us to further examine the validity of the simple saturation strategy.

In FIG. 5.1 the cross section, selected same as that shown in the previous chapter, is used for the demonstration of the RH fields. Both the background RH field and the counterpart adjusted using the current simple saturation strategy are exhibited as FIG. 5.1b and 5.1d, respectively. By comparing these two fields, an instant visualization of the effect of the q_v adjustment can be gained. Moreover, if one looks into the true RH field (FIG. 5.1a), the dissimilarity of a considerable degree between it and the adjusted result can be discerned. In the truth simulation, the saturation is found to occur mostly above the height of 0 °C (i.e., the freezing level, FL). Below the FL, the RH field exhibits relatively high spatial variability; within the regions with significant radar echoes, even though the high RH values (80% and above, shaded in red) are found as the majority, RH value as low as 40% (as shaded in light blue) may exist as well. The differences between the true and adjusted RH fields imply the inconsistency existing between the model microphysics and the empirical rule employed; most likely, the empirical rule is too simplified to characterize the nature of RH variability and thus has its deficiency. By comparing with the true RH field, it is shown the simple saturation strategy is generally valid well above the FL, where most of the cold cloud formation anad sourced. Furthermore, according to the equation proposed by Goff and Gratch (1946), it is easier for the air parcels to reach saturation under a colder environment since less water vapor is required. On the contrary, more water vapor is needed for reaching saturation under the FL. On the other hand, as a certain amount of the rainwater appearing under the FL is not formed in situ originally but converted from the

iced phase precipitation aloft, the presence of precipitation under the FL is not necessarily contradictive to the unsaturation. In fact, the existence of the "unsaturated downdraft" driven by the evaporation of falling rain has been drawn attention to and discussed in many early studies (Betts and Dias 1979; Byers and Braham 1949; Emanuel 1981; Leary 1980) in both observation- and simulation-based approaches. In addition, it is also indicated that entrainment of the relatively dry air from the non-precipitating area can result in reduced liquid water content (Wagner et al. 2013), particularly at the areas of the storm edge.

The difference between the true and the background RH fields as used for the CNTL (FIG. 5.1c) gives us an idea about how much adjustment (in either enhancement or reduction direction) has to be done indeed for a more accurate moisture initialization. Note that the background RH field is derived as a function of the three-dimensional spatially smoothed T field (refer to section 3.2). Within the boundary of the cloudy regions denoted by the significant radar reflectivity contours (15 dBZ), we find a large amount of underestimated RH values (i.e., negative difference shaded in blue), which requires moisture enhancement, are given by the background; on the contrary, a certain amount of significant RH overestimation (i.e., regions shaded in warm colors) in the magnitude up to 40% that needs to be reduced can also be seen appearing mostly under the FL. Consequently, given the bi-directional tendency of the RH difference between the truth and background as illustrated and discussed above, our concern upon the validity of the enhancing-only strategy utilized in the current moisture adjustment (FIG. 5.1d) is brought.

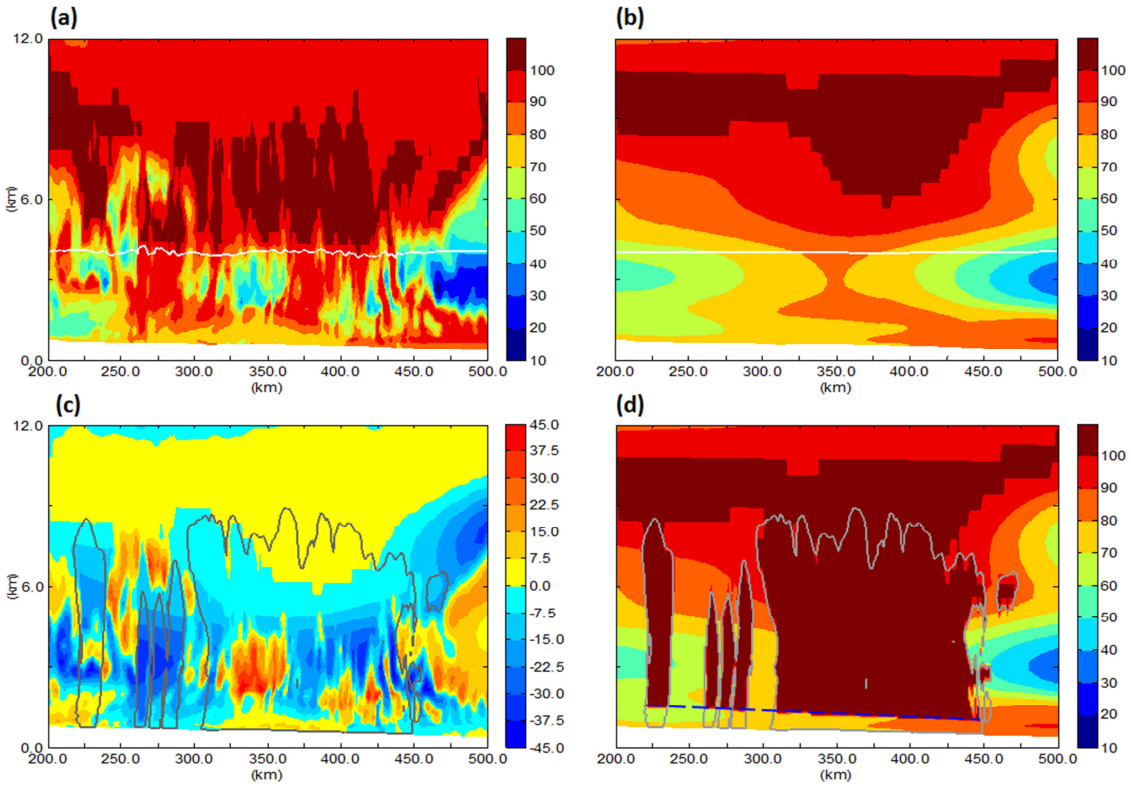

FIG. 5.1 Cross section of RH field (%) for (a) truth simulation, (b) background (CNTL), and (d) QvAdj. The RH difference between the truth and CNTL (CNTL-truth) is given as (c). The height of 0 °C is denoted by white solid lines in (a) and (b). 15 dBZ echo boundary is drawn by gray contour in (c) and (d) for a rough illustration of cloudy regions. The LCL is denoted by a blue dash line in (d).

The quantitative moisture analysis error resulted from the current q_v adjustment has been presented in terms of the SRMS error at the initial time in FIG. 4.5d. Overall, by comparing with the non-adjusted q_v field given by the CNTL (or other experiments without applying moisture adjustment), an extra error up to 35.5% is found introduced by the application of q_v adjustment alone, as denoted by the QvAdj. An even larger analysis error is found to be introduced by applying both temperature and moisture adjustments (Refer to subsection 4.2.2 for related discussions). In other words**,** the current q_v adjustment does not improve the initial moisture field but actually harm it by

dragging the background field father away from the true field. In FIG. 5.2, the along height q_v dissimilarity from the truth, in terms of the RMS error, of the background (CNTL), perfect direct insertion experiment Qv (presented in section 3.4), and cloud analysis experiment QvAdj (presented in section 4.2) are shown. The RMS errors are calculated within the verification domain as described in Chapter 3. With a universal (i.e., entire domain wide) insertion of the perfect q_v, the Qv results in zero error throughout the entire vertical layers. Beginning at the surface, the CNTL and QvAdj share quite similar RMS errors with no significant difference. The QvAdj is then found with an abrupt error increase shown at the ninth model level, from where its error begins to greatly diverge from the CNTL, which shows a relatively gentle error increase with height. of the CNTL and QvAdj begin to diverge at the ninth model level. The model level 9, as denoted by the blue dash line, is inferred as the bottom boundary of the q_v adjustment application. The height of this model level is generally consistent with the LCL denoted in FIG. 5.1d. On the contrary, it is relatively hard to declare an exact level where the CNTL and QvAdj have their error merged since it appears to be a gradual process occurring with the height (above the model level 25); however, it can still be told to be generally coincident with the average height of the significant echo top, which is also where the application of qv adjustment ends at. Within the layers of q_v adjustment application, a considerably great amount of analysis error, in terms of the RMS error difference between the CNTL and QvAdj, is shown with a maximum located around the level 20 (~2.2 to 3.0 km AGL), which is found consistent with the regions where the greatest RH overestimation occurs (shown in FIG. 5.1c). Given the

examination results shown here, the questionable validity of the simple saturation moisture adjustment is further affirmed.

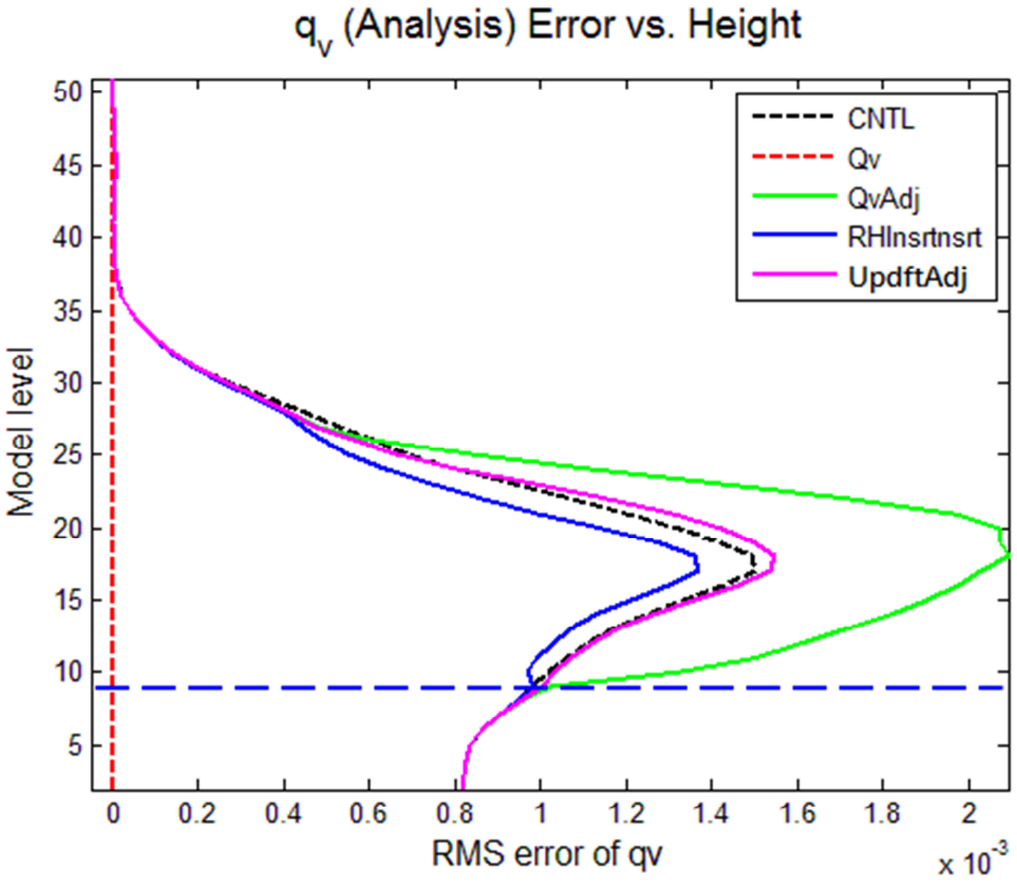

FIG. 5.2 RMS error of q_v as a function of height (in terms of model level) at forecast initial (2:00 UTC). Experiments with and without hydrometeor analysis are represented by solid and dash lines, respectively. The ninth level is marked with a horizontal blue dash line. See context for detailed description.

5.1.2 Design and Test of a Potential Modified Moisture Adjustment

After a thorough examination of the validity of the current moisture adjustment on providing moisture analysis, its room for potential improvements is revealed. In this subsection, we propose an optimally improved moisture adjustment based on the true RH variability and test its impact on the resulting moisture analysis and forecasts.

Through this investigation in which the validity of this optimally specified in-cloud moisture field is demonstrated, the potential effectiveness and value of a practically modified adjustment procedure, which will be presented in the next section, is assured.

Given that the simple saturation strategy utilized in the current moisture adjustment tends to overestimate the moisture field, especially for regions under the FL, certain modification on the strategy has to be sought for a more accurately specified moisture field with which the undesired analysis errors can be avoided. Complying with the convention adopted for executing the current procedure that the direct adjustments are actually made on the RH field from which the final moisture filed is derived, an instinctively modified procedure is proposed to directly insert the true RH values into the background in the cloudy regions. The experiment with this "optimally" modified q_v adjustment is named "RHInsrt" and its analyzed RH field is illustrated in the cross section shown in FIG. 5.3c. Since the direct insertion of the perfect RH is limited only within the cloud regions, the analyzed RH filed shows some noticeable discontinuities at the cloud/precipitation boundary. Furthermore, in contrast to the forecast verification which is conducted in a relatively larger domain that includes both precipitating and non-precipitating areas, the quantitative impact of this cloudy region-limited q_v improvement on the subsequent forecasts is therefore of our interests for investigation. It is worth noting that in spite of the perfectness of the true RH values inserted, the RHInsrt still suffers errors in its final q_v analysis of. The analysis errors mainly result from the smoothed T field in the background used for the RH to q_v conversion. The q_v analysis result of the RHInsrt is provided in FIG. 5.3d, along with the true q_v field (FIG. 5.3b) for comparison. Visualized with the cross section as presented, the modified q_v

adjustment generally captures most fine features of the truth and accurately specifies a comparable q_v field. Some minor differences, mostly occurring above the FL, are found: the analysis of the RHInsrt seems to fail on depicting some convective-scale q_v fluctuations that are present in the truth, which can be mostly attributed to the horizontally homogeneous background temperature distribution (as demonstrated by the 0 °C lines shown in FIG. 5.3) and the nature of the low water vapor content at high levels. Another difference is found to occurr near the surface: with the in-cloud area limit, the analyzed q_v field of the RHInsrt shows some significant underestimations under the LCL, which is known as the lowest boundary of the clouds (i.e., cloud bottom).

Quantitative improvement of the q_v analysis provided by the RHInsrt can be evaluated by the RMS error shown in FIG. 5.2. By comparing with the background q_v (denoted by the black dashed line), significantly reduced errors throughout the entire q_v adjusting layer are seen for the RHInsrt (denoted by the blue solid line) while the general trend of the vertical error distribution is retained. Provided for a general perception, at the level 18, where most of the largest errors occur, the optimally modified q_v adjustment (i.e., RHInsrt) makes a 9% error reduction over the background (i.e., CNTL) while the simple saturation q_v adjustment (i.e., QvAdj) results in a 40% error increase over the background.

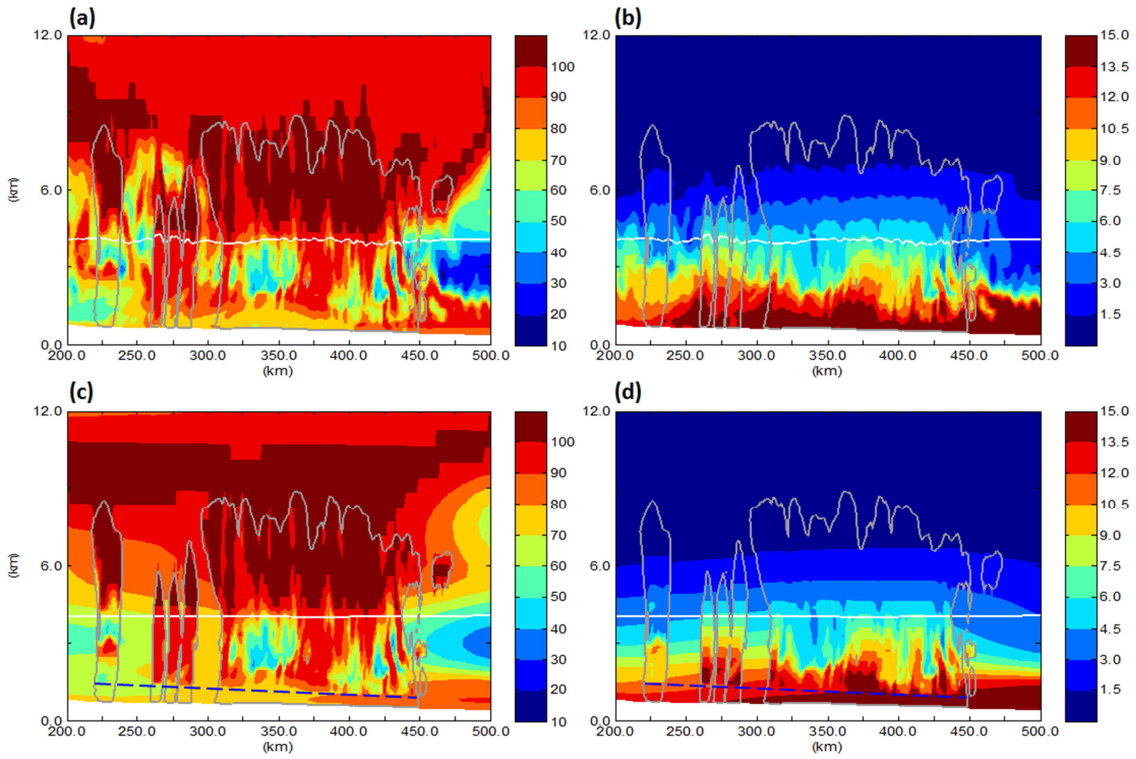

FIG. 5.3 Cross section of RH field (%) for (a) truth simulation and (c) RHInsrt. Cross section of q_v field (g/kg) for (b) truth simulation and (d) RHInsrt. Corresponding 0 °C levels are denoted by white solid lines. 15 dBZ echo boundary is drawn by gray contour. The LCL is denoted by blue dash line for experiment RHInsrt indicating the bottom boundary of adjustment.

Other than the modified q_v adjustment, the same hydrometeor analysis as performed for all the cloud analysis experiments presented in the previous chapter is realized for the RHInsrt. The in-cloud temperature adjustment, however, is turned off to distinguish the individual impact of the q_v adjustment, which is the aim of our investigation. Besides, while discussing the impact of the optimally modified moisture adjustment by looking into the forecast performance of the RHInsrt, we also reprise certain experiments from the previous chapters such like the Qv (from the direct insertion experiments), QvAdj and NoAdj (from the cloud analysis experiments) in

addition to the CNTL for comparison. In the following discussion, the Qv and QvAdj will be termed as the TrueQv and SatAdj, respectively, for a better clarity.

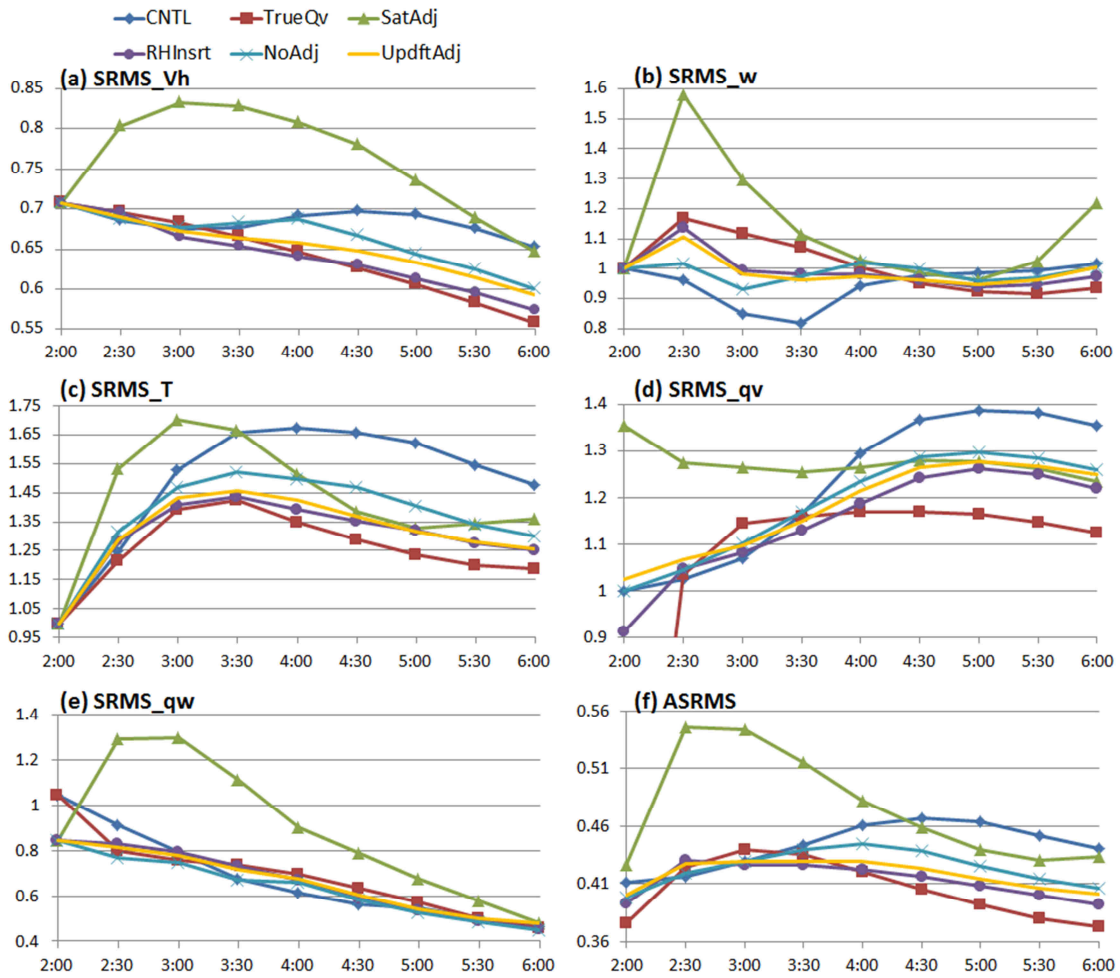

FIG. 5.4 Same as FIG. 3.6, but for the CNTL, TrueQv, NoAdj, SatAdj, RHInsrt, and UpdftAdj.

Quantitative verification of various predicted state variables are provided in FIG. 5.4 for the CNTL and moisture-associated experiments described above. Since most experiments have been discussed in the previous chapters, the focus here will be put on the RHInsrt and its relative performance in comparison with others.

On the prediction of horizontal winds (FIG. 5.4a), the instant error growth as shown in the TrueQv resulted from the perfect initial q_v field is also seen in the RHInsrt.

Similar to its impact on the TrueQv, this error growth also causes the RHInsrt to show a forecast error larger than the CNTL at the very beginning of the forecast. However, the length of the impact for the RHInsrt is shorten to the first 30 minutes only, after which the RHInsrt even has its forecast error dropping below the TrueQv for about an hour (between 3:00 and 4:00 UTC). As the impact of the q_v features at the fine scales on inducing the very short range forecast error growth has been established through the previous experiment sets, the shortened error growth period of the RHInsrt, as compared to the Qv, could be most likely attributed to the limited area of the improved q_v field. Besides, the additional information of the hydrometeor fields in the RHInsrt's IC could also be responsible for the very-short-term outperformance over the TrueQv. Eventually after a longer forecast range (2.5 hours, specifically), the above factors start to have their effect diminished as the initial q_v accuracy brings back its domination and the TrueQv significantly outperforms the RHInsrt as a result. While comparing with other two cloud analysis experiments (SatAdj and NoAdj), the RHInsrt generally performs better at most times.

On the prediction of vertical velocity (FIG. 5.4b), the RHInsrt performs better than the TrueQv (the one with the perfect initial q_v) but worse than the NoAdj (the one with the background q_v and hydrometeor analysis) in the first 1.5 hours. The instant impact of the fine scaled initial q_v field at the very beginning as described earlier for the horizontal winds is again confirmed by the relative position of the *w* prediction performances among the experiments. Beginning from 4:30 UTC, the RHInsrt turns to give the second best *w* prediction, which is only worse than that of the TrueQv.

On the prediction of T (FIG. 5.4c), the RHInsrt maintains a trend of forecast error evolution very similar to the TrueQv. Overall, at most times, the RHInsrt outperforms all other experiments except for the TrueQv. However, the RHInsrt performs slightly worse than the CNTL at 2:30 UTC. Given the differences in their ICs, the disadvantaged performance of the RHInsrt implies the strict criticality of the accuracy of the q_v field corresponding to the present hydrometeors on avoiding the instant imbalance on the forecast T.

An overall improvement on q_v analysis (~10%) given by the RHInsrt is demonstrated again as shown at the initial time in FIG. 5.4d. A very short term instant forecast error growth that causes the performance worse than the CNTL as occurring in the TrueQv also happens to the RHInsrt within the first hour of the forecast range. Besides, similar to the V_h prediction, the RHInsrt at first outperforms the TrueQv between 3:00 and 3:30 UTC, and then gets surpassed by the TrueQv after 4:00 UTC. Overall, the RHInsrt provides the best q_v forecasts among all cloud analysis experiments throughout the entire four hours range.

Relatively insignificant forecast error differences are shown among the experiments on the total water prediction (FIG. 5.4e). Overall, the RHInsrt shows forecast errors larger than both the TrueQv and NoAdj within the first hour, and then outperforms the TrueQv with relatively significant error difference after 4:00 UTC while shows indistinctive errors to the NoAdj.

On the overall performance of the state variable predictions given by the ASRMS error (FIG. 5.4f), the instant error growth as seen on most state variables discussed above is shown for the RHInsrt at 2:30 UTC. However, owing to the localized

(in-cloud regions only) improvement of the q_v accuracy and the benefit of initial hydrometeor analysis, the RHInsrt is able to outperform the TrueQv for a very short period (from 3:00 to 3:30 UTC). After 4:00 UTC, the TrueQv returns to provide forecasts significantly better than the RHInsrt (also the best among all) as the critical initial q_v accuracy regains its dominant impact. As a conclusion, the optimally specified in-cloud RH field (i.e., RHInsrt) is capable of providing significantly improved forecasts over either the CNTL or any other cloud analysis experiments which are conducted either with or without the current q_v adjustment.

In both the previous chapter and here, it is found the significantly great q_v analysis errors resulted from the simple saturation moisture adjustment can lead to instant great forecast error growth on most state variables. Further exploration of the 30 minutes forecast errors is proposed by looking into their vertical distribution (FIG. 5.5).

On the predictions of θ and q_v (FIG. 5.5b and 5.5c, respectively), the significant error growth of the SatAdj mainly occurs within the cloudy layers, where the q_v adjustment is in effect, indicating the close linkage between the initial moisture field and the immediate forecasts of the thermodynamic states. On the contrary, the localized moisture adjustment of the SatAdj results in significant forecast errors of horizontal winds (u in FIG. 5.5a and v not shown here) vertically spreading over the entire model layer, suggesting the high and quick sensitivity of the V_h forecast to the initial q_v field. On the q_w prediction (FIG. 5.5d), besides the errors within the cloudy layers, another significant error is found at the level 30 and above in the SatAdj. Furthermore, tight interaction among the V_h, θ, and q_w can be inferred given the relatively similar vertical location of the significant error they share. We would like to point out the significant

better q_v forecast (i.e., less error) near the surface extending up to the cloud base given by the experiment TrueQv. This advantage over other experiments is contributed by the perfect q_v insertion at the cloud-free low levels, where the q_v improvement is not achievable in practice owing to the in-cloud regions limitation.

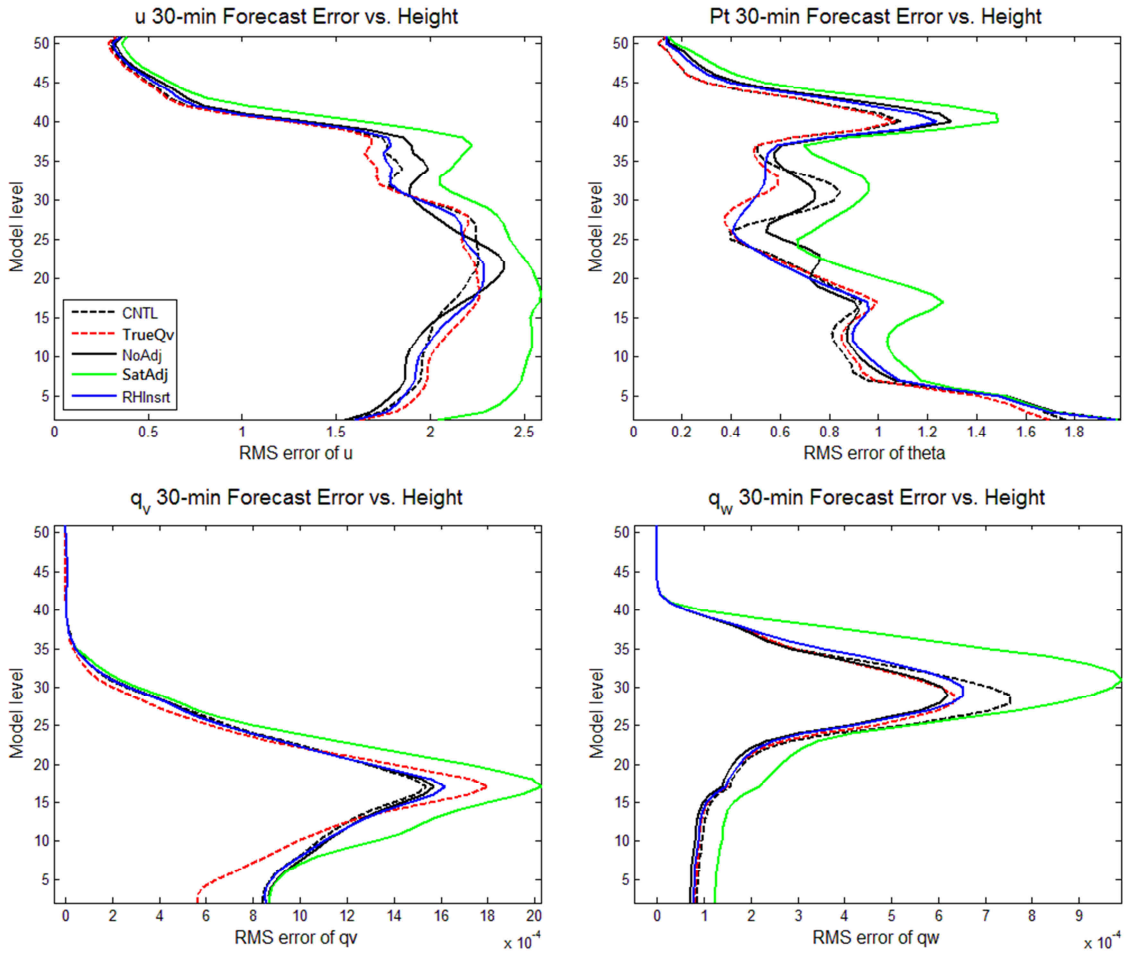

FIG. 5.5 RMS error of (a) u, (b) θ, (c) q_v, and (d) q_w as a function of height (in terms of model level) at 30-min forecast (2:30 UTC). Experiments with and without hydrometeor analysis are represented by solid and dash lines, respectively.

In FIG. 5.6, the verification of reflectivity prediction by the CNTL and q_v-associated experiment set is shown. In terms of the forecast dissimilarity from the truth (FIG. 5.6a), the RHInsrt is able to provide forecasts significantly better than the SatAdj for the entire four hours forecast range. Specifically, after the one hour spin-up period

required for the TrueQv to develop a decent storm structure and provide the significantly best performance, the RHInsrt continuously keeps its second best performance. While comparing with the NoAdj, the additional application of this optimally modified q_v adjustment also shows positive impact ensured by the relatively better forecasts it provides. On predicting the intense convection, the RHInsrt results in a slightly larger underforecast, in terms of the lower bias score (FIG. 5.6b), compared to the TrueQv; however, its significant advantage over the NoAdj is still valid. Furthermore, according to the ETS (FIG. 5.6c), the RHInsrt generally provides forecasts systematically better than the SatAdj (only with a minor exception occurring at 4:00 UTC) throughout the four hours range. After two and a half hours of the forecasts (beginning at 4:30 UTC), the performance of the RHInsrt appears to be quite competitive with that given by the TrueQv, the best forecast. As a conclusion, based on our examination results presented above, the effectiveness of the optimally specified in-cloud RH field is demonstrated by its significant positive impact on the storm prediction.

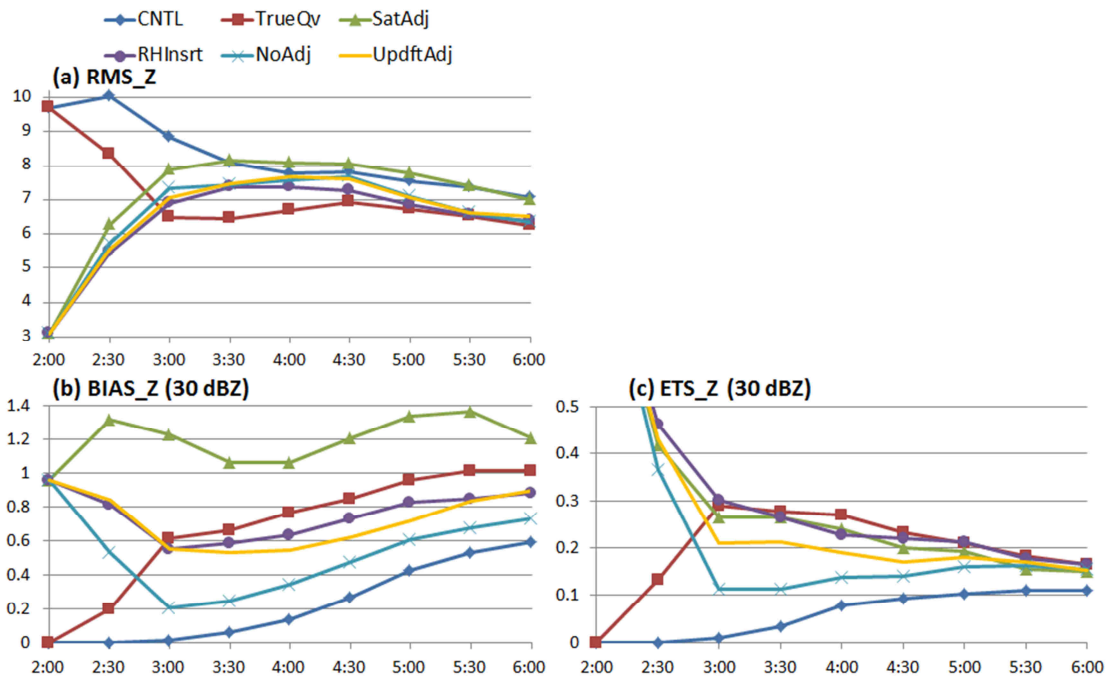

FIG. 5.6 Same as FIG. 3.7, but for the CNTL, TrueQv, NoAdj, SatAdj, RHInsrt, and UpdftAdj.

5.2 A Modified Moisture Adjustment and its Impact

As demonstrated in the previous section that the storm prediction can be significantly improved through an accurately specified initial RH field within the cloudy regions, even if there exist minor analysis errors. Further efforts are made, in this section, to propose an improved q_v adjustment procedure, from which better forecasts are expected.

Since there is no easy relationship existing between in-cloud moisture and available observations, some empirical rules are needed to help improve the in-cloud moisture adjustment. In the previous section, the in-cloud RH field from the truth simulation is shown to have certain unsaturated regions, which is found mostly corresponding with the downdrafts as it has been widely observed in the real atmosphere. In FIG. 5.7, the true RH field is provided again, along with the contour of

true w equal to -0.2 m s^{-1}, which is arbitrarily selected for representing the general areas of the downward motion. It is seen that the occurrence of the unsaturation, especially that under the FL, generally coincides well with the downward motion areas. The capability of our presumed perfect model, used for conducting the truth simulation, on depicting the real observed phenomenon is thus assured.

Based on the investigation of the truth simulation shown above, the usefulness of vertical velocity (w) on helping determine in-cloud moisture is considered. Here in our OSSE framework, we introduce the w information, borrowed from the truth, to develop a modified q_v adjustment. The impact of this modified procedure on the forecasts will also be examined and discussed. Given the ability of the 3DVAR approach on providing accurate wind analysis as demonstrated in a number of present studies (Gao et al. 1999; Potvin et al. 2012), the potential of this newly proposed procedure on real case application, at least in terms of its easy applicability, is assured.

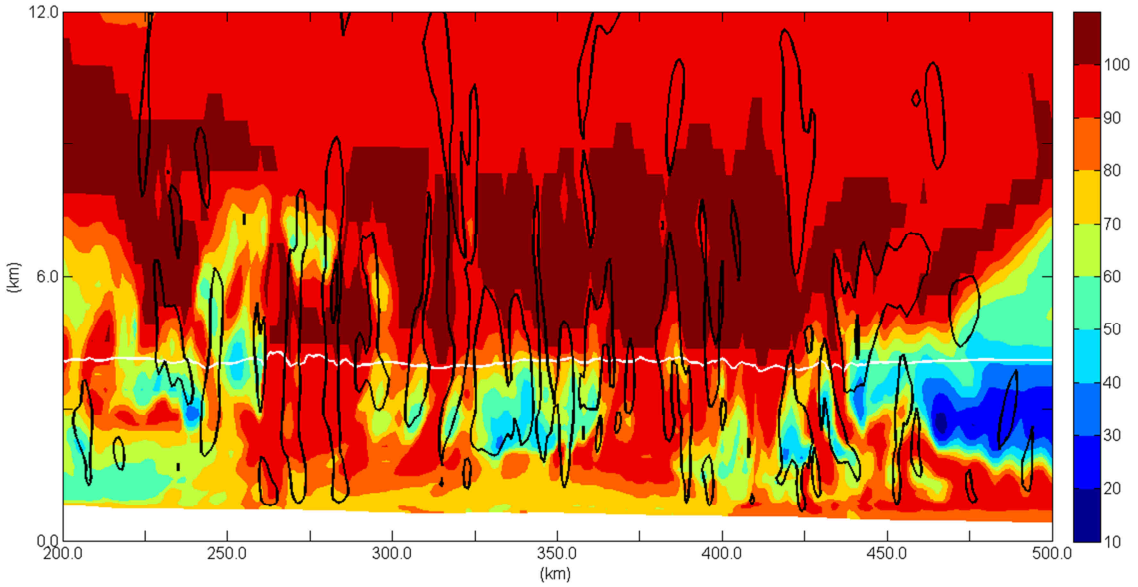

FIG. 5.7 Same as FIG. 5.1a, but with black contours of true w = -0.2 m/s overlaid.

5.2.1 Development of a Vertical Motion Based Moisture Adjustment

Our goal is to find the potential relationship existing between the true RH and *w*, with which the moisture field can be adjusted more accurately and hopefully the improved forecasts can be obtained. Considering the in-cloud RH field shows significantly different features in above-the-FL and under-the-FL regions, our retrieval of the truth-based RH-*w* relation is performed separately for the two regions divided by the 0 °C isotherm as follows:

(i) Regions above the FL (T < 0 °C):

It has been seen in the truth simulation (FIG. 5.3a and b) that most in-cloud regions above the FL are saturated or nearly-saturated (i.e. with RH ≥ 90%). Besides, the water vapor content (i.e., q_v) appears to be relatively low (in this case, no larger than 7.5 g kg^{-1}) primarily owing to the attraction of gravity. Therefore, a relatively simple strategy is sought for performing the q_v adjustment in these regions.

A binary-classified strategy is applied, under which a constant RH value will be assigned over the sub-saturated regions, which is based on the setting of a *w* threshold. There are two central questions that need to be answered before the adjusting procedure can be practically realized:

1) What specific *w* value, which will serve as a bottom threshold, would be representative enough to cover most unsaturated regions?
2) In those unsaturated regions, what constant RH value, which can best match the true state, should be used?

Table 5.1 Contingency table used for statistics above the FL

	w < threshold	w ≥ threshold
RH = 100%	Miss 1	Hit 1
RH < 100%	Hit 2	Miss 2

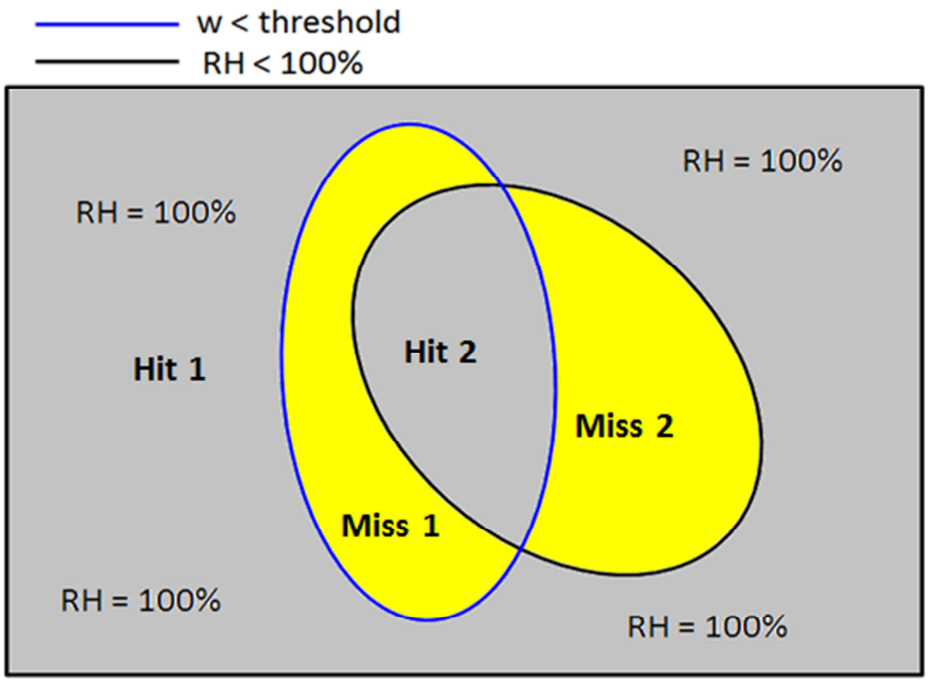

FIG. 5.8 Diagram of w and RH fields used for statistics above the FL. Area within the blue and black ellipses denotes w < threshold and RH < 100%, respectively. Hits and misses corresponding to the contingency table test (Table 5.1) are shaded in gray and yellow color, respectively.

To answer the first question, we perform the statistics of w and its corresponding RH values using a contingency table (as shown in Table 5.1). The population (or sample) used for our statistics are the model grids with the true values that match the following conditions: 1) $T < 0$ °C for ensuring above the FL, and 2) $Z \geq 15$ dBZ for ensuring within the cloudy regions. FIG. 5.8 is provided for the illustration of a sample of w and

RH distribution that used for carrying out our statistics. By varying the *w* threshold, we calculate every resulting hit-miss ratio (HMR) as:

$$\mathrm{HMR} = \frac{\mathrm{Hit\ 1\ +\ Hit\ 2}}{\mathrm{Miss\ 1\ +\ Miss\ 2}}.$$

The best *w* value is then determined by the preset *w* threshold which results in the largest HMR. The *w* threshold is chosen given that it is capable of covering most unsaturated areas and avoiding most saturated areas.

The statistics results (in terms of HMR) of varying w thresholds are plotted and shown as FIG. 5.9. The *w* values ranging from -5 m s^{-1} to 5 m s^{-1} are tested in an every 1 m s^{-1} interval. However, within the range between -0.5 m s^{-1} and 0.5 m s^{-1} where the HMR maximum is approached, the HMR are calculated in a finer interval of 0.1 m s^{-1}. As a result, *w* of 0 m s^{-1} is found to be the best threshold that gives the largest HMR (~3.75), suggesting that the negative w values outline most unsaturated in-cloud regions above the FL.

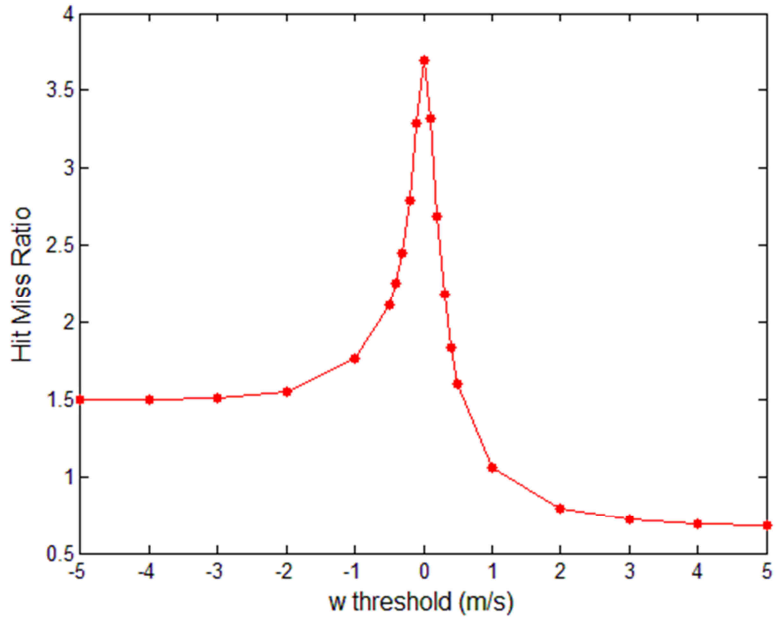

FIG. 5.9 HMR as a function of varying *w* threshold.

After the *w* threshold considered most representative of the unsaturated areas is found, we further look for an arbitrary RH value to assign for these areas. The criterion for determining what RH value should be used is based on the calculation of the q_v analysis error: a minimized RMS error of the final q_v analysis is searched through the varying RH value. Specifically, while 100% RH is kept for all positive *w* areas, different constant RH values are tested for best representing the negative *w* areas and the corresponding RMS errors are calculated. FIG. 5.10 shows q_v analysis results in terms of the SRMS error varying with different RH specified, in which the RH values ranging between 80% and 99% are tested in an every 1% interval. As a result, a SRMS error minimum of 0.99718 is found shared by 90% and 91% RH. Note that in our q_v analysis upon which the SRMS error is calculated, only the in-cloud moisture field above the FL is adjusted while the background moisture values are kept for the regions below the FL. By comparing this analysis result with that provided by other previous discussed cloud analysis experiments (as listed in FIG. 5.10), it is shown that this modified above-the-FL q_v adjustment strategy indeed provides an improved q_v analysis result over both the CNTL (i.e., the background) and SatAdj (i.e., the current q_v adjustment). Note that the improvement over the SatAdj is even more significant with a 26% error reduction. However, a relatively larger error provided by this modified q_v adjustment in contrast with that of the RHInsrt can be seen. This discernible disadvantage is mainly due to the unimproved background moisture field below the FL.

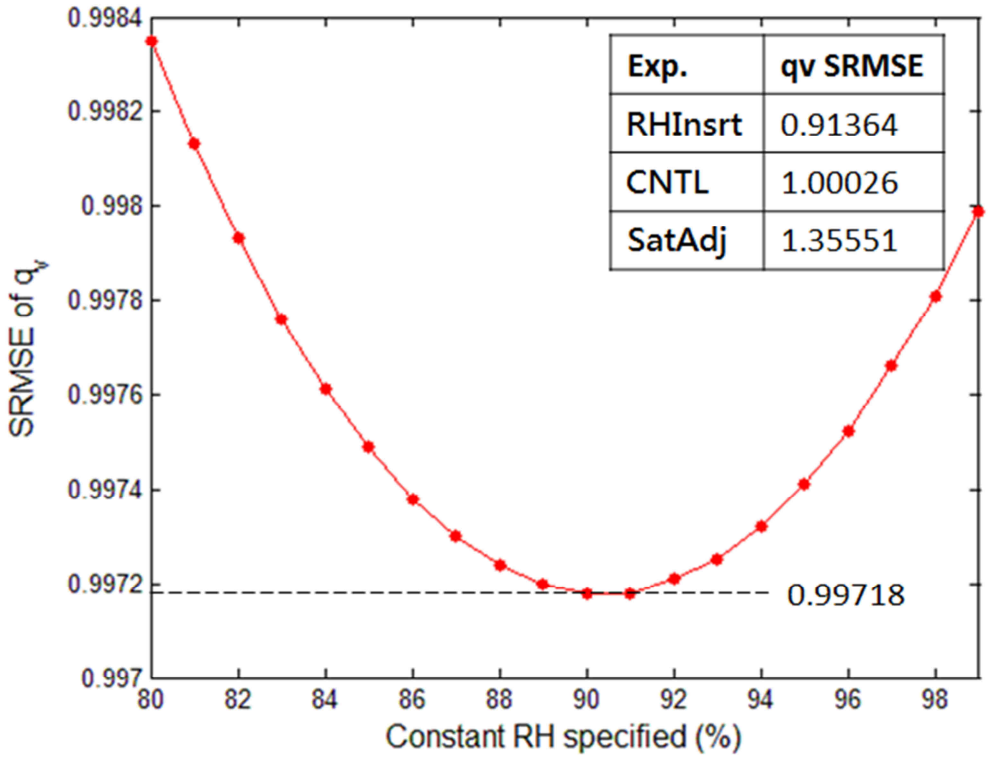

FIG. 5.10 SRMSE of q_v as a function of varying constant RH value specified for negative w areas. For reference purpose, SRMSEs of some other associated experiments are listed at upper right corner of the plot.

(ii) Regions below the FL ($T \geq 0$ °C):

Different from what is seen for the regions above the FL, significantly higher RH variability, both spatially and quantitatively, is found within the in-cloud regions under the FL. Given the presence of the majority of significant (i.e., relatively higher) q_v content, the validity of the q_v adjustment in these regions is thus suggested to be relatively crucial to the subsequent forecasts. To enable a better depiction of the intrinsic complexity of the moisture distribution under the FL, a corresponding complicated adjustment strategy is required.

Again, the relationship between the true *w* and RH is sought for constructing the adjustment strategy. Given the RH variability, the scatter plot and regression are performed. The population for the statistics is confined to the following conditions: 1) $T \geq 0\ ^{\circ}C$ for ensuring below the FL, 2) Z ≥ 15 dBZ for ensuring within cloudy regions, and 3) above the cloud base provided by the cloud coverage analysis procedure (refer to 2.1 for details). In FIG 5.11, the scatter plot of the true *w* and RH is presented. It is seen the overall distribution of the scatters ranges from 10% to 100% for the RH and from -8 m s^{-1} to 10 m s^{-1} for the *w*. Furthermore, a major amount of scatters are found centering around the 0 m s^{-1}. A relatively vague trend of the generally positive proportion between the *w* and RH is found among the scatters.

In order to find a relationship between the *w* and RH that is best representative, in terms of characterizing most scatters and providing resulting analysis of a least error, we perform the regression upon the scatters distributed around the neutral *w* (i.e., 0 m s^{-1}) where most scatters are located. For the regression, a *w* range centering at 0 m s^{-1} with a two-way expansion of 3 m s^{-1} (as denoted by the black dashed lines in FIG. 5.11) is selected given the 99% of the total statistics population it contains. For scatters within this range, first- to third-order polynomial regressions are tested. The results of the regression are shown in FIG. 5.12 denoted by the solid blue lines in addition to the scatters. The fitting equation is also provided in the respective figure. For the scatters outside of the range of the regression, simple constant RH values are assigned given their minority. Generally, these constant RH values are determined by inserting the terminal *w* values (i.e., -3 and 3) into the respective fitting equations. For example, the constant RH values specified for *w* less than -3 m s^{-1} are 57.7%, 47.0%,

and 53.5% in the first-, second-, and third-order regression, respectively (as listed and denoted by the horizontal blue dash lines in FIG. 5.12). However, there are exceptions in the second- and third-order regressions occurring at the positive terminal w value (i.e., 3 m s^{-1}): the RH value derived from corresponding fitting equation appears to decrease with the increasing w after reaching a RH maximum. To avoid the decreasing trend for our adjustment strategy, we truncate the fitting equation around the location where the RH happens. As a result, in the second- (third-) order regression, the constant RH values of 84.8% (84.4%) is specified for regions with w above 2.0 m s^{-1} (1.6 m s^{-1}).

The resulting moisture fields (under the FL) adjusted with these three different order regressions are evaluated with the SRMS error calculation. Again, the background RH values are kept for regions above the FL. The result (as denoted at the bottom left corners in FIG. 5.12) shows that the second- and third-order regressions provide q_v analyses comparable to each other (the second-order is slightly better), while the first-order gives a relatively worse analysis with a discernible larger error. It is also shown that none of these regressions is able to provide quantitatively improved q_v analysis over the CNTL (i.e., the background). The improvement of the overall q_v analysis is limited to 1) the unadjusted regions above the FL, 2) the lack of accuracy of the background T used for the RH-q_v conversion, and most primarily 3) the intrinsic loose relationship existing between the w and RH. Nevertheless, the analyses gained with the regression-based adjustments are still found significantly advantageous over those given by the simple saturation q_v adjustment (i.e., the SatAdj).

Upon the second-order regression (the one giving the least q_v analysis error), further efforts are made to minimize the SRMS error of the q_v analysis. To do so, we

tune the specified constant RH values used at the w boundary of both sides (i.e., w of -3 m s^{-1} and 2 m s^{-1} at the left boundary and right boundary, respectively). With the bottom threshold of w < -3 m s^{-1} and top threshold of $w \geq 2$ m s^{-1} set, the RH values are then tested in an every 1% interval ranging from 40% to 60% for the bottom threshold and from 85% to 99% for the top threshold. For each tuning test, the q_v SRMS error of the corresponding analysis is calculated (detailed results of the examination are omitted here). As a result, it is found when RH of 45% and 85% are specified for the bottom and top threshold, respectively, a SRMS error minimum of 1.02920 can be obtained (FIG. 5.11). The final w-RH relationship used for the q_v adjustment in the regions below the FL is denoted by the blue line shown in FIG. 5.11.

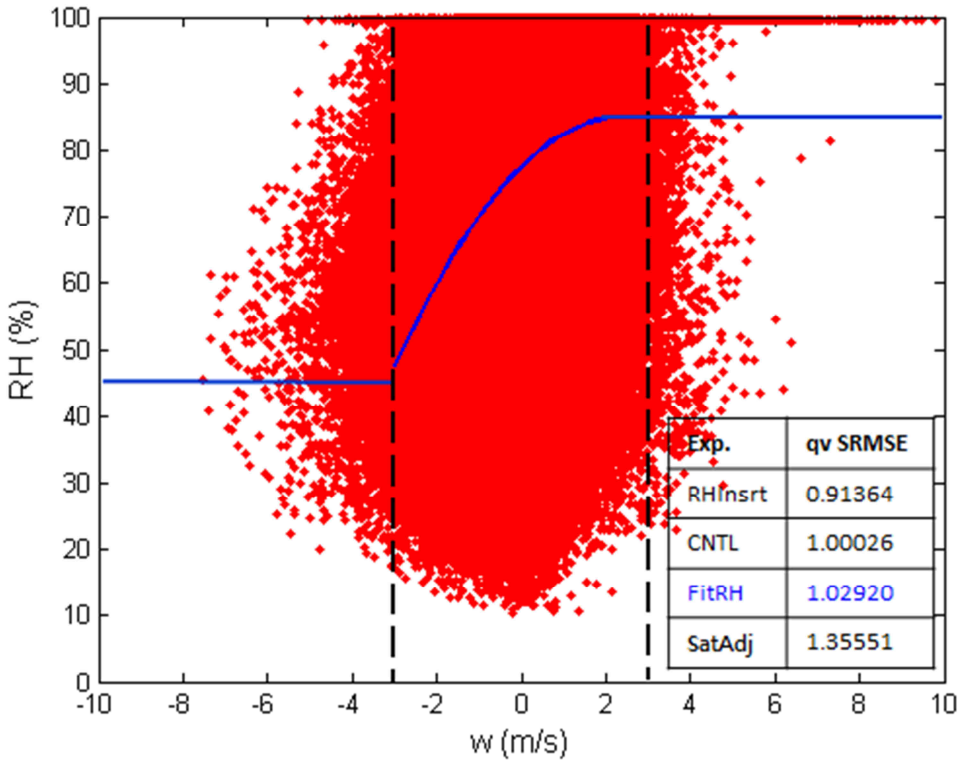

FIG. 5.11 Scatter plot of the true w and RH within the cloudy regions below the FL. Scatters between two black dash lines are used to fit for polynomial relations. Blue curve is the final relation used as the modified q_v adjustment.

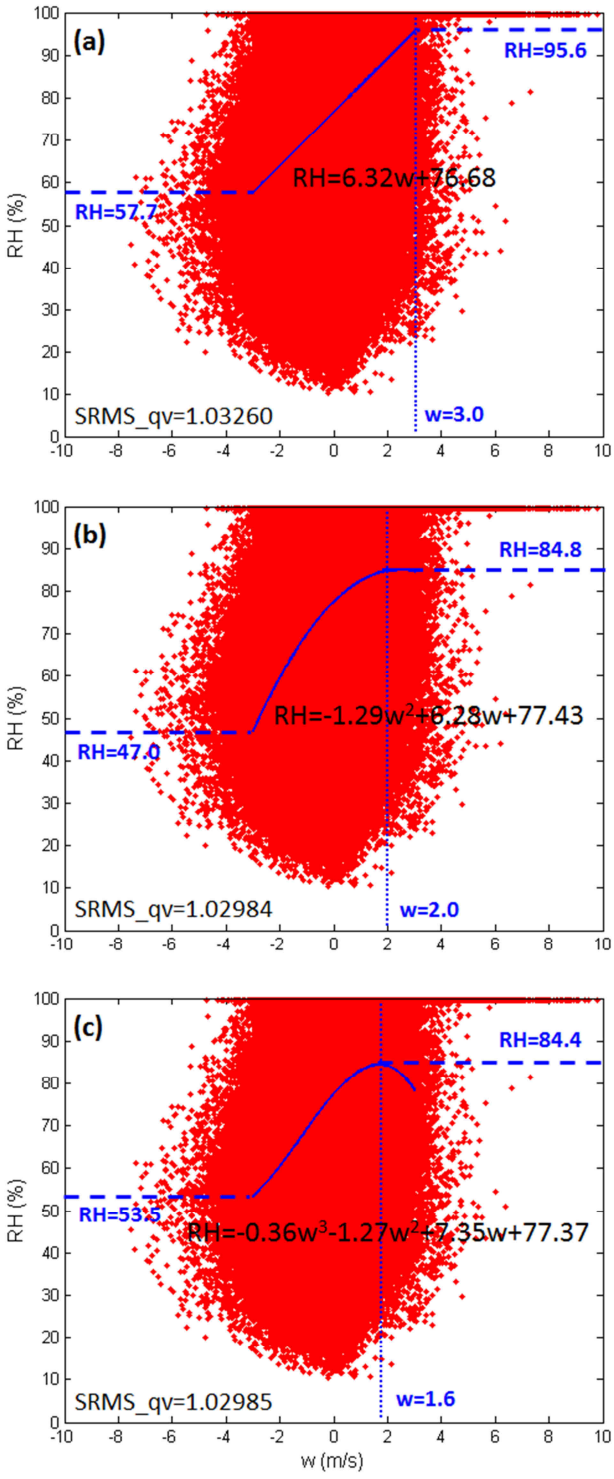

FIG. 5.12 Retrieval of *w*-RH relationship using (a) first order, (b) second order, and (c) third order polynomial regression. Regression results are plotted with blue solid line or curves in the middle of the figures, along with the equations written. Constant RH values used for *w* exceeding terminal thresholds are marked with horizontal dashed blue lines at both sides. SRMS error of q_v analysis using corresponding equation is listed at the bottom left corner of each plot.

With all retrieving processes exhibited above (for both above and below the FL regions), the modified in-cloud q_v adjustment strategy is finalized as:

$$\text{For } T < 0\ ^{\circ}C \text{ (above the FL)}: \begin{cases} w \geq 0 \text{ m s}^{-1}, & \text{RH} = 100\% \\ w < 0 \text{ m s}^{-1}, & \text{RH} = 90\% \end{cases}, and$$

$$\text{for } T \geq 0\ ^{\circ}C \text{ (below the FL)}: \begin{cases} w \geq 2 \text{ m s}^{-1}, & \text{RH} = 85\% \\ -3 \text{ m s}^{-1} \leq w < 2 \text{ m s}^{-1}, & \text{RH} = -1.29w^2 + 6.28w + 77.43 \\ w < -3 \text{ m s}^{-1}, & \text{RH} = 45\% \end{cases}.$$

In practical application of the startegy above, the background temperature is used.

5.2.2 Impact of the Modified Moisture Adjustment

In this subsection, the effectiveness of the *w*-based q_v adjustment is examined through the verification of both the analysis and subsequent forecasts it provides. In FIG. 5.13, the analyzed RH and q_v fields provided by both the current adjustment and modified adjustment are shown for a qualitative comparison.

By comparing with the true RH field (FIG. 5.3a), the significant advantage of the modified q_v adjustment over the current q_v adjustment is shown on providing a RH analysis with spatial variability, which is much more comparable to the truth. However, some extreme values as seen in the truth, particularly those under the FL, are blunted by the *w*-based procedure, resulting in a RH field relatively smoother than its counterpart in the truth. As two significant examples, the low RH values (~40% in light blue) in the area at the horizontal distance between 325 km and 350 km (around 3 km high) is overestimated and the high RH values (above 90% in red) in the area at 375 km is underestimated. On the q_v analysis, significant q_v discontinuity occurring between the cloud edge and its adjacent environmental (i.e., cloud-free) regions is found caused by the current q_v adjustment (FIG. 5.13b), form which the in-cloud q_v field appears to experiences a horizontally homogeneous enhancement given the only information of the

general evenly layered background temperature field used for the q_v retrieval. In contrast with that, the q_v analysis provided by the modified procedure shows relatively smoother q_v changes at the cloud edge. On the other hand, with the additional information of w introduced, the localized updraft/downdraft-induced q_v fluctuations, which is completely absent in the analysis of the simple saturation adjustment, are also characterized by the modified q_v adjustment. Still, some underestimations on the q_v analysis, occurring mostly at low levels around the cloud base, are shown caused by the modified procedure because of the blunted extreme values in the preceding RH analysis as discussed above.

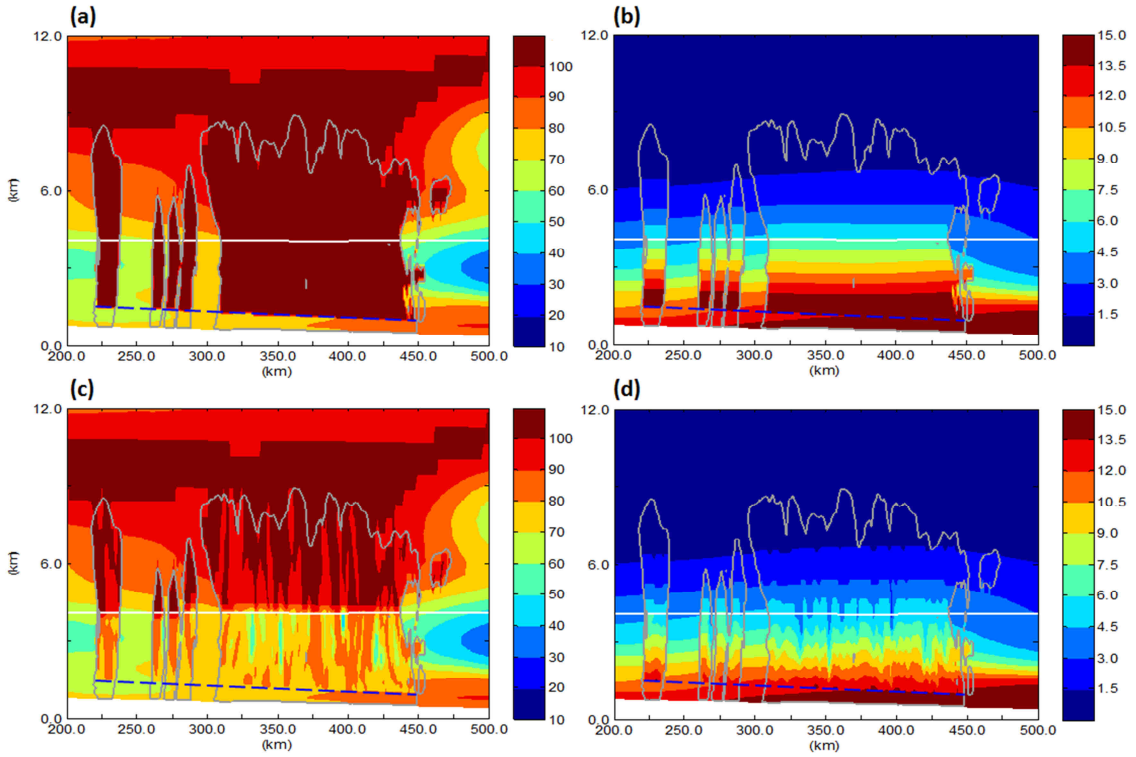

FIG. 5.13 Same as FIG. 5.3, but for the SatAdj (upper panel) and UpdftAdj (lower panel).

In addition to the qualitative improvements on the moisture analysis provided by the modified q_v adjustment as discussed above, the quantitative verification of the

moisture analysis in terms of the SRMS error at the initial condition time (i.e., 2:00 UTC) can be accessed in FIG. 5.4d. Note that the cloud analysis experiment performed with the modified q_v adjustment is named as the UpdftAdj hereafter, given that this *w*-based procedure generally addresses moisture adjustments at the updraft areas instead of making an overall enhancement at both updraft and downdraft areas as done in the current adjustment. Given that the SRMS error of the q_v analysis of the UpdftAdj is 1.026 and the counterpart of the SatAdj is 1.356, the modified moisture adjustment significantly reduces about 24% analysis error of that the simple saturation adjustment has caused, which is inferred mostly by reducing the over-moistening in the downdraft regions. A further examination of the modified adjustment procedure is provided in FIG. 5.2, in which the vertical distribution of the q_v analysis error is shown. Generally, within the layer where the q_v adjustment is in effect, the UpdftAdj appears to have a significantly improved q_v analysis in comparison with the SatAdj (termed as QvAdj in the figure) although a minor error increase is also found to be introduced by the additional application of this modified procedure to the background (i.e., CNTL).

Impact of the modified q_v adjustment on predicting model state variables can be discussed by referring to FIG. 5.4. Given the highest standard of the forecast performance set by the RHInsrt, which utilizes an "optimally" specified moisture field in its IC, we thus expect the performance of the UpdftAdj to be as close to that of the RHInsrt as possible in the following verifications. On the horizontal wind prediction (FIG. 5.4a), the UpdftAdj shares a forecast error trend quite similar to the RHInsrt. Generally, the UpdftAdj performs not as good as the RHInsrt throughout the entire four hour range, and the forecast error difference between them is found to increase with the

forecast range. The systematic outperformance of the RHInsrt over the UpdftAdj highlights the importance of the initial moisture accuracy, specifically in the cloudy regions, on V_h forecasts. Besides, the positive impact of the modified q_v adjustment is also assured by the systematic outperformance of the UpdftAdj over the NoAdj in the entire four hours of the forecast (relatively insignificant within the first hour). On the *w* prediction (FIG. 5.4b), again, the UpdftAdj is found to provide forecast quite competitive with that of the RHInsrt. With the relatively smoother moisture analysis compared to that of the RHInsrt, the Updraft shows relatively smaller *w* forecast error within the first two hours, highlighting the impact of the finer scaled moisture features on inducing the larger *w* forecast error in the very short beginning range.

Similarly, forecast error of the UpdftAdj similar to but slight larger than that of the RHInsrt is found on the *T* prediction (FIG. 5.4c) throughout the entire forecast range. Besides, the slightly worse than the CNTL performance at 2:30 UTC shown in the RHInsrt (as discussed in the previous section) is also found in the UpdftAdj.

On the prediction of q_v (FIG. 5.4d), even beginning with a quantitatively larger analysis error compared to the NoAdj, the UpdftAdj is found to quickly outperform the NoAdj in one hour. The qualitative improvement on the initial q_v field, introduced by the additional information of *w* is attributed to be the key factor of this advantage. In general, the forecast error of the UpdftAdj sticks closely to the RHInsrt for the entire four hours range. However, in the end of the forecast, the UpdftAdj is found slightly outperformed by the SatAdj, which calls for further investigation.

Upon the insignificant diversity of the q_w prediction performance (FIG. 5.4e) among different experiments as discussed earlier, the forecast error of the UpdftAdj is found to nearly overlay on that of the RHInsrt at most times.

The overall performance on the state variable prediction, in terms of the ASRMS error (4.4f), provided by the UpdftAdj is found to stay similar with but slightly worse than that of the RHInsrt. According to the verification results shown above, the *w*-based q_v adjustment is found promising on providing improved forecasts comparable to that achieved by the direct perfect in-cloud RH insertion. Our earlier statement regarding the instant negative impact of the fine scaled q_v feature in the IC occurring at the beginning stage of the *w* prediction is further affirmed here by the relatively better performance of the UpdftAdj compared to that of the RHInsrt.

The verification of *Z* prediction by the UpdftAdj is provided in FIG. 5.6. On the dissimilarity between the truth and the experiment forecast (i.e., the RMS error, FIG. 5.6a), the UpdftAdj performs as good as the RHInsrt within the first 1.5 hours, and then runs into relatively larger error, which is in the magnitude similar to that given by the NoAdj. The later stage divergence of the RMS error shown between the UpdftAdj and RHInsrt can be attributed to their bias score difference occurring at the corresponding time. Most likely, the perfect RH insertion at the initial time is beneficial for the forecast (i.e., RHInsrt) to maintain proper intensity of *Z* by avoiding unfavorable evaporation for a relatively longer range. Nevertheless, the UpdftAdj is still able to distinguish itself from the NoAdj with the great reduced underforecast over the entire forecast range. The ETS of the UpdftAdj (FIG. 5.6c) is significantly better than that of the NoAdj at all times, but is found not that competitive if compared with the SatAdj.

Since the high ETS of the SatAdj is mostly benefited from the unrealistic overforecast of Z as discussed in the previous chapter, we believe the merit of the modified adjustment for improving the Z forecast, mostly through reducing the underforecast, is still valid.

According to the examination presented above, the effectiveness of the modified q_v adjustment procedure based on w and background T has been demonstrated in terms of providing qualitatively improved q_v analysis which is beneficial for both accurate prediction of state variables and properly maintained storm intensity.

Chapter 6: Summary and Future Work

6.1 Summary and Conclusions

Improving the convective-scale storm forecasts in regional NWP models still remains an ongoing challenge, toward which the limitations and potential of the ARPS complex cloud analysis system for radar reflectivity data assimilation has been explored in this dissertation. By using OSSEs in which the truth of all model state variables is known, the accuracy of the analyzed fields can be assessed quantitatively. This study is also valued for its first attempt of using OSSEs to carry out an in-depth investigation into the effectiveness of cloud analysis.

A detailed introduction to the current official version of the ARPS complex cloud analysis system is provided first in this dissertation. With a step-by-step flow chart, key procedures including analysis of precipitating and non-precipitating hydrometers, update of in-cloud temperature and moisture fields, as well as the empirical assumptions involved are reviewed. A new version of the hydrometeor analysis scheme is proposed and implemented in the system. Compared to the official version which simply uses background temperature and observed reflectivity as a guidance to determine one dominant hydrometeor species, the new scheme employs a hydrometeor classification algorithm based on polarimetric radar variables, enabling co-existence of different hydrometeor species that is believed more realistic. In addition to the use of polarimetric radar variables that aid the determination of hydrometeor species, the radar reflectivity operators used in the cloud analysis are also improved. A commonly used option (i.e., the KRY scheme) in the ARPS cloud analysis is based on empirical power-law relationship between the reflectivity and hydrometeor mixing

ratios that were originally derived based on fitting observational data. In the modified version, we use a set of reflectivity operators developed by Jung et al. (2008), which were derived based on scattering by hydrometeors of electromagnetic waves. The operators also include a melting model that enables more accurate calculations of scattering by water-coated wet hail and graupel.

The revised cloud analysis with the above two modifications is applied to a maritime mesoscale convective vortex case in Taiwan region, and the impact of the revised cloud analysis is assessed in terms of rainfall forecast. It is found that even though the differences in the hydrometeor analyses provided by the versions of scheme are significant, the forecast hydrometeor and rainfall become similar just one hour into the forecast. Only small sensitivity to the cloud analysis algorithm differences is found, and for this real case, the rainfall forecast error is significant. Significant model errors as well as errors in the storm environment are believed to be the contributing factors; such errors can quickly overwhelm any improvements to the analyses of in-cloud model states at the initial condition time.

To more unambiguously determine the sensitivity of model forecasts to the cloud analysis procedure and to various treatments within, we shifted our focus in the rest of this dissertation to an OSSE framework where the truth and possible model errors are known. The 19 May 2013 mesoscale convective system over central United States is selected for conducting the OSSE study. A six-hour long free forecast, initialized at 00 UTC, is performed using the ARPS model with a 1-km grid spacing. The initial condition was created by assimilating radar data using the ARPS 3DVAR and cloud analysis on a 4-km grid, using the operational 12-km NAM analysis as the

background. The 1-km spun-up forecast between 2 and 6 hours is used as the truth for the OSSEs. By smoothing the model state variables of the truth forecast at 02 UTC and removing the cloud fields, a degraded initial condition is created. A baseline control forecast is created starting from this degraded initial condition, which will be improved by introducing more accurate initial conditions through sensitivity and data assimilation experiments.

In the first set of the OSSEs, the relative sensitivity to 1) model error due to the use of different microphysics scheme and 2) errors in the initial state variables, is investigated. The forecast winds, temperature (T), moisture (q_v), total water-ice mixing ratio (q_w), and simulated radar reflectivity (Z) of sensitivity experiments are evaluated in terms of the root mean square (RMS) error calculated against the truth. In examining the model error, different microphysics schemes are used in experiments having perfect hydrometeor initial conditions. Compared to the control in which the same microphysics scheme as the truth run is used but with the initial hydrometeors cleared out, the differences due to the model microphysics used appear to be overwhelmed by forecast errors due to IC errors, even though they are limited to non-hydrometeor state variables. However, in terms of the forecast reflectivity field, errors due to microphysics difference become more significant for longer range forecasts.

Subsequently, forecast sensitivity to errors in the IC of individual state variables is examined by alternately inserting perfect values of individual or a group of variables back into the smoothed initial conditions. Among the model state variables that can be updated by the cloud analysis (i.e., potential temperature θ, moisture q_v, and hydrometeor mixing ratio), q_v is found to have the greatest impact on the prediction of

state variables and forecast reflectivity. On the other hand, precipitation hydrometeors are found to have the second largest impact in terms of short-term (two hours and less) prediction of q_w and associated T, which are most likely helped by more accurate hydrometeor and cold pool predictions. Lastly, the importance of the non-precipitating hydrometeors is relatively small. Generally consistent findings about the relative importance among different model state variables are found in Ge et. al (2013).

The second part of the OSSE study is designed to examine the impact and effectiveness of the cloud analysis scheme. Differing from the direct insertion of perfect values that is done in the previous set of experiments, hydrometeor and associated in-cloud state variables in the initial condition are obtained using the ARPS cloud analysis scheme with varying configurations. In addition to the hydrometeor analysis, impact of adjustment of two in-cloud state variables (temperature and moisture) is also examined. When the hydrometeor analysis is performed alone without updating any other in-cloud state variables, noticeable and long lasting, up to four hours, positive impact on forecast can be found in comparison with the hydrometeor-clear control. However, it is found whenever the current q_v adjustment, which saturates the entire precipitation region by setting 100% relative humidity (RH), is applied, rapid forecast error growth occurs in most state variables and reflectivity is significantly over-forecasted. Same issue has also been reported in Schenkman (2012) when frequent cycling analysis strategy was used. On the other hand, when the q_v adjustment is off, the in-cloud temperature adjustment itself, which adjusts the temperature profile towards the moist-adiabat of a low-level lifted parcel, is found to work quite well in terms of giving consistently improved forecast in both state variables and reflectivity over the four-hour forecast range.

Based on the results of the earlier OSSEs, efforts are made in the last part of the dissertation to improve the q_v adjustment procedure in the current cloud analysis to mitigate precipitation overforecast. Firstly, we conduct an experiment by directly inserting the perfect relative humidity values from the truth in the precipitation region to document the impact of in-cloud moisture analysis. The water vapor mixing ratio field is then derived from the perfect RH and error-containing temperature filed. The positive impact of this in-cloud humidity field is demonstrated by its improved forecasts in comparison with those using simple saturation q_v adjustment. Furthermore, a modified q_v adjustment procedure making use of the vertical velocity information is proposed. Based on the observed physics of the "unsaturated downdraft" driven by the evaporation of falling rain, the potential relationship between the vertical velocity and RH is examined. It is found according to our simulation results, this newly-proposed procedure is able to significantly reduce over-moistening in the downdraft regions. However, because of the loose relationship between vertical velocity and relative humidity, the overall analysis error in the adjusted q_v is not necessarily reduced quantitatively. Still, the improved state variable forecast resulting from the modified q_v adjustment over that from the original scheme remains significant throughout the entire four hours range. In terms of predicting intense convection, the superiority of the modified q_v adjustment still holds compared to the experiment with no in-cloud q_v adjustment; however, with this scheme there is under-prediction of precipitation. Further research on further improvement to the q_v adjustment procedure is therefore still warranted.

6.2 Future Work

Given that our findings in this study are primarily based on one-time application of the cloud analysis within the OSSE framework, it is of our interest to explore how their validity will maintain for a real case study in the following two aspects:

1) Inclusion of the 3DVAR wind analysis:

In this study, the impacts of only those variables adjusted in the cloud analysis were examined (i.e., θ, q_v, and q_x, specifically). The 3DVAR wind analysis, however, is often applied along with the cloud analysis for a greater positive impact (as pointed in Hu et al. 2006a; Hu et al. 2006b; Zhao and Xue 2009a). As it was stated in Ge et al. (2013) that among all the state variables they examined, V_h had the greatest impact in terms of accurately constructing the storm structure, the relative importance of the cloud analysis updated variables after the inclusion of the wind analysis can call for further studies.

2) Intermittent application:

As proposed in Schenkman (2012), for better forecast results the current q_v adjustment should be activated only for the first analysis if a cycled DA procedure is performed. Similarly, upon our preliminary findings about the relative importance of each state variable we have examined, further studies can be conducted by applying cycled (i.e., multi-time) analyses, in which combination of different analysis configurations (i.e., adjustment options) can be attempted. Furthermore, the effect of our modified q_v adjustment combined with the current temperature adjustment, which has not been investigated in this dissertation, should also be included in future works.

The modified moisture adjustment we proposed in this study is mainly based on our OSSE framework, in which the true vertical motion (i.e., w) field is greatly relied. Its practical effectiveness on real cases is still required for further exploration. Given the critical role played by the quality and informativeness of the w, the performance of the q_v adjustment based on 3DVAR analysis of radial velocity data from dual (or multiple) radars is planned for examination. On the other hand, more sophisticated empirical relations that make use of additional information could be searched from present studies (either observation based or numerical based) for developing a further improved, or say robust, q_v adjustment. Also with more information involved, the heavy dependence on the w, which relation with moisture is found not completely strict, can be partly alleviated.

References

Albers, S. C., J. A. McGinley, D. A. Birkenheuer, and J. R. Smart, 1996: The local analysis and prediction system (LAPS): Analysis of clouds, precipitation and temperature. *Wea. Forecasting*, **11,** 273-287.

Auligne, T., A. L. Y. Michel, T. Montmerle, and A. J. M. H. J. Dudhia, 2011: Toward a new cloud analysis and prediction system. *B Am Meteorol Soc*, **92,** 207-210.

Benjamin, S. G., and Coauthors, 2004: An hourly assimilation–forecast cycle: The RUC. *Mon. Wea. Rev.*, **132,** 495-518.

Betts, A. K., and M. F. S. Dias, 1979: Unsaturated downdraft thermodynamics in cumulonimbus. *J. Atmos. Sci.*, **36,** 1061-1071.

Brewster, K., 1996: Application of a Bratseth analysis scheme including Doppler radar data. *Preprints, 15th Conf. Wea. Anal. Forecasting*, Norfolk, VA, Amer. Meteor. Soc., 92-95.

——, 2002: Recent advances in the diabatic initialization of a non-hydrostatic numerical model. *Preprints, 15th Conf Num. Wea. Pred./ 21st Conf Severe Local Storms*, San Antonio, TX, Amer. Meteor. Soc., J6.3.

Bringi, V. N., and V. Chandrasekar, 2001: *Polarimetric Doppler Weather Radar: Principles and Applications.* Cambridge, 636 pp.

Byers, H. R., and R. R. Braham, 1949: The Thunderstorm: Report of the Thunderstorm Project, 287 pp.

Chen, G. T.-J., and C.-P. Chang, 1980: The structure and vorticity budgetof an early summer monsoon trough (mei-yu) over southeastern China and Japn. *Mon. Wea. Rev.*, **108,** 942-953.

Crum, T. D., and R. L. Alberty, 1993: The WSR-88D and the WSR-88D operational support facility. *Bull. Amer. Meteor. Soc.*, **74,** 1669-1687.

Dawson, D., 2009: Impacts of Single- and Multi-moment Microphysics on Numerical Simulations of Supercells and Tornadoes of the 3 May 1999 Oklahoma Tornado Outbreak. Ph.D. Dissertation, School of Meteorology, University of Oklahoma, 173 pp.

Dawson, D. T., II, and M. Xue, 2006: Numerical forecasts of the 15-16 June 2002 Southern Plains severe MCS: Impact of mesoscale data and cloud analysis. *Mon. Wea. Rev.*, **134,** 1607-1629.

Dawson, D. T., II, M. Xue, J. A. Milbrandt, and M. K. Yau, 2010: Comparison of evaporation and cold pool development between single-moment and multi-moment bulk microphysics schemes in idealized simulations of tornadic thunderstorms. *Mon. Wea. Rev.*, **138,** 1152-1171.

Dennis, A. S., S. P. Smith Jr., and G. A. P. M. Peterson, R. D. , 1971: Hailstone size distributions and equivalent radar reflectivity factors computed from hailstone momentum records. *J. Appl. Meteor.*, **10,** 79-85.

Droegemeier, K. K., S. M. Lazarus, and R. P. Davies-Jones, 1993: The influence of helicity on numerically simulated convective storms. *Mon. Wea. Rev.*, **121,** 2005-2029.

Emanuel, K. A., 1981: A similarity theory for unsaturated downdrafts within clouds. . *J. Atmos. Sci.*, **38,** 1541-1557.

Evensen, G., 1994: Sequential data assimilation with a nonlinear quasi-geostrophic model using Monte Carlo methods to forecast error statistics. *J. Geophys. Res.*, **99,** 10143-10162.

Federer, B., and A. Waldvogel, 1975: Hail and raindrop size distributions from a Swiss multicell storm. *J. Appl. Meteor.*, **14,** 91-97.

Ferrier, B. S., W.-K. Tao, and J. Simpson, 1995: A double-moment multiple-phase four-class bulk ice scheme. Part II: Simulations of convective storms in different large-scale environments and comparisons with other bulk parameterizations. *J. Atmos. Sci.*, **52,** 1001-1033.

Gao, J.-D., M. Xue, A. Shapiro, and K. K. Droegemeier, 1999: A variational method for the analysis of three-dimensional wind fields from two Doppler radars. *Mon. Wea. Rev.*, **127,** 2128-2142.

Gao, J., M. Xue, K. Brewster, and K. K. Droegemeier, 2004: A three-dimensional variational data analysis method with recursive filter for Doppler radars. *J. Atmos. Oceanic Tech.*, **21,** 457-469.

Gao, J., M. Xue, K. Brewster, F. Carr, and K. K. Droegemeier, 2002: New developmentof a 3DVAR system for a nonhydrostatic NWP model. *15th Conf. on Numerical Weather Prediction/19th Conf. on Weather Analysis and Forecasting*, San Antonio, TX, Amer. Meteor. Soc., 339-341.

Ge, G., J. Gao, and M. Xue, 2013: Impacts of Assimilating Measurements of Different State Variables with a Simulated Supercell Storm and Three-Dimensional Variational Method. *Mon. Wea. Rev.*, **141,** 2759-2777.

Goff, J. A., and S. Gratch, 1946: Low-pressure properties of water from -160 to 212. . *Transactions of the American Society of Heating and Ventilating Engineers: 52nd Annual Meeting of the American Society of Heating and Ventilating Engineers*, ASHVE, 95-122.

Golding, B. W., 1998: Nimrod: A system for generating automated very short range forecasts. *Meterorol. Appl.*, **5,** 1-16.

Haines, P. A., J. K. Luers, and C. A. Cerbus, 1989: The role of the Smith-Feddes model in improving the forecasting of aircraft icing. *Third Conf. on the Aviation Weather System*, Anaheim, CA, Amer. Meteor. Soc., 258-263.

Hamill, T. M., and C. Snyder, 2000: A hybrid ensemble Kalman filter - 3D variational analysis scheme. *Mon. Wea. Rev.*, **128,** 2905-2919.

Heinselman, P. L., and A. V. Ryzhkov, 2006: Validation of polarimetric hail detection. *Wea. Forecasting*, **21,** 839-850.

Hohenegger, C., and C. Schar, 2007: Atmospheric predictability at synoptic versus cloud-resolving scales. *B Am Meteorol Soc*, **88,** 1783-1793.

Houtekamer, P. L., and H. L. Mitchell, 1998: Data assimilation using an ensemble Kalman filter technique. *Mon. Wea. Rev.*, **126,** 796-811.

Hu, M., and M. Xue, 2007: Impact of configurations of rapid intermittent assimilation of WSR-88D radar data for the 8 May 2003 Oklahoma City tornadic thunderstorm case. *Mon. Wea. Rev.*, **135,** 507–525.

Hu, M., M. Xue, and K. Brewster, 2006a: 3DVAR and cloud analysis with WSR-88D level-II data for the prediction of Fort Worth tornadic thunderstorms. Part I: Cloud analysis and its impact. *Mon. Wea. Rev.*, **134,** 675-698.

Hu, M., M. Xue, J. Gao, and K. Brewster, 2006b: 3DVAR and cloud analysis with WSR-88D level-II data for the prediction of Fort Worth tornadic thunderstorms. Part II: Impact of radial velocity analysis via 3DVAR. *Mon. Wea. Rev.*, **134,** 699-721.

Huang, X.-Y., and P. Lynch, 1993: Diabatic digital-filtering initialization: Application to the HIRLAM model. *Mon. Wea. Rev.*, **121,** 589-603.

Hubbert, J. C., M. Dixon, S. M. Ellis, and G. Meymaris, 2009: Weather radar ground clutter. Part I: Identification, modeling, and simulation. *J. Atmos. Oceanic Technol.*, **26,** 1165-1180.

Johns, R. H., and C. A. Doswell III, 1992: Severe local storm forecasting. *Wea. Forecasting*, **7,** 588-612.

Jones, C. D., and B. Macpherson, 1997: A latent heat nudging scheme for the assimilation of precipitation data into an operational mesoscale model. *Meteor. Appl.*, **4,** 269-277.

Jou, B. J.-D., W.-C. Lee, and R. H. Johnson, 2010: An overview of SoWMEX/TiMREX. *Selected Papers of the Fourth International Monsoon Workshop*, C. P. Chang, Ed., World Scientific, 1-16.

Jung, Y., G. Zhang, and M. Xue, 2008: Assimilation of simulated polarimetric radar data for a convective storm using ensemble Kalman filter. Part I: Observation operators for reflectivity and polarimetric variables. *Mon. Wea. Rev.*, **136,** 2228-2245.

Jung, Y., M. Xue, and M. Tong, 2010: Ensemble Kalman filter assimilation of radar data for a convecive storm using a two-moment microphysics scheme. *4th EnKF Workshop*, Albany, NY, http://hfip.psu.edu/EDA2010.

——, 2012: Ensemble Kalman filter analyses of the 29-30 May 2004 Oklahoma tornadic thunderstorm using one- and two-moment bulk microphysics schemes, with verification against polarimetric data. *Mon. Wea. Rev.*, **140,** 1457-1475.

Kain, J. S., and Coauthors, 2010: Assessing advances in the assimilation of radar data within a collaborative forecasting-research environment. *Wea. Forecasting*, **25,** 1510-1521.

Kessler, E. I., 1969: *On the distribution and continuity of water substance in atmospheric circulations.* Amer. Meteor. Soc., 84 pp.

Kim, D., S. G. Benjamin, and J. M. Brown, 2002: Cloud/hydrometeor initialization in the 20-km RUC using radar and GOES data. . *Preprints, 15th Conf. on Numerical Weather Prediction*, Amer. Meteor. Soc., 335-338.

Knight, C. A., W. A. Cooper, D. W. Breed, I. R. Paluch, P. L. Smith, and G. Vali, 1982: *Hailstorms of the central high plains.* Vol. 1.

Lai, H.-W., C. A. Davis, and B. J.-D. Jou, 2011: A subtropical oceanic mesoscale convective vortex observed during SoWMEX/TiMREX. *Mon. Wea. Rev.*, **139,** 2367-2385.

Leary, C. A., 1980: Temperature and humidity profiles in mesoscale unsaturated downdrafts. *J. Atmos. Sci.*, **37,** 1005-1012.

Lewis, J. M., and J. C. Derber, 1985: The use of adjoint equations for analysis and assimilation of meteorological observations: Theoretical aspects. *Tellus*, **37A,** 309-322.

Lilly, D. K., 1990: Numerical prediction of thunderstorms - Has its time come? *Quart. J. Roy. Meteor. Soc.*, **116,** 779-798.

Lin, Y.-L., R. D. Farley, and H. D. Orville, 1983: Bulk parameterization of the snow field in a cloud model. *J. Climat. Appl. Meteor.*, **22,** 1065-1092.

Lin, Y., P. S. Ray, and K. W. Johnson, 1993: Initialization of a modeled convective storm using Doppler radar-derived fields. *Mon. Wea. Rev.*, **121,** 2757-2775.

Lorenz, E. N., 1963: Deterministic nonperiodic flow. *J. Atmos. Sci.*, **20,** 130-141.

Lorenz, E. N., 1995: Predictability - A problem partly solved. *Proc. Seminar on Predictability*, Shinfield Park, Reading, United Kingdom, European Centre for Medium-Range Weather Forecasting, 1-18.

Macpherson, B., B. J. Wright, W. Hand, and A. J. Maycock, 1996: The impact of MOPS moisture data in the UK Meteorological Office mesoscale data assimilation scheme. *Mon. Wea. Rev.*, **124,** 1746-1766.

Milbrandt, J. A., and M. K. Yau, 2005a: A multi-moment bulk microphysics parameterization. Part I: Aanlysis of the role of the spectral shape parameter. *J. Atmos. Sci.*, **62,** 3051-3064.

——, 2005b: A multi-moment bulk microphysics parameterization. Part II: A proposed three-moment closure and scheme description. *J. Atmos. Sci.*, **62,** 3065-3081.

Milbrandt, J. A., and M. K. Yau, 2006: A multimoment bulk microphysics parameterization. Part IV: Sensitivity experiments. *J. Atmos. Sci.*, **63,** 3137-3159.

Park, H., A. V. Ryzhkov, D. S. Zrnic, and K.-E. Kim, 2009: The hydrometeor classification algorithm for the polarimetric WSR-88D: Description and application to an MCS. *Wea. Forecasting*, **24,** 730-748.

Park, S. K., and K. K. Droegemeier, 2000: Sensitivity analysis of a 3D convective storm: Implications for variational data assimilation and forecast error. *Mon. Wea. Rev.*, **128,** 140-159.

Pestaina-Haynes, M., and G. L. Austin, 1976: Comparison between maritime tropical (GATE and Barbados) and continental mid-latitude (Montreal) precipitation lines. *J. Appl. Meteor.*, **15,** 1077-1082.

Phillips, V. T. J., A. Pokrovsky, and A. Khain, 2007: The influence of time-dependent melting on the dynamics and precipitation production in maritime and continental storm clouds. *J. Atmos. Sci.*, **64,** 338-359.

Potvin, C. K., D. Betten, L. J. Wicker, K. L. Elmore, and M. I. Biggerstaff, 2012: 3DVAR versus traditional dual-Doppler wind retrievals of a simulated supercell thunderstorm. . *Mon. Wea. Rev.*, **140,** 3487-3494.

Purser, R. J., and R. McQuiqq, 1982: A successive correction analysis scheme using recursive numerical fileters. Met. O 11 Tech. Note, No. 154, British Meteorological Office, 17 pp.

Putnam, B. J., M. Xue, Y. Jung, N. A. Snook, and G. Zhang, 2014: The analysis and prediction of microphysical states and polarimetric variables in a mesoscale convective system using double-moment microphysics, multi-network radar data, and the ensemble Kalman filter. *Mon. Wea. Rev.*, **142,** 141-162.

Rennie, S. J., S. L. Dance, A. J. Illingworth, S. P. Ballard, and D. Simonin, 2011: 3D-Var assimilation of insect-derived Doppler radar radial winds in convective cases using a high-resolution model. *Mon. Wea. Rev.*, **139,** 1148-1163.

Rogers, R. R., and M. K. Yau, 1989: *A Short Course in Cloud Physics*. 3rd ed. Pergamon Press, 293 pp.

Rosenfeld, D., and I. M. Lensky, 1998: Satellite-based insights into precipitation formation processes in continental and maritime convective clouds. *B Am Meteorol Soc*, **79,** 2457-2476.

Schaefer, J. T., 1990: The critical success index as an indicator of warning skill. *Wea. Forecasting*, **5,** 570-575.

Schenkman, A., M. Xue, A. Shapiro, K. Brewster, and J. Gao, 2011: Impact of CASA radar and Oklahoma mesonet data assimilation on the analysis and prediction of tornadic mesovortices in a MCS. *Mon. Wea. Rev.*, **139,** 3422-3445.

Schenkman, A. D., 2012: Exploring tornadogenesis with high-resolution simulations initialized with real data. Ph. D. Dissertation, School of Meteorology, University of Oklahoma, 186 pp.

Seity, Y. P. B., S. Malardel, G. H. P. Benard, and F. B. C. L. V. Masson, 2011: The AROME-France convective-scale operational model. *Mon. Wea. Rev.*, **139,** 976-991.

Snyder, C., and F. Zhang, 2003: Assimilation of simulated Doppler radar observations with an ensemble Kalman filter. *Mon. Wea. Rev.*, **131,** 1663-1677.

Stensrud, D. J., and Coauthors, 2009: Convective-scale warn-on-forecast system: A vision for 2020. *Bull. Amer. Meteor. Soc.*, **90,** 1487-1499.

Straka, J. M., D. S. Zrnic, and A. V. Ryzhkov, 2000: Bulk hydrometeor classification and quantification using polarimetric radar data: Synthesis of relations. *Journal of Applied Meteorology*, **39,** 1341-1372.

Sun, J., 2005: Initialization and numerical forecasting of a supercell storm observed during STEPS. *Mon. Wea. Rev.*, **133,** 793-813.

Sun, J., and N. A. Crook, 1997: Dynamical and microphysical retrieval from Doppler radar observations using a cloud model and its adjoint. Part I: Model development and simulated data experiments. *J. Atmos. Sci.*, **54,** 1642-1661.

——, 1998: Dynamical and microphysical retrieval from Doppler radar observations using a cloud model and its adjoint. Part II: Retrieval experiments of an observed Florida convective storm. *J. Atmos. Sci.*, **55,** 835-852.

Sun, J., and Coauthors, 2012: Sensitivity of 0–12-h warm-season precipitation forecasts over the central United States to model initialization. *Weather and Forecasting*, **27,** 832-855.

Surcel, M., I. Zawadzki, and M. K. Yau, 2015: A study on the scale dependence of the predictability of precipitation patterns. *J. Atmos. Sci.*, **72,** 216-235.

Tong, M., and M. Xue, 2005: Ensemble Kalman filter assimilation of Doppler radar data with a compressible nonhydrostatic model: OSS Experiments. *Mon. Wea. Rev.*, **133,** 1789-1807.

Tribbia, J. J., and D. P. Baumhefner, 1988: The reliability of improvements in deterministic short-range forecasts in the presence of initial state and modeling deficiencies. *Mon. Wea. Rev.*, **116,** 2276-2288.

Uccellini, L. W., P. J. Kocin, and J. M. Sienkiewicz, 1999: Advances in forecasting extratropical cyclogenesis at the National Meteorological Center. *The lifecycles of extratropical cyclones*, M. A. Shapiro, and S. Gronas, Eds., AMS, 317-336.

Ulbrich, C. W., 1983: Natural variations in the analytical form of the raindrop size distributions. *J. Appl. Meteor.*, **22,** 1764-1775.

Ulbrich, C. W., and D. Atlas, 2007: Microphysics of raindrop size spectra: Tropical continental and maritime storms. *J. Appl. Meteor. Climatology*, **46,** 1777-1791.

Van Weverberg, K., A. M. Vogelmann, H. Morrison, and J. A. Milbrandt, 2011: Sensitivity of idealized squall-line simulations to the level of complexity used in two-moment bulk microphysics schemes. *Mon. Wea. Rev.*, **140,** 1883-1907.

Vasiloff, S. V., and Coauthors, 2007: Improving QPE and Very Short Term QPF: An Initiative for a Community-Wide Integrated Approach. *B Am Meteorol Soc*, **88,** 1899-1911.

Vivekanandan, J., S. M. Ellis, R. Oye, D. S. Zrnic, A. V. Ryzhkov, and J. Straka, 1999: Cloud microphysics retrieval using S-band dual-polarization radar measurements. *B Am Meteorol Soc*, **80,** 381-388.

Wagner, T. J., D. D. Turner, L. K. Berg, and S. K. Krueger, 2013: Ground-based remote retrievals of cumulus entrainment rates. *J. Atmos. Oceanic Technol.*, **30,** 1460-1471.

Wang, H., J. Sun, S. Fan, and X.-Y. Huang, 2013: Indirect assimilation of radar reflectivity with WRF 3D-Var and its impact on prediction of four summertime covective events. *J. Appl. Meteor.*, **52,** 889-902.

Weygandt, S., P. Nutter, E. Kalnay, S. K. Park, and K. K. Droegemeier, 1999: The relative importance of different data fields in a numerically simulated convective storm. . *8th Conf. on Mesoscale Processes*, Boulder, CO, Amer. Meteor. Soc., 310-315.

Weygandt, S. S., A. Shapiro, and K. K. Droegemeier, 2002a: Retrieval of Model Initial Fields from Single-Doppler Observations of a Supercell Thunderstorm. Part I: Single-Doppler Velocity Retrieval. *Mon. Wea. Rev.*, **130,** 433-453.

——, 2002b: Retrieval of model initial fields from single-Doppler observations of a supercell thunderstorm. Part II: Thermodynamic retrieval and numerical prediction. *Mon. Wea. Rev.*, **130,** 454-476.

Weygandt, S. S., S. G. Benjamin, T. G. Smirnova, and J. M. Brown, 2008: Assimilation of radar reflectivity data using a diabatic digital filter within the rapid update cycle. *Preprint, 12th Conf. on IOAS-AOLS*, Ameri. Meteor. Soc.

Wilson, J. W., C. A. Knight, S. A. Tessendorf, and C. Weeks, 2011: Polarimetric radar analysis of raindrop size variability in maritime and continental clouds. *J. Appl. Meteor. Climatology*, **50,** 1970-1980.

Xiao, Q., Y.-H. Kuo, J. Sun, W.-C. Lee, D. M. Barker, and E. Lim, 2007: An approach of radar reflectivity data assimilation and its assessment with the inland QPF of typhoon Rusa (2002) at landfall. *J. Appl. Meteor. Climatology* **46,** 14-22.

Xu, Q., 1996a: Generalized adjoint for physical processes with parameterized discontinuities - Part I: Basic issues and heuristic examples. *J. Atmos. Sci.*, **53,** 1123-1142.

——, 1996b: Generalized adjoint for physical processes with parameterized discontinuities - Part II: Vector formulations and matching conditions. *J. Atmos. Sci.*, **53,** 1143-1155.

Xue, M., K. K. Droegemeier, and V. Wong, 1995: Advanced Regional Prediction System (ARPS) and real-time storm prediction. *Preprint, International workshop on limited-area and variable resolution models*, Beijing, China, World Meteor. Organ.

Xue, M., K. K. Droegemeier, and V. Wong, 2000: The Advanced Regional Prediction System (ARPS) - A multiscale nonhydrostatic atmospheric simulation and prediction tool. Part I: Model dynamics and verification. *Meteor. Atmos. Phy.*, **75,** 161-193.

Xue, M., F. Kong, K. A. Brewster, K. W. Thomas, J. Gao, Y. Wang, and K. K. Droegemeier, 2013: Prediction of convective storms at convection-resolving 1 km resolution over continental United States with radar data assimilation: An example case of 26 May 2008 and precipitation forecasts from spring 2009. *Adv. Meteor.*, **2013,** Article ID 259052, doi:259010.251155/252013/259052.

Xue, M., and Coauthors, 2001: The Advanced Regional Prediction System (ARPS) - A multi-scale nonhydrostatic atmospheric simulation and prediction tool. Part II: Model physics and applications. *Meteor. Atmos. Phys.*, **76,** 143-165.

Xue, M., and Coauthors, 2008: CAPS realtime storm-scale ensemble and high-resolution forecasts as part of the NOAA Hazardous Weather Testbed 2008 Spring Experiment. *24th Conf. Several Local Storms*, Savannah, GA, Ameri. Meteor. Soc., Paper 12.12.

Zhang, G., J. Vivekanandan, and E. Brandes, 2001: A method for estimating rain rate and drop size distribution from polarimetric radar measurements. *IEEE Trans. Geosci. Remote Sens.*, **39,** 830-841.

Zhang, J., 1999: Moisture and Diabatic Initialization Based on Radar and Satellite Observation. Ph.D., School of Meteorology, University of Oklahoma, 194 pp.

Zhang, J., F. Carr, and K. Brewster, 1998: ADAS cloud analysis. *Preprints, 12th Conf. on Num. Wea. Pred.*, Phoenix, AZ., Amer. Met. Soc., 185-188.

Zhao, K., and M. Xue, 2009a: Assimilation of coastal Doppler radar data with the ARPS 3DVAR and cloud analysis for the prediction of Hurricane Ike (2008). *Geophysical Research Letters*, **36**.

Zhao, K., and M. Xue, 2009b: Assimilation of coastal Doppler radar data with the ARPS 3DVAR and cloud analysis for the prediction of Hurricane Ike (2008). *Geophy. Res. Lett.***,** L12803.

Zhao, Q. Y., and Y. Jin, 2008: High-resolution radar data assimilation for hurricane Isabel (2003) at landfall. *Bull. Amer. Meteor. Soc.*, **89,** 1355-1372.

Zrnic, D. S., and A. V. Ryzhkov, 1996: Advantages of rain measurements using specific differential phase. *J. Atmos. Oceanic Technol.*, **13,** 454-464.

Appendix A: Formulation of the Modified Mixing Ratio Analysis Procedure

To obtain the analysis result of mixing ratio for each precipitating species (e.g., rain, snow, graupel, and hail) from a single radar observation value, such as reflectivity, additional information is needed since the problem itself is under-determined. The ratio of q_x (i.e., mixing ratio of species x) among each precipitating species is the perquisite information required for realizing the entire mixing ratio analysis procedure. The complete procedure is provided step by step in details as follows.

A.1 Retrieving the Portions of Mixtures

According to the simple melting model included in Jung et al. (2008a) as they built up the T-matrix method based radar observation operators, radar variables (e.g., Z, Z_{DR}, Z_{dp}, and K_{DP}) are contributed not only by the pure species such like rain, snow, graupel, and hail, but also by their mixing phases (e.g., wet/melting snow, mixed by rain and snow). Therefore, the portion of these mixing species in terms of ratio to other pure (dry) species is also required in advance.

As the mixture is assumed to exist only when rain water (i.e., q_r) coexist with any ice phase species (i.e., q_s, q_g, or q_h), here we take the rain-snow mixture as an example for the demonstration.

In the melting model introduced in Jung et al. (2008a), the fraction of rain-snow mixture F can be determined by

$$F = 0.5[\min(q_s/q_r\,, q_r/q_s)]^{0.3}, \tag{1}$$

where the power of 0.3 is taken for depicting a gradual change of rain and snow amount with height through the melting layer. With this, the total mixing ratio of rain-snow mixture can be calculated as

$$q_{rs} = F(q_r + q_s),$$

(2)

where the subscript *rs* stands for mixture of rain and snow.

According to the equations above, the portion of any mixture can be determined as long as the ratio between the rain water and the corresponding ice spices is known. It is the first step of our procedure to calculate the portions of all present mixtures (i.e., q_{rs}, q_{rg}, and q_{rh}) from the pre-known information, the ratio among all present pure species.

A.2 Extracting the Coefficient in Radar Operator for Rain

From Jung et al. (2008a), the radar reflectivity for rain species is given by

$$Z_r = \frac{4\lambda^4 \alpha_{ra}^2 N_{0r}}{\pi^4 |K_w|^2} \Lambda_r^{-(2\beta_{ra}+1)} \Gamma(2\beta_{ra} + 1),$$

(3)

where λ is the radar wavelength, K_w = 0.93 is the dielectric factor for water, α_{ra} = 4.28 $\times 10^{-4}$ and β_{ra} = 3.04 are factors of backscattering amplitudes from the T-matrix and fitting results (Zhang et al. 2001), N_{0r} and Λ_r are the intercept and slope parameter, respectively, of the drop size distribution (DSD) as introduced in Ulbrich (1983). By introducing the relation

$$\Lambda_r = \left(\frac{\pi \rho_r N_{0r}}{\rho_a q_r}\right)^{0.25}$$

(4)

and inserting constant β_{ra}, equation (3) can be reformed as

$$Z_r = \frac{4\lambda^4 \alpha_{ra}^2 \Gamma(7.08)}{\pi^{5.77} |K_w|^2 {\rho_r}^{1.77} {N_{0r}}^{0.77}} (\rho_a q_r)^{1.77}.$$

(5)

Note that ρ_r and ρ_a are the density of rain water and air, respectively. In equation (5), the N_{0r} is in unit of [km^{-4}] while Z_r is of [mm^3]. For simplicity and convenience in further analysis process, two coefficients are added in generalizing Z_r to the common used linear unit of reflectivity [mm^6 m^{-3}] as

$$Z_r = 10^9 \times \frac{4\lambda^4 \alpha_{ra}^2 \Gamma(7.08) {\rho_a}^{1.77}}{\pi^{5.77} |K_w|^2 \rho_x^{1.77} (10^{-12} \times N_{0r})^{0.77}} {q_r}^{1.77},$$

(6)

in which N_{0r} is in unit of [m^{-4}].

In equation (6), q_r is the only unknown variable. Thus, we extract all other variables ahead and make them a coefficient *r_coef* for our further derivation

$$Z_r = r\_coef \times {q_r}^{1.77},$$

$$r\_coef = 10^9 \times \frac{4\lambda^4 \alpha_{ra}^2 \Gamma(7.08) {\rho_a}^{1.77}}{\pi^{5.77} |K_w|^2 \rho_x^{1.77} (10^{-12} \times N_{0r})^{0.77}}.$$

(7)

A.3 Extracting the Coefficients in Radar Operator for Species Other than Rain

Similarly, we begin with the reflectivity equation from Jung et al. (2008a) for other species *x* (snow, graupel, hail, or any other mixtures)

$$Z_x = \frac{2880\lambda^4 N_{0x}}{\pi^4 |K_w|^2} \Lambda_x^{-7} (A\alpha_{xa}^2 + B\alpha_{xb}^2 + 2C\alpha_{xa}\alpha_{xb}),$$

(8)

where N_{0x} and Λ_x again, are the DSD parameters, but for non-rain species *x*.

α_{xa} and α_{xb} are polynomial fitting results as a function of the water fraction of mixtures $f_w = q_r/(q_r+q_x)$, which can be obtained as the ratios among each species are known at first. The functions are listed below

Rain-snow mixture:

$$\alpha_{rsa} = \left(0.194 + 7.094f_w + 2.135{f_w}^2 - 5.225{f_w}^3\right) \times 10^{-4},$$

$$\alpha_{rsb} = \left(0.191 + 6.916f_w - 2.841{f_w}^2 - 1.160{f_w}^3\right) \times 10^{-4}.$$

Rain-graupel mixture:

$$\alpha_{rga} = \left(0.081 + 2.040f_w - 7.390{f_w}^2 + 18.14{f_w}^3 - 26.02{f_w}^4 + 19.37{f_w}^5 - 5.75{f_w}^6\right) \times 10^{-3},$$

$$\alpha_{rga} = \left(0.076 + 1.740f_w - 7.590{f_w}^2 + 20.22{f_w}^3 - 30.42{f_w}^4 + 23.31{f_w}^5 - 7.06{f_w}^6\right) \times 10^{-3}.$$

Rain-hail mixture:

$$\alpha_{rha} = \left(0.191 + 2.39f_w - 12.57{f_w}^2 + 38.71{f_w}^3 - 65.53{f_w}^4 + 56.16{f_w}^5 - 18.98{f_w}^6\right) \times 10^{-3},$$

$$\alpha_{rha} = \left(0.165 + 1.72f_w - 9.920{f_w}^2 + 32.15{f_w}^3 - 56.00{f_w}^4 + 48.83{f_w}^5 - 16.69{f_w}^6\right) \times 10^{-3}.$$

A, *B*, and *C* are coefficients associated with the falling properties of different ice particles such like canting angle. Refer to Jung et al. (2008a) for more details. Here the constant values used in our study are listed below

Snow and rain-snow mixture:

A = 0.8140, B = 0.0303, and C = 0.0778.

Graupel, rain-graupel mixture, hail, and rain-hail mixture:

A = 0.4308, B = 0.3192, and C = 0.1250.

Reform equation (8) by inserting equation (4) as

$$Z_x = \frac{2880\lambda^4(A\alpha_{xa}^2 + B\alpha_{xb}^2 + 2C\alpha_{xa}\alpha_{xb})\rho_a{}^{1.75}}{\pi^{5.75}|K_w|^2 N_{0x}{}^{0.75}\rho_x{}^{1.75}} q_x{}^{1.75} \,. \tag{9}$$

As the Z_x above is in [mm^6 m^{-3}], we extract all the known variables and constants and make them a coefficient *x_coef*. The equation (9) then is rewritten as

$$Z_x = x\_coef \times q_x{}^{1.75} \,, \tag{10}$$

in which,

$$x\_coef = \frac{2880\lambda^4(A\alpha_{xa}^2 + B\alpha_{xb}^2 + 2C\alpha_{xa}\alpha_{xb})\rho_a{}^{1.75}}{\pi^{5.75}|K_w|^2 N_{0x}{}^{0.75}\rho_x{}^{1.75}} \,.$$

A.4 Calculating for Final Analysis of Mixing Ratios

According to Jung et al. (2008a), the total reflectivity Z is contributed by every single precipitating species as

$$Z = Z_r + Z_s + Z_{rs} + Z_g + Z_{rg} + Z_h + Z_{rh} \,. \tag{11}$$

Noting that all Z above are in linear unit (i.e., mm^6 m^{-3}), a unit conversion is needed as most reflectivity data provided are logarithmic (i.e., in dBZ).

Again, we took a grid point with rain and snow coexisting on it as an example to demonstrate our analyzing procedure. As we know the ratios among q_r, q_s, and q_{rs} at first, say $q_r : q_s : q_{rs} = a : b : c$, the unknown q_s and q_{rs} then can be represented by unknown q_r as

$$q_s = \frac{b}{a} q_r \text{ and } q_{rs} = \frac{c}{a} q_r.$$

(12)

As there are only rain and snow present on this grid we are analyzing, equation (11) can be simplified as

$$Z_{obs} = Z_r + Z_s + Z_{rs} ,$$

(13)

where the original Z on the left hand side has been replaced by Z_{obs} to denote it is a known variable. At the right hand side of equation (13), by inserting equation (7) for the first term and equation (10) for the last two terms, it can be rewritten as

$$Z_{obs} = r\_coef \times {q_r}^{1.77} + s\_coef \times {q_s}^{1.75} + rs\_coef \times {q_{rs}}^{1.75} ,$$

which can be further rewritten by applying relations from equation (12) as

$$Z_{obs} = r\_coef \times {q_r}^{1.77} + s\_coef \times \left(\frac{b}{a} q_r\right)^{1.75} + rs\_coef \times \left(\frac{c}{a} q_r\right)^{1.75}$$

$$= r\_coef \times {q_r}^{1.77} + s\_coef \times \left(\frac{b}{a}\right)^{1.75} \times {q_r}^{1.75} + rs\_coef \times \left(\frac{c}{a}\right)^{1.75} \times {q_r}^{1.75}$$

(14)

Although all terms are represented by one unknown q_r now, it is noticeable terms of rain species and non-rain species hold different power on q_r. A unified substitute is therefore applied to make the terms combinable. This unified power p is determined by weighting portions of all present species such as

$$p = (1.77a + 1.75b + 1.75c)/(a + b + c)$$

in this case. With the unified power, equation (14) can be simplified as

$$Z_{obs} = \left[r\_coef + s\_coef \times \left(\frac{b}{a}\right)^{1.75} + rs\_coef \times \left(\frac{c}{a}\right)^{1.75}\right] {q_r}^{p} .$$

(15)

Finally, the analysis result of q_r is obtained by

$$q_r = \left(\frac{Z_{obs}}{r\_coef + s\_coef \times \left(\frac{b}{a}\right)^{1.75} + rs\_coef \times \left(\frac{c}{a}\right)^{1.75}} \right)^{1/p} .$$

Mixing ratios of all other species can be further calculated by applying the ratio relations [i.e., equation (12)].

Here we have to note that some analysis errors could be included by applying the unified power *p* in the last step of the procedure: the analysis results of mixing ratio would not necessarily compose an exactly same *Z* as the observed one; in other words, the radar operator and the mixing ratio analysis process are not one hundred percent mutual- revertible. Nevertheless, according to the analysis results we have obtained throughout our study, it is believed the errors are insignificant and would not harm on providing reasonable analysis results.

Appendix B: Verification Indices

B.1 Scaled Root Mean Square Errors

Scaled root mean square (RMS) error of an arbitrary variable X between the truth simulation (denoted by subscript t) and the experiment to be verified (denoted by subscript e) is computed by

$$\text{SRMS\_X} = \sqrt{\frac{1}{N\sigma_{\Delta X}^2}\sum\nolimits_D (X_e - X_t)^2}\,,$$

where N is the total grid number in the verification domain D, and the scaling factor $\sigma_{\Delta X}^2$ is the variance of the error between the truth simulation and control experiment at initial (i.e., forecast time = 0), which can be obtained by

$$\sigma_{\Delta X}^2 = \frac{1}{N}\sum_{i=1}^{N}(\Delta X_i - \overline{\Delta X})^2\,,$$

where $\Delta X_i = (X_c - X_t)_i$ is the variable difference between the truth run and the control experiment at a specified grid point i while $\overline{\Delta X}$ is the mean value of the differences over entire verification domain.

The averaged SRMS error is computed by

$$\text{ASRMS} = \frac{1}{6}\sqrt{\frac{1}{N\sigma_{\Delta u}^2}\sum\nolimits_D \Delta u^2 + \frac{1}{N\sigma_{\Delta v}^2}\sum\nolimits_D \Delta v^2 + \frac{1}{N\sigma_{\Delta w}^2}\sum\nolimits_D \Delta w^2 \ldots .}$$

$$\overline{\ldots + \frac{1}{N\sigma_{\Delta T}^2}\sum\nolimits_D \Delta T^2 + \frac{1}{N\sigma_{\Delta q_v}^2}\sum\nolimits_D \Delta {q_v}^2 + \frac{1}{N\sigma_{\Delta q_w}^2}\sum\nolimits_D \Delta {q_w}^2}\,,$$

where u, v, and w are in [m s^{-1}], T is in [K], q_v and q_w are in [kg kg^{-1}].

Similarly, the averaging calculation above is used for SRMS of horizontal winds (V_h) presented in the context as

$$\mathrm{SRMS}_{V_h} = \frac{1}{2}\sqrt{\frac{1}{N\sigma_{\Delta u}^2}\sum_D \Delta u^2 + \frac{1}{N\sigma_{\Delta v}^2}\sum_D \Delta v^2}\,.$$

B.2 Scaled Energy Differences

Following Ge et al. (2013), three energy differences are computed as follows.

Kinetic energy difference:

$$\mathrm{KED} = \frac{1}{2}\sum_D (\Delta u^2 + \Delta v^2 + \Delta w^2)\ .$$

Thermal energy difference:

$$\mathrm{TED} = \frac{c_p}{2T_r}\sum_D \Delta T^2\ ,$$

where c_p is the specific heat equal to 1004 J K^{-1} kg^{-1} and T_r is a reference temperature of 270 K.

Latent energy difference:

$$\mathrm{LED} = \frac{{L_p}^2}{2c_pT_r}\sum_D {\Delta q_v}^2\ ,$$

where L_p is the latent heat of vaporization of 2.5×10^6 J kg^{-1}.

The EDs at any arbitrary forecast time *n* then can be scaled by their respective values at initial as

$$\mathrm{SKED}_{t=n} = \frac{\mathrm{KED}_{t=n}}{\mathrm{KED}_{t=0}}\ ,\mathrm{STED}_{t=n} = \frac{\mathrm{TED}_{t=n}}{\mathrm{TED}_{t=0}}\ ,\text{and } \mathrm{SLED}_{t=n} = \frac{\mathrm{LED}_{t=n}}{\mathrm{LED}_{t=0}}\,.$$

The averaged scaled ED at forecast time *n* is computed by

$$\mathrm{ASED}_{t=n} = \frac{1}{3}(\mathrm{SKED}_{t=n} + \mathrm{STED}_{t=n} + \mathrm{SLED}_{t=n})\,.$$